Magnetic Stabilisation of Strained Hydrogen Flames

Exploring active control strategies via magnetic fields to stabilise thermodiffusive instabilities in lean-premixed hydrogen flames

AE5122: Thesis Aerodynamics and Wind Energy

F. Aziz

Delft University of Technology

TU Delft

Cover Image is AI Generated

Magnetic Stabilisation of Strained Hydrogen Flames

Exploring active control strategies via magnetic fields to stabilise thermodiffusive instabilities in lean-premixed hydrogen flames

by

F. Aziz

to obtain the degree of Master of Science
at the Delft University of Technology,
to be defended publicly on Friday August 29, 2025 at 1:30 PM.

Student number:	5976952	
Project duration:	December 15, 2024 – August 29, 2025	
Thesis committee:	Dr. I. Langella,	TU Delft, Responsible Supervisor
	Dr. N.A.K. Doan,	TU Delft, Chairperson
	Dr. C.M. De Servi,	TU Delft, Examiner

An electronic version of this thesis is available at `http://repository.tudelft.nl/`.

TU Delft

Preface

Since the early days of my studies, I have been fascinated by how magnetic fields can shape the behaviour of gases and plasmas. I would often imagine their use in propulsion systems and wondered whether such forces could also play a role in reducing the persistent problems of pollution from combustion. At the same time, I was struck by the frustrating trade-off between CO_2 and NOx emissions; it seemed that whenever we solved one problem, another emerged. These ideas gradually built up in my mind, and when the time came to choose a thesis project, I initially proposed working on separating oxygen and nitrogen using magnetic fields. My professor, Dr. Ivan Langella, patiently listened and then gently redirected me towards something more realistic yet equally exciting: studying magnetic control of hydrogen flames.

At first, I was not convinced. Combustion, with all its turbulence and instabilities, did not appeal to me, and OpenFOAM was certainly not my favourite companion. But I also knew this challenge would push me to grow. Accepting it meant stepping outside my comfort zone, learning about hydrogen flames and their instabilities from the ground up, and developing the patience to work with complex solvers and large simulations. I soon realised that, if I embraced it fully, this one project could teach me as much as the rest of my Master's combined — and so I took the leap.

The journey that followed was demanding, but it changed me for the better. I had to find my place in a wider research effort, learn how to connect small pieces of evidence into a coherent picture, and discover the discipline of approaching research systematically. My contributions may not have been in writing solvers from scratch, but in building a framework to interpret results and explain mechanisms that were not immediately obvious. Through this process, I came to understand that research is not only about creating something entirely new, but also about clarifying, questioning, and sometimes showing why things do not work the way we expect. That realisation has been one of the most valuable lessons of this thesis.

I am deeply grateful to those who guided and supported me along the way. Dr. Ivan Langella not only set me on this path but also helped me navigate throughout this project. His guidance gave me directions where I could look to find my answers. I am also grateful for his support in the last-minute administrative hurdles with my thesis committee. My PhD supervisor, Vaibhav Mysore Natesh, was a constant source of direction and encouragement, and other colleagues in the group helped me with practical matters and kept me moving forward. Beyond the academic sphere, my friends reminded me of deadlines and provided balance, while my family offered unwavering support, both moral and practical, so that I could focus on this work without distraction. I also acknowledge the faculty for granting me access to the HPC12 cluster, without which the simulations would not have been possible.

Looking back, I see this thesis not only as a study of flames and magnetic fields but also as a journey of becoming a researcher. It has taught me resilience, patience, and the importance of small but meaningful contributions. For all the challenges and all the support I have received, I remain truly grateful. I hope that, in its own modest way, this work can serve as a step towards further exploration of how new ideas might one day help us solve the pressing problems of combustion and energy.

F. Aziz
Delft, August 2025

Abstract

This thesis explores the magnetic stabilisation of strained hydrogen flames, focusing on mitigating thermodiffusive instabilities in lean premixed laminar hydrogen flames while preserving their inherent NOx reduction benefits. Utilising comprehensive numerical simulations of counterflow flame configurations, the study reveals that radially decreasing magnetic field gradients modify flame structure, predominantly through indirect mechanisms. These mechanisms involve magnetically induced alterations to the bulk flow field, which subsequently couple with differential diffusion effects to influence the distribution of reactants, affecting mixture fraction and the temperature field. Key findings demonstrate that the representative thermal thickness of the flame remains effectively unchanged, with a kernel-density (KDE) mode shift of 0.16 %. Crucially, total kinematic stretch is reduced by approximately 5-13 % near the axis, driven primarily by the curvature-induced contribution. Tangential strain exhibits a distinct two-regime response, decreasing by about 5-8 % in the preheat zone but increasing by 6-8 % in the reaction zone. Furthermore, a two-regime velocity-field redistribution is observed, where the axial component broadly weakens, while the radial velocity decreases for low progress variable (C) near the axis and strengthens for $C \gtrsim 0.5$. This research clarifies that direct magnetic effects are intrinsically weak and negligible for practical control, with effective manipulation relying on these indirect pathways. The study also highlights that the efficacy of magnetic control diminishes with increasing strain rates and richer equivalence ratios. This work provides novel insights into the fundamental mechanisms governing magnetic control in premixed hydrogen flames, offering a framework for advancing sustainable combustion technologies.

Contents

List of Figures

List of Tables

Nomenclature

Abbreviations

Abbreviation	Definition
AI	Artificial Intelligence
CFD	Computational Fluid Dynamics
EV	Electric Vehicle
GAMG	Generalized Geometric-Algebraic Multi-Grid
HRR	Heat Release Rate
ISC	Intersystem Crossing
JANAF	Joint Army Navy Air Force
KDE	Kernel Density Estimation
LPG	Liquefied Petroleum Gas
MHD	Magnetohydrodynamics
ODE	Ordinary Differential Equation
PCG	Preconditioned Conjugate Gradient
PIMPLE	Pressure Implicit with Splitting of Operator for Pressure-Linked Equations
PISO	Pressure Implicit with Splitting of Operators
SIMPLE	Semi-Implicit Method for Pressure-Linked Equations

Symbols

Symbol	Definition	Unit
A	Pre-exponential Arrhenius factor	[varies]
a	Applied strain rate	[s^{-1}]
a_t	Tangential strain rate	[s^{-1}]
B	Magnetic field strength	[T]
B_0	Initial magnetic field strength	[T]
C	Progress variable	[-]
C_p	Specific heat at constant pressure	[J kg^{-1} K^{-1}]
D	Characteristic length	[m]
D_k^M	Species diffusivity	[m^2 s^{-1}]
D_{kl}	Binary diffusion coefficient between species k and l	[m^2 s^{-1}]
Da	Damköhler number	[-]
E_a	Activation energy	[J mol^{-1}]
$\vec{f}_i$	Magnetic body force (acceleration) on species i	[m s^{-2}]
$\vec{g}$	Gravitational acceleration	[m s^{-2}]

Symbol	Definition	Unit
g_L	Landé g-factor	[-]
h	Sensible enthalpy of the mixture	[J]
h_k	Sensible enthalpy of species k	[J]
$\vec{J}_k$	Diffusion flux of species k	[kg m^{-2} s^{-1}]
$\vec{J}_{M,i}$	Magnetic diffusion flux of species i	[kg m^{-2} s^{-1}]
$\vec{J}_{Y,i}$	Fickian diffusion flux of species i	[kg m^{-2} s^{-1}]
Ka	Karlovitz number	[-]
K_c	Equilibrium constant	[-]
k	Boltzmann constant	[J K^{-1}]
k_0	Low-pressure limit rate constant	[varies]
k_∞	High-pressure limit rate constant	[varies]
k_f	Forward reaction rate constant	[varies]
k_r	Reverse reaction rate constant	[varies]
L_b	Markstein length	[m]
Le	Lewis number	[-]
Ma	Markstein number	[-]
m_i	Molar mass of species i	[kg mol^{-1}]
$\vec{M}_i$	Magnetophoretic gradient factor	[m^{-1}]
N_A	Avogadro's number	[mol^{-1}]
p	Pressure	[Pa]
p_{ref}	Reference pressure	[Pa]
$\dot{Q}$	Volumetric Heat release rate	[W m^{-3}]
$\vec{q}$	Heat flux	[W m^{-2}]
Pr	Prandtl number	[-]
R	Gas constant of the mixture	[J kg^{-1} K^{-1}]
Re	Reynolds number	[-]
R_u	Universal gas constant	[J mol^{-1} K^{-1}]
Sc	Schmidt number	[-]
S_c	Consumptions Speed	[m s^{-1}]
S_D	Flame displacement speed	[m s^{-1}]
S_D^k	Kinetic component of flame displacement speed	[m s^{-1}]
S_D^{diff}	Diffusion component of flame displacement speed	[m s^{-1}]
S_L	Laminar flame speed	[m s^{-1}]
S_i	Spin quantum number of species i	[-]
T	Temperature	[K]
T_a	Adiabatic flame temperature	[K]
T_b	Burnt gas temperature	[K]
T_u	Unburnt gas temperature	[K]
U	Characteristic velocity	[m s^{-1}]
$\vec{v}$	Flow velocity	[m s^{-1}]
$\vec{V}_k$	Diffusion velocity of species k	[m s^{-1}]
X_k	Mole fraction of species k	[-]

Symbol	Definition	Unit
Y_k	Mass fraction of species k	[-]
Z	Bilger mixture fraction	[-]
α	Thermal diffusivity of the gas mixture	[m^2 s^{-1}]
α_k	Thermal diffusivity of species k	[m^2 s^{-1}]
β	Temperature exponent in the Arrhenius equation	[-]
γ	Ratio of specific heats	[-]
δ	Flame thickness	[m]
κ	Total stretch rate	[s^{-1}]
λ	Thermal conductivity	[W m^{-1} K^{-1}]
μ	Dynamic viscosity	[N s m^{-2}]
μ_0	Permeability of free space	[H m^{-1}]
ν	Kinematic viscosity	[m^2 s^{-1}]
ρ	Density	[kg m^{-3}]
σ	Thermal expansion ratio	[-]
τ	Stress tensor	[N m^{-2}]
τ_c	Chemical timescale	[s]
τ_η	Kolmogorov timescale	[s]
τ_{flow}	Flow timescale	[s]
ϕ	Equivalence ratio	[-]
$\vec{\phi}$	Mass flux	[kg m^{-2} s^{-1}]
Φ	Viscous dissipation	[J s^{-1}]
χ_i	Magnetic susceptibility of species i	[-]
$\dot{\omega}_k$	Production rate of species k	[kg m^{-3} s^{-1}]

1

Introduction

Combustion technology has played an essential role in shaping human civilisation, significantly impacting societal and technological advancements from prehistoric times through to the modern industrial era. Initially harnessed by early humans for basic survival needs such as cooking, heating, and protection, combustion technology evolved substantially over time, facilitating major material and industrial breakthroughs. For instance, ancient civilisations, including the Egyptians, utilised combustion for metal smelting and pottery kilns, laying foundations for future technological innovations [1]. Major milestones such as James Watt's steam engine during the Industrial Revolution and the internal combustion engines developed by Nikolaus Otto and Rudolph Diesel greatly accelerated transportation, globalisation, and economic growth [1]. The subsequent advent of jet engines, pioneered by Frank Whittle and Hans van Ohain, underscored the versatility and significance of combustion technologies in modern aviation and power generation [1]. Today, amidst growing environmental concerns and sustainability challenges, combustion technology is once again at a critical juncture. The urgent need for cleaner, efficient energy systems has driven research towards advanced combustion solutions, particularly focusing on hydrogen as a promising clean fuel. However, significant technical challenges remain, including stabilising strained hydrogen flames and controlling associated thermo-diffusive instabilities. This thesis directly addresses these challenges by investigating magnetic control strategies to enhance hydrogen flame stability, contributing to the ongoing evolution of sustainable combustion technologies.

1.1. Background and Motivation

Combustion technologies have long been the cornerstone of human development, shaping societies by enabling technological progress and economic growth. To understand the modern-day challenges and innovations in combustion, particularly concerning hydrogen as a cleaner fuel, it's important to first consider the historical role and transformative impact combustion has had on civilisation.

1.1.1. Historical Role of Combustion Technologies

Combustion has significantly influenced human progress across multiple eras, from early human survival to contemporary global industries. Historically, each advancement in combustion technology has catalysed major economic, societal, and technological shifts, setting the stage for modern research and innovation in sustainable energy solutions.

Prehistoric and Ancient Combustion Applications

Early civilisations harnessed combustion primarily for survival and basic development [1]:

- Fire for cooking, heating, and protection by early humans.
- Metal smelting and pottery kilns by ancient Egyptians and other early cultures enabled early industrial capabilities [1], [2].

Industrial Revolution: Steam Power and Mechanisation

The Industrial Revolution (18th Century) marked a pivotal transformation:

- James Watt significantly improved the steam engine, revolutionising transportation, manufacturing, and urbanisation [3].

Advances in Internal Combustion (19th-20th Centuries)
Major innovations included the development of internal combustion engines, which profoundly affected transportation and industrial sectors:

- Nikolaus Otto and Rudolf Diesel introduced efficient internal combustion engines [4].
- These engines facilitated the rapid expansion of the automotive industry, globalisation, and widespread economic growth.

20th-Century Aviation and Power Generation
Combustion technology reached new heights in aviation and electricity generation during the 20th century:

- Jet engines, pioneered by Frank Whittle and Hans van Ohain, enabled unprecedented aviation advancements [5].
- Combustion-based power plants became central to global electricity production, underpinning industrial and technological expansion [1].

The transformative impact of historical combustion technologies has directly shaped the modern economic and industrial landscape. Today, facing mounting environmental concerns, combustion research is increasingly directed towards sustainability and efficiency. The lessons from historical technological shifts are instrumental in guiding current efforts to transition towards cleaner combustion practices, notably in hydrogen technologies, as addressed in this research.

1.1.2. Global Energy Landscape and Sustainability Challenges

The modern global economy is deeply dependent on combustion-based energy, predominantly fossil fuels such as coal, oil, and natural gas, which accounted for approximately 81.5% of global primary energy consumption as of 2023 [6]. This persistent reliance spans key sectors including electricity generation, transportation, and industrial processes, with coal and natural gas notably dominant in power production and petroleum fuels widely used in transport sectors. To illustrate the global distribution of energy consumption clearly, Figure 1.1 highlights the significant dominance of fossil fuels compared to renewable sources, underlining the magnitude of the sustainability challenge facing current and future generations.

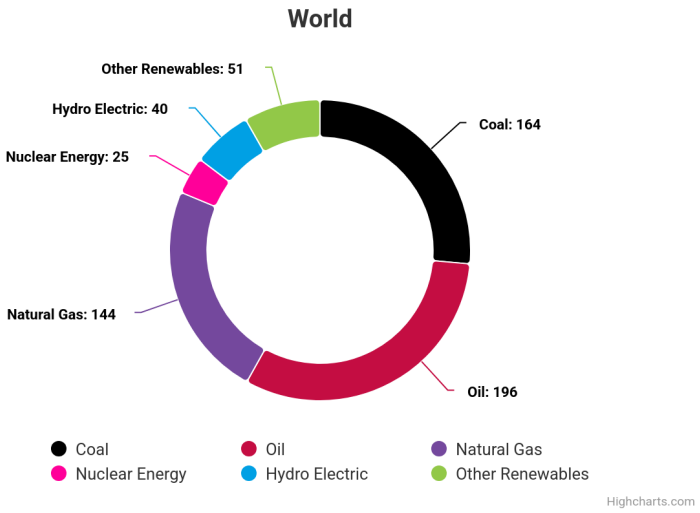

Figure 1.1: Global energy consumption [6]

However, this heavy reliance on fossil fuels has led to critical environmental and sustainability challenges, primarily due to substantial greenhouse gas emissions and air pollutants such as nitrogen oxides (NOx) and sulfur dioxide (SO_2). High-temperature combustion processes, essential in industries such as steel and cement manufacturing, significantly contribute to global greenhouse gas emissions, with the steel and cement sectors alone accounting for approximately 7% and 8% of global CO_2 emissions, respectively [7]. Aviation further exacerbates this issue, contributing notably to global emissions through both CO_2 and non-CO_2 factors, despite advancements in engine efficiencies and fuel technologies. The persistent environmental impacts, such as air pollution-linked health issues, ecosystem degradation, and resource depletion, underscore the urgent need for transitioning toward

sustainable and cleaner combustion technologies, including the adoption of hydrogen as a viable, lower-emission energy carrier.

1.1.3. Hydrogen as a Clean and Sustainable Fuel

In the quest for sustainable energy alternatives, hydrogen has emerged as a leading candidate due to its high energy density and clean combustion characteristics. Hydrogen boasts a specific energy density of 120 MJ/kg, which is significantly higher than that of conventional fossil fuels like gasoline (44-46 MJ/kg) [8]. Unlike conventional fossil fuels, hydrogen combustion primarily produces water vapor, substantially reducing carbon emissions when combusted with pure oxygen [9]. Even when air is used as an oxidizer, hydrogen combustion generates significantly lower greenhouse gas and particulate emissions compared to traditional hydrocarbons [9]. As a result, hydrogen is actively being integrated across various sectors, including:

- **Power Generation:** Hydrogen fuel cells and hydrogen-blended turbines provide electricity with reduced or zero emissions, playing a vital role in decarbonising electricity grids.
- **Transportation:** Hydrogen fuel cells in electric vehicles (EVs) offer a zero-emission alternative to fuels based on petroleum [10]. Additionally, hydrogen combustion engines are being explored as transitional technologies due to their lower emissions compared to conventional internal combustion engines[11].
- **Aerospace:** Liquid hydrogen has long been utilised as rocket fuel due to its superior energy-to-weight ratio, and its application is expanding within aviation to reduce emissions.

1.2. Research Context

Hydrogen's potential as a clean energy carrier is accompanied by complex combustion behaviours that differ significantly from those of conventional hydrocarbon fuels. These differences arise primarily due to hydrogen's distinct physical and chemical properties, such as high diffusivity, low molecular weight, and fast flame speeds [12]. As hydrogen-based energy systems move from experimental stages toward practical deployment, it is critical to understand the combustion-specific challenges that hinder stability, efficiency, and emissions control.

1.2.1. Combustion Challenges in Hydrogen Applications

Hydrogen combustion presents several fundamental challenges that stem from its unique thermophysical properties. Hydrogen flames exhibit heightened sensitivity to hydrodynamic instabilities, such as the Darrieus–Landau instability, where density differences between unburned and burned gases cause perturbations along the flame front [12]. Furthermore, buoyancy-driven instabilities, resulting from large density gradients in gravitational fields, can distort flame geometry, especially in terrestrial and low-gravity environments [12]. Thermoacoustic instabilities, oscillations driven by interactions between heat release and acoustic waves, are especially concerning in confined combustion systems such as turbines and propulsion chambers [13].

One of the most prominent is its strong susceptibility to thermo-diffusive instabilities in lean conditions due to a Lewis number less than one ($Le < 1$) [12]. This condition causes hydrogen to diffuse much faster than heat, disrupting local flame front uniformity and leading to wrinkled or cellular flame structures that can degrade combustion efficiency and control.

1.2.2. Thermo-Diffusive Instabilities in Hydrogen Flames

Thermo-diffusive instability is a dominant flame instability mechanism in hydrogen-air mixtures due to hydrogen's low Lewis number ($Le < 1$), which implies that hydrogen diffuses significantly faster than heat [14]. This preferential diffusion creates local imbalances in fuel concentration and temperature, giving rise to cellular flame structures and uneven flame propagation. These effects are particularly severe in lean hydrogen mixtures, which are often used to reduce flame temperature and NOx emissions in practical systems. In strained flow environments, such as in turbulent combustion regimes, thermo-diffusive instabilities become even more pronounced due to the added complexity of flame stretch and curvature distortion due to turbulent eddies [15].

In addressing these challenges, current research explores advanced strategies such as magnetic control in lean premixed combustion. Lean premixed combustion effectively reduces flame temperatures, thus curbing NOx emissions and mitigating thermoacoustic instabilities [16], yet the inherent high flame speed of hydrogen introduces risks of flashback and flame instabilities. To further stabilise hydrogen flames, magnetic fields present an innovative approach.

1.2.3. Magnetic Control Strategies: An Emerging Solution

Magnetic control of combustion has emerged as a novel, non-intrusive strategy to influence flame behaviour through the manipulation of paramagnetic species and charged radicals. In hydrogen flames, particularly those exhibiting thermo-diffusive instabilities, magnetic fields can modify the transport of key intermediates such as OH and HO_2 radicals, thereby impacting local heat release, flame position, and propagation dynamics [17], [18]. Studies have demonstrated that magnetic field gradients alter flame shape and shift reaction zones, thus offering a new layer of control in hydrogen combustion systems [19], [20]. Unlike conventional stabilisation methods that require changes to burner geometry or fuel composition, magnetic fields can be externally applied and dynamically tuned to target specific instability mechanisms.

Given hydrogen's high diffusivity and instability-prone behaviour, integrating magnetic control into combustion modelling represents a promising avenue for reducing NOx emissions and extending flame stability limits. The following chapters build on this foundation by exploring the theoretical basis, experimental evidence, and simulation-based evaluation of magnetic field effects in counterflow hydrogen flame configurations.

1.3. Problem Statement and Research Objectives

To effectively address combustion instabilities in hydrogen-based energy systems, it is essential to clearly identify and articulate the specific research gaps and challenges present in existing literature and practice. This section explicitly states the core problem that this thesis aims to tackle, laying the groundwork for the research objectives and questions that guide the investigation throughout the study.

1.3.1. Problem Statement

While combustion technology has advanced significantly, the unique combustion properties of hydrogen continue to pose critical challenges. Hydrogen flames exhibit notable thermo-diffusive instabilities due to their inherently low Lewis number in lean conditions, causing preferential diffusion effects that alter local flame dynamics. Traditional stabilisation strategies often rely on modifying burner geometry, fuel composition, or injection methods; however, these can be complex, costly, or insufficient under highly strained or lean conditions [21], [22]. Magnetic field gradients have emerged as an innovative control method, with the potential to selectively influence radical distributions and species diffusion. However, most existing studies focus on hydrocarbon flames and overlook the role of magnetically induced diffusion and radical redistribution in hydrogen flames, particularly under realistic strained flame conditions. The direct and indirect mechanisms by which magnetic fields can influence and potentially stabilise hydrogen premixed counterflow flames have not yet been systematically explored.

Therefore, this study investigates whether magnetic field gradients can effectively modify the stability characteristics of lean premixed hydrogen counterflow flames by leveraging direct diffusion-driven mechanisms and indirect convective effects, particularly examining the impact of these fields on differential species diffusion, radical redistribution, and Markstein Length.

1.3.2. Research Objectives

Building on the central problem outlined above, the primary aim of this thesis is to assess whether magnetic fields can serve as an effective control mechanism for stabilising thermo-diffusively unstable hydrogen premixed flames. The research is structured to evaluate both direct magnetic influences, such as species-specific diffusion enhancements, and indirect mechanisms arising from modified convection and strain field dynamics. The objectives are formulated to ensure a comprehensive investigation of magnetic field effects in a numerically modelled counterflow flame system under realistic, non-unity Lewis number conditions:

1. To design and execute a parametric simulation study on lean premixed hydrogen counterflow flames under varying magnetic field strengths, directions, and gradient types.
2. To analyse flame structure, radical distribution (especially OH), and global flame parameters (e.g., flame position, curvature, thickness) in response to magnetic field application.
3. To evaluate the relative contributions of direct magnetic diffusion versus indirect convective and reactive effects in modifying flame behaviour.
4. To assess whether magnetic fields can significantly alter Markstein Length and extend flame stability limits under high-strain conditions.

1.3.3. Research Questions

The following research questions were formulated to guide the investigation and provide clarity on the key aspects of magnetic field influence on hydrogen flame stability. These questions are aligned with the stated objectives and seek to uncover both a mechanistic understanding and practical implications of magnetic control in strained hydrogen flames.

1. Can magnetic field gradients significantly modify the structure and stability of lean hydrogen premixed counterflow flames through either direct or indirect mechanisms?
2. How do magnetic field strength, gradient type, and orientation affect the transport and spatial distribution of key radicals, particularly OH, in non-unity Lewis number conditions?
3. What roles do direct magnetic effects, such as species-specific diffusion and heat transport, play in modifying flame dynamics, and how do these compare in magnitude and influence to indirect effects like convection and reaction rate alterations?
4. In what ways does magnetic field application influence fundamental flame parameters such as Markstein Length, flame speed, and curvature under strained conditions, and how are these effects mediated by flame structure and transport phenomena?

1.4. Research Methodology Overview

To address the research objectives and questions outlined in the previous section, this study employs a computational approach using high-fidelity numerical simulations. Given the complexity of hydrogen combustion and its sensitivity to strain and differential diffusion, CFD simulations were used to evaluate the role of magnetic fields in controlling flame behaviour. This section provides a brief overview of the modelling and simulation strategy adopted in this thesis, while comprehensive details are provided in subsequent chapters.

1.4.1. Numerical Modelling and Simulation Approach

The numerical investigations in this study were conducted using a customised CFD solver built upon a laminar premixed counterflow flame configuration. The modified solver incorporated magnetic field effects, including gradient-based magnetic diffusion, and to support both unity and non-unity Lewis number conditions. The primary flame model resolves a two-dimensional, steady, axisymmetric hydrogen-air flame stabilised between opposing reactant and product inlets under varying strain rates.

Two separate stages of simulation were carried out:

- **Stage 1:** Preliminary analysis under the unity Lewis number assumption to understand the solver behaviour and assess the general trends in magnetic interaction with flame structure. This included multiple parametric studies across magnetic field strengths, directions, and gradients.
- **Stage 2:** Advanced simulations using non-unity Lewis number formulations based on the San Diego reaction mechanism. This stage included the full coupling of magnetic field terms with detailed transport property models, allowing analysis of both direct and indirect effects of magnetic control in premixed hydrogen flames.

The simulation results were post-processed to extract flame characteristics, radical species distribution, strain fields, and curvature. These outputs form the core dataset for analysing magnetic influence on flame stability, as explored in later chapters.

1.5. Scope and Thesis Structure

This thesis investigates the influence of magnetic field gradients on the stability and behaviour of lean hydrogen premixed counterflow flames. The study is limited to numerical simulations using detailed chemical kinetics, species transport, and magnetically induced diffusion under laminar, steady-state conditions. While the focus is on hydrogen combustion in a counterflow configuration, the findings aim to inform broader research on flame stabilisation strategies and emissions control in advanced energy systems. Experimental validation, turbulence modelling, and large-scale reactor effects are beyond the scope of this work but are identified as potential directions for future research.

The remainder of the thesis is organised as follows:

- **Chapter 2 & 3 - Literature Review:** Chapter 2 reviews the fundamental properties of hydrogen combustion, key instability mechanisms with emphasis on thermo-diffusive instabilities and the instability parameters to quantify them. Chapter 3 presents a detailed review of the theoretical and experimental developments

in magnetic combustion control. Emphasises knowledge gaps related to hydrogen flames, particularly in strained premixed configurations, and introduces the rationale for the current study.

- **Chapter 4 – Methodology:** Describes the numerical setup, solver modifications, chemical mechanisms, boundary conditions, and simulation parameters. Includes mesh convergence, validation steps, and computational considerations.
- **CHapter 5 - Results:** Analyse simulation results across various magnetic field configurations and flame conditions for unity Lewis number cases and differential diffusion cases. Focuses on flame stabilisation behaviour, radical redistribution, and parametric sensitivity of magnetic effects.
- **Chapter 6 – Conclusions:** Summarises key findings, evaluates the effectiveness of magnetic control strategies, and outlines limitations and future directions for both simulation and experimental work.

2

Hydrogen Combustion

Hydrogen is widely used across various sectors owing to its versatile chemical properties and high energy content per unit mass [8]. Beyond its industrial applications in petroleum refining, ammonia synthesis, and methanol production, hydrogen plays a growing role in energy, transportation, and aerospace systems, either through direct combustion or via electrochemical conversion in fuel cells [1]. In the power generation sector, hydrogen is utilised in fuel cells to produce electricity with high efficiency and zero emissions. It is also combusted in modified gas turbines, either in pure form or blended with conventional fuels, to reduce the carbon intensity of thermal power plants [23]. In the transportation industry, hydrogen fuel cells power electric vehicles as a zero-emission alternative to conventional engines, while certain applications have explored hydrogen combustion in internal combustion engines as a transitional, low-emission technology [10]. In aerospace, liquid hydrogen has long been used as a high-energy propellant in rocket engines due to its superior specific impulse and combustion efficiency.

Despite these advantages, the practical use of hydrogen in combustion systems presents several challenges. Its low molecular weight leads to high diffusivity, increasing the risk of flame instabilities, particularly under lean premixed conditions. Additionally, hydrogen has a wide flammability range and low ignition energy [24], which, while beneficial for ignition, also raises safety concerns in uncontrolled environments. These factors necessitate a deeper understanding of hydrogen flame behaviour, particularly its chemical kinetics, transport properties, and instability mechanisms, to develop safe and efficient hydrogen-based combustion systems.

This chapter provides the theoretical foundation for understanding hydrogen combustion, starting with the reaction mechanism and kinetic pathways that govern its ignition and flame propagation characteristics.

2.1. Reaction Mechanism

Hydrogen combustion, at its most fundamental level, involves the oxidation of hydrogen to form water. While the global reaction is often represented as:

$$2H_2 + O_2 \rightarrow 2H_2O$$

such a representation omits the complex radical-driven chain reactions that govern flame propagation, ignition delays, and pollutant formation. In realistic combustion environments, particularly those involving lean premixed conditions and finite residence times, the assumption of instantaneous reaction rates is no longer valid. Accurate modelling requires detailed finite-rate chemistry to resolve the dynamic interaction of multiple reactive intermediates. Furthermore, when air is used as the oxidiser, interactions between radicals and atmospheric nitrogen lead to NOx formation, requiring precise tracking of both major and minor species.

This study adopts the San Diego mechanism, which incorporates 21 elementary reactions among 9 chemically reacting species with inert nitrogen (N_2, H, O_2, OH, O, H_2, H_2O, HO_2, H_2O_2, O_3) [25]. The mechanism has been widely validated for hydrogen-air combustion and provides a balanced compromise between computational cost and chemical fidelity in simulating radical-sensitive flames.

H_2-O_2 Chain Reactions

$$\mathrm{H + OH \rightarrow O_2 + H} \tag{2.1}$$
$$\mathrm{O + H_2 \rightarrow OH + H} \tag{2.2}$$
$$\mathrm{OH + H_2 \rightarrow H_2O + H} \tag{2.3}$$
$$\mathrm{O + H_2O \rightarrow 2OH} \tag{2.4}$$

H_2-O_2 Dissociation/Recombination Reactions

$$\mathrm{2H + M \rightarrow H_2 + M} \tag{2.5}$$
$$\mathrm{H + OH + M \rightarrow H_2O + M} \tag{2.6}$$
$$\mathrm{2O + M \rightarrow O_2 + M} \tag{2.7}$$
$$\mathrm{O + H + M \rightarrow OH + M} \tag{2.8}$$
$$\mathrm{O_3 + M \rightarrow O_2 + O + M} \tag{2.9}$$

Formation and Consumption of HO_2

$$\mathrm{H + O_2 + M \rightarrow HO_2 + M} \tag{2.10}$$
$$\mathrm{H + HO_2 \rightarrow H_2 + O_2} \tag{2.11}$$
$$\mathrm{H + HO_2 \rightarrow H_2O + O} \tag{2.12}$$
$$\mathrm{H + HO_2 \rightarrow 2OH} \tag{2.13}$$
$$\mathrm{O + HO_2 \rightarrow O_2 + OH} \tag{2.14}$$
$$\mathrm{OH + HO_2 \rightarrow O_2 + H_2O} \tag{2.15}$$

Formation and Consumption of H_2O_2

$$\mathrm{2OH + M \rightarrow H_2O_2 + M} \tag{2.16}$$
$$\mathrm{2HO_2 \rightarrow H_2O_2 + O_2} \tag{2.17}$$
$$\mathrm{H + H_2O_2 \rightarrow H_2O + OH} \tag{2.18}$$
$$\mathrm{H + H_2O_2 \rightarrow HO_2 + H_2} \tag{2.19}$$
$$\mathrm{O + H_2O_2 \rightarrow HO_2 + OH} \tag{2.20}$$
$$\mathrm{OH + H_2O_2 \rightarrow HO_2 + H_2O} \tag{2.21}$$

Here, equations 2.1 - 2.4 follow the reversible Arrhenius rate equation given by $k = AT^{\beta}\exp(-E_a/RT)$, where T is temperature, A is the forward rate constant, E_a is the activation energy and R is the gas constant. Equations 2.5 - 2.9 are recombination-dissociation reactions requiring a third body M to stabilise the reaction. Each reaction species, M, has a different efficiency in stabilising the reaction. The reactions of formation of HO_2 and H_2O_2, represented by equations 2.10 and 2.16, have pressure-dependent reaction rates. These reactions follow the Troe Fall-Off mechanism, characterised by the reaction rates interpolated between a low-pressure rate k_0 and a high-pressure rate k_∞. The remaining reactions follow the reversible Arrhenius rate equation.

With the chemical kinetics now established, it becomes essential to describe how these reactions interact with fluid transport phenomena to govern flame behaviour. The following section outlines the fundamental conservation equations that form the basis of reacting flow modelling, incorporating mass, momentum, species, and energy transport. Additionally, relevant non-dimensional parameters are introduced to characterise the dominant physical processes and provide insight into the stability and structure of hydrogen flames.

2.2. Governing Equations for Reacting Flows

Modelling reacting flows in hydrogen combustion involves solving a system of tightly coupled transport equations that govern the evolution of mass, momentum, chemical species, and energy. Given the low-Mach number regime relevant to this study, compressibility effects such as acoustic wave propagation are neglected, and the flow is treated as incompressible. However, due to significant heat release and changes in species composition, the fluid density varies spatially and is treated as a dependent thermodynamic variable. In this study, density is updated from the local temperature using the ideal gas law, assuming a constant reference pressure. This approach is consistent with standard low-Mach number formulations for reacting flows, as demonstrated in the work of Lessani and Papalexandris [26], and is commonly adopted in computational combustion solvers.

The governing equations employed here are based on the framework outlined in *Principles of Combustion* by Kuo [27], and describe a variable-density, incompressible reacting system suitable for premixed combustion analysis.

2.2.1. Conservation of Mass

The conservation of mass for a variable-density flow is given by:

$$\frac{\partial \rho}{\partial t} + \nabla \cdot (\rho \vec{v}) = 0 \tag{2.22}$$

In low Mach number combustion systems, the assumption of incompressibility implies that pressure-induced density changes are negligible. However, spatial variations in density arise due to changes in temperature and species mass fractions, particularly across the flame front. In this study, density is not solved from an additional equation but is updated explicitly using the ideal gas law:

$$\rho = \frac{p_{\text{ref}}}{RT} \tag{2.23}$$

Here, p_{ref} is the reference pressure (assumed constant), and T is the local temperature. As a result, the continuity equation must retain the density term within the divergence operator. This variable-density formulation, while neglecting compressibility effects, allows for accurate representation of thermal expansion and species-driven density gradients in reacting flows [26].

2.2.2. Conservation of Momentum

The momentum conservation equation for a variable-density, low-Mach number flow without body forces is given by:

$$\frac{\partial (\rho \vec{v})}{\partial t} + \nabla \cdot (\rho \vec{v} \vec{v}) = -\nabla p + \nabla \cdot \boldsymbol{\tau} \tag{2.24}$$

Here, $\vec{v}$ is the velocity vector, p is the pressure, and $\boldsymbol{\tau}$ is the viscous stress tensor. For a Newtonian fluid, the stress tensor is defined as [27]:

$$\boldsymbol{\tau} = \mu \left(\nabla \vec{v} + (\nabla \vec{v})^T \right) - \frac{2}{3} \mu (\nabla \cdot \vec{v}) \mathbf{I} \tag{2.25}$$

where μ is the dynamic viscosity and $\mathbf{I}$ is the identity tensor. Although the flow is treated as incompressible in the low-Mach number sense, the divergence of velocity $\nabla \cdot \vec{v}$ is generally non-zero due to local variations in density arising from heat release and species transport. As such, the full form of the viscous stress tensor is retained in the momentum equation. Utilising the mass conservation equation, the conservation of momentum equation can be simplified to:

$$\rho \frac{\partial \vec{v}}{\partial t} + (\vec{\phi} \cdot \nabla) \vec{v} = -\nabla p + \nabla \cdot \boldsymbol{\tau} \tag{2.26}$$

where $\vec{\phi} = \rho \vec{v}$ is the mass flux.

2.2.3. Conservation of Reacting Species

The transport equation for each chemical species k in a reacting flow is given by:

$$\frac{\partial (\rho Y_k)}{\partial t} + \nabla \cdot (\rho Y_k \vec{v}) = -\nabla \cdot (J_k) + \dot{\omega}_k \tag{2.27}$$

Here, Y_k is the mass fraction of species k, $\vec{v}$ is the bulk velocity, $\vec{J_k} = \rho \vec{V_k} Y_k$ is the diffusion flux of the species k, $\vec{V_k} = \vec{v_k} - \vec{v}$ is the diffusion velocity of the species k relative to the bulk flow, and $\dot{\omega}_k$ denotes the net production rate of the species due to chemical reactions.

In this study, species diffusion is modelled using Fick's Law, where the diffusion flux is assumed to be proportional to the gradient of species concentration:

$$J_k = \rho Y_k \vec{V_k} = -\rho D_k^M \nabla Y_k \tag{2.28}$$

In the present study, only Fickian diffusion is considered in the transport model. The Soret effect, although known to influence the reaction rates in lean hydrogen flames significantly [28], has been omitted. This simplification was adopted to reduce the number of coupled transport phenomena, allowing a focused one-on-one comparison of the effects of magnetically induced diffusion fluxes. While the omission of the Soret effect may affect quantitative flame structure, it does not preclude the qualitative assessment of magnetic field effects. Including both Soret and magnetically induced fluxes simultaneously would have convoluted the analysis and obscured the one-on-one relationship between applied magnetic fields and species transport.

Assuming a low-Mach number flow, with variable density and negligible barodiffusion, the species transport equation simplifies to the following convective-diffusive form:

$$\rho\frac{\partial Y_k}{\partial t} + \vec{\phi}\cdot\nabla Y_k = \nabla\cdot(\rho D_k^M \nabla Y_k) + \dot{\omega}_k \tag{2.29}$$

where D_k^M is the effective mixture-averaged diffusion coefficient for species k. The right-hand side includes the combined effects of molecular diffusion and chemical reaction.

2.2.4. Conservation of Energy

The conservation of energy in reacting flows accounts for the transport of sensible enthalpy due to convection, heat conduction, species diffusion, chemical heat release, and mechanical work. In the present study, the energy equation is expressed in terms of the sensible enthalpy, $h = C_pT$, where C_p is the specific heat at constant pressure and T is the local temperature. The general form of the energy equation is given by:

$$\frac{\partial(\rho h)}{\partial t} + \nabla\cdot(\rho h\vec{v}) - \frac{Dp}{Dt} = -\nabla\cdot\vec{q} + \dot{Q} + \Phi \tag{2.30}$$

Here:

- $\vec{q}$ is the total heat flux vector,
- $\dot{Q}$ represents the chemical heat release rate,
- Φ is the viscous dissipation term.

The chemical heat release is computed using the species production terms and their sensible enthalpies:

$$\dot{Q} = -\sum_{k=1}^{N} h_k\dot{\omega}_k$$

where h_k is the specific sensible enthalpy of species k, and $\dot{\omega}_k$ is the net production rate of that species due to chemical reactions. The total heat flux $\vec{q}$ includes three main components [27]:

$$\begin{aligned}\vec{q} &= \vec{q}_{\text{conduction}} + \vec{q}_{\text{interdiffusion}} + \vec{q}_{\text{Dufour}} \\ &= -\lambda\nabla T + \rho\sum_{k=1}^{N} h_k Y_k \vec{V}_k + R_u T\sum_{k=1}^{N}\sum_{l=1}^{N}\left(\frac{X_l\alpha_k}{m_k D_{kl}}\right)(\vec{V}_k - \vec{V}_l)\end{aligned}$$

where λ is the thermal conductivity, h_k is the sensible enthalpy of species k, α_k is the thermal diffusivity of species k and D_{kl} is the binary diffusion constant between species k and l. The first term represents Fourier heat conduction, the second accounts for species interdiffusion, and the third is the Dufour effect. The Dufour effect arises from cross-coupling between mass and heat fluxes, where mass diffusion of species leads to additional thermal energy transport. However, in typical combustion scenarios, especially for hydrogen-air mixtures at atmospheric pressures, the Dufour effect is generally negligible compared to conduction and species enthalpy transport. Therefore, it is omitted in this work to reduce model complexity. Likewise, the viscous dissipation term Φ is negligible for low-speed, laminar flames and is excluded from the final equation.

Although the general formulation includes the pressure work term Dp/Dt, this term is omitted in the present study. Under the low-Mach number approximation, pressure remains nearly spatially uniform and serves primarily as a mechanical constraint rather than a thermodynamic variable. As such, the pressure work contribution is minimal. This simplification is widely supported in the literature. Majda and Sethian (1985) [29] analytically derive the low-Mach formulation, showing that Dp/Dt vanishes in the asymptotic limit. Almgren et al. (2006) [30] similarly neglect this term in their numerical models for low-Mach reacting flows. In addition to theoretical justification, removing this term improves solver stability in practice. The simplified equation for the conservation of energy then becomes:

$$\rho\frac{\partial h}{\partial t} + \vec{\phi}\cdot\nabla h = \nabla\cdot(\lambda\nabla T) - \nabla\cdot\left(\sum_{k=1}^{N} h_k\vec{J}_k\right) + \dot{Q} \tag{2.31}$$

2.2.5. Equation of State

In this study, the ideal gas law is used to relate the thermodynamic pressure, density, and temperature of the gas mixture. The equation of state is given by:

$$p = \rho R T \tag{2.32}$$

where R is the specific gas constant of the mixture, computed from:

$$R = R_u \sum_{k=1}^{N} \frac{Y_k}{m_k} \tag{2.33}$$

Here, $R_u$is the universal gas constant, and $m_k$is the molecular weight of the species k. The specific gas constant R thus varies spatially depending on the local species composition.

2.2.6. Summary of Governing Equations

The governing equations for reacting flows for an incompressible flow regime are as follows [27].

$$\frac{\partial u_i}{\partial x_i} = 0 \tag{2.34}$$

$$\frac{\partial u_j}{\partial t} + u_i \frac{\partial u_j}{\partial x_i} = -\frac{1}{\rho}\frac{\partial p}{\partial x_j} + \nu \frac{\partial^2 u_j}{\partial x_i \partial x_i} + Y_k f_{k,j} \tag{2.35}$$

$$\frac{\partial Y_k}{\partial t} + u_i \frac{\partial Y_k}{\partial x_i} = \frac{\partial}{\partial x_i}\left(D_k^M \frac{\partial Y_k}{\partial x_i}\right) + \frac{\dot{\omega}_k}{\rho} \tag{2.36}$$

$$\begin{aligned} \frac{\partial T}{\partial t} + u_i \frac{\partial T}{\partial x_i} - \frac{1}{\rho C_p}\frac{Dp}{Dt} = \frac{\partial}{\partial x_i}\left(\alpha \frac{\partial T}{\partial x_i}\right) - \sum_{k=1}^{N}\left(\frac{C_{p,k} D_k^M}{C_p}\right)\left[\frac{\partial Y_k}{\partial x_i}\frac{\partial T}{\partial x_i} + T\frac{\partial^2 Y_k}{\partial x_i \partial x_i}\right] \\ - \frac{\Delta h_{f,k}^{\circ}\dot{\omega}_k}{\rho C_p} + \sum_{k=1}^{N}\frac{D_k^M}{C_p}\left(f_{k,i}\frac{\partial Y_k}{\partial x_i}\right) \end{aligned} \tag{2.37}$$

$$p = \rho R T \tag{2.38}$$

2.2.7. Dimensionless Parameters

To better understand the interplay between transport processes and chemical reactions in hydrogen flames, it is useful to introduce key non-dimensional parameters. These provide insight into flow behaviour, diffusion dominance, and flame stability characteristics. The dimensionless numbers considered in this study are the Reynolds Number (Re), Prandtl Number (Pr), Schmidt Number (Sc), Lewis Number (Le), and Karlovitz Number (Ka). Each plays a unique role in characterising the flame structure, transport, and susceptibility to instabilities.

Reynolds Number (Re)

The Reynolds Number is defined as the ratio of inertial forces to viscous forces and is expressed as

$$Re = \frac{UD}{\nu} \tag{2.39}$$

where U is the characteristic flow velocity, D is the characteristic length, and ν is the kinematic viscosity. In this study, the low Reynolds Number regime ensures laminar flow, which is a typical assumption in counterflow flame modelling.

Prandtl Number (Pr)

The Prandtl Number represents the ratio of momentum diffusivity to thermal diffusivity and is given by

$$Pr = \frac{\nu}{\alpha} \tag{2.40}$$

where α is the thermal diffusivity. For most air-like gas mixtures, Pr is typically around 0.7. In this work, Pr is fixed at 0.7, consistent with common assumptions for hydrogen-air mixtures.

Schmidt Number (Sc)
The Schmidt Number relates momentum diffusivity to mass diffusivity and is expressed as:

$$Sc_k = \frac{\nu}{D_k^M} \tag{2.41}$$

where D_k^M is the species-specific mixture-averaged mass diffusivity of species k, and ν is the kinematic viscosity. Typically, Sc is assumed to be 0.7 for air-like mixtures, including hydrogen, unless otherwise stated. This simplification is common in combustion modelling, where multi-component diffusion is not explicitly solved.

In this study, however, we employ species-specific diffusion coefficients calculated using the binary diffusion coefficients for each species in the mixture. As such, the Schmidt number is implicitly accounted for in the species-specific diffusion terms, and the need for an averaged Schmidt number is removed. Therefore, while Sc remains conceptually relevant for understanding species diffusion, it is not explicitly used in this study due to the direct calculation of D_k^M for each species.

Lewis Number (Le)
The Lewis Number is the most important non-dimensional parameter in this study, particularly for hydrogen combustion. It is defined as

$$Le_k = \frac{\alpha}{D_k^M} \tag{2.42}$$

For hydrogen-air mixtures, the Lewis Number of hydrogen is typically less than 1 ($Le < 1$), which indicates that hydrogen diffuses faster than heat. This preferential diffusion is the fundamental cause of thermo-diffusive instabilities in lean hydrogen flames. In the early stages of this work, $Le = 1$ was assumed for benchmarking purposes. However, for instability analysis, a non-unity Lewis Number is essential to capture the effects of differential diffusion.

Karlovitz Number (Ka)
The Karlovitz Number quantifies the ratio of the chemical reaction timescale to the smallest turbulent timescale (Kolmogorov time scale) and is defined as

$$Ka = \frac{\tau_c}{\tau_\eta} \tag{2.43}$$

where τ_c is the chemical timescale and τ_η is the Kolmogorov timescale. While this parameter is highly relevant in turbulent combustion, its role is limited in the current study, which focuses on laminar flames. Nevertheless, it is included here for completeness.

Damköhler Number
The Damköhler Number compares the characteristic flow (or convective) timescale to the chemical reaction timescale:

$$Da = \frac{\tau_{flow}}{\tau_c} \tag{2.44}$$

where τ_{flow} is the flow timescale and τ_c is the chemical timescale. Da indicates whether the flame behaves as a thin laminar flamelet (Da > 1) or a thicker flame influenced by turbulence (Da < 1). In the current laminar study, Da serves primarily as a reference parameter.

2.3. Hydrogen Flame Instabilities

Hydrogen flames are susceptible to a range of physical instabilities that influence flame propagation, structure, and stability. Among these, thermo-diffusive instability plays the most critical role in lean premixed hydrogen combustion, which is the focus of this study. The primary instability modes are outlined below:

1. **Thermo-Diffusive Instability:** This instability arises due to hydrogen's low Lewis number ($Le < 1$), meaning it diffuses significantly faster than heat. This imbalance causes local enrichment and flame speed variations, leading to cellular flame structures, tip splitting, and unsteady propagation. Thermo-diffusive instability is particularly pronounced in lean hydrogen-air mixtures and plays a major role in defining flame curvature, stretch response, and overall flame stabilisation behaviour.
2. **Hydrodynamic Instability (Darrieus–Landau):** Caused by the density jump across the flame front, this instability leads to wrinkling and surface growth of the flame. While it contributes to flame area enlargement and potentially accelerates combustion, it is more relevant in turbulent regimes and is not directly studied in this work.

3. **Buoyancy Instability (Rayleigh–Taylor):** This occurs due to gravity acting on the density difference between the lighter burnt gases and the heavier unburnt mixture. It is primarily a concern in vertical flames or microgravity environments and does not apply to the counterflow configuration used in this study.

4. **Thermoacoustic Instability:** Resulting from the coupling between unsteady heat release and pressure fluctuations, this instability is prominent in confined systems such as gas turbines or rocket engines. It is not considered here, as acoustic feedback and confinement effects are not included in the numerical setup.

While multiple instability mechanisms can affect hydrogen flames, this study focuses exclusively on thermo-diffusive instability, which is dominant under lean, premixed, low-Mach conditions. For an extensive discussion of intrinsic flame instability mechanisms across different fuels, the reader is referred to Oppong et al. [12] and Lieuwen [13].

2.3.1. Instability Evaluation Parameters

Understanding flame instability requires analysing how a premixed flame responds to external strain, preferential diffusion, and curvature effects. Several key parameters govern these behaviours, particularly in hydrogen-air systems where differential diffusion effects are pronounced due to hydrogen's low molecular weight. In this study, we focus on four primary parameters: the Lewis number (Le), flame thickness (δ), stretch rate (κ), and flame response metrics such as the Markstein length (L_b) and Markstein number (Ma). These quantities are essential for interpreting the onset and evolution of thermo-diffusive instabilities in laminar premixed counterflow flames, and they form the basis for quantitative comparison across different magnetic field configurations.

Previous studies, such as Oppong et al. (2022) [12] and Law (1989) [14], have highlighted the role of these parameters in governing flame stability. In particular, Le and L_b are recognised as critical in characterising the influence of preferential diffusion and stretch-induced flame response, while δ and κ define the spatial and kinematic scales over which these effects manifest. Unlike turbulent regimes where parameters like the Karlovitz number (Ka) are more prominent, the present work focuses exclusively on laminar flames, where these four parameters capture the dominant instability mechanisms relevant to hydrogen combustion.

Lewis Number

The Lewis number (Equation 2.42) is a dimensionless quantity that describes the ratio of thermal diffusivity to mass diffusivity for a given species. In the context of hydrogen-air flames, the Lewis number of hydrogen is typically much less than one ($Le < 1$), owing to the extremely high mass diffusivity of hydrogen relative to its thermal diffusivity.

This low Lewis number causes preferential diffusion of hydrogen ahead of the flame front, leading to local enrichment in the reaction zone. As a result, regions of the flame can become locally more reactive, which increases the local flame speed and introduces instability. This behaviour is a defining characteristic of thermo-diffusive instability, particularly in lean hydrogen-air mixtures [12], [14].

In counterflow flames, where the strain rate is externally imposed and the flame remains steady and approximately one-dimensional, the effects of preferential diffusion become even more evident. The flame's response to curvature and stretch is strongly modulated by Le, with $Le < 1$ flames exhibiting higher sensitivity and greater instability growth compared to unity Lewis number flames. This manifests as changes in flame location, flame speed, and local burning behaviour as the applied strain varies. In this study, simulations are performed using both unity and non-unity Lewis number configurations to isolate and quantify the effects of preferential diffusion under varying magnetic field conditions.

Flame Thickness

Flame thickness is a fundamental metric describing the width of the reaction zone, where steep gradients in temperature and species concentrations occur. It plays a central role in defining the flame's sensitivity to curvature, strain, and differential diffusion. Thin flames are more prone to local extinction and instability, particularly under strong stretch, as they offer less diffusive buffering against perturbations [14].

Hydrogen flames typically exhibit extremely thin flame fronts due to hydrogen's low molecular weight and high mass diffusivity. This results in sharp thermal and concentration gradients, enhancing both hydrodynamic and thermo-diffusive instabilities under strain. As a result, flame thickness becomes a critical scaling parameter when evaluating flame stability, especially in strained configurations like counterflow flames.

Flame thickness can be defined in multiple ways, each suited to different modelling needs. The most common

definitions are:

$$\delta_d = \frac{\alpha}{S_L} \quad \text{(diffusive flame thickness)} \tag{2.45}$$

$$\delta_t = 2\frac{\alpha}{S_L}\left(\frac{T_a}{T_u}\right)^{0.7} \quad \text{(transport-based thickness)} \tag{2.46}$$

$$\delta_{tg} = \frac{T_a - T_u}{|\nabla T|_{\max}} \quad \text{(thermal flame thickness)} \tag{2.47}$$

Here, S_L is the laminar flame speed, α is the thermal diffusivity of the unburnt mixture, T_u is the unburnt temperature, and T_a is the adiabatic flame temperature. δ_d is a theoretical estimate based on diffusion scaling, δ_t accounts for thermophysical scaling effects, and δ_{tg} is derived directly from temperature gradients.

In this study, the thermal flame thickness (δ_{tg}) is used for all post-processing and non-dimensionalisation. This choice is motivated by its direct accessibility from simulation data and its suitability in capturing local flame structure under varying conditions. Unlike δ_d and δ_t, which rely on assumed constant transport properties, δ_{tg} reflects the actual resolved temperature field and therefore provides a more accurate estimate of the active flame zone in spatially varying or magnetically modified flows.

Kinematic Stretch Rate

Stretch rate is a fundamental parameter used to quantify the rate of deformation of the flame surface due to fluid flow. It describes the total kinematic influence of the flow field on the flame front, accounting for both velocity divergence and flame curvature. In premixed flames, and particularly in counterflow configurations, stretch rate plays a central role in evaluating flame sensitivity to flow-induced strain [12], [14].

The *kinematic stretch rate* κ is most generally defined as the normalised rate of change of an infinitesimal flame surface area element [14]:

$$\kappa = \frac{1}{A}\frac{dA}{dt} = \nabla_t \cdot \vec{v}_t + (\vec{v}_F - \vec{v})(\nabla \cdot \hat{n}) \tag{2.48}$$

where A is the flame surface area, $a_t = \nabla_t \cdot \vec{v}_t$ is the tangential strain, $\vec{v}_F$ is the flame speed in the laboratory frame, $\vec{v}$ is the local flow velocity and $\hat{n}$ is the unit normal vector to the flame front, oriented toward the unburnt gases. This form of the stretch rate captures both the volumetric expansion and the tangential strain at the flame surface [31]. The flame normal is computed from the progress variable C as:

$$\hat{n} = -\frac{\nabla C}{|\nabla C|} \tag{2.49}$$

Following the surface-kinematics framework of Law et. al. [14], κ can be decomposed into tangential strain within the flame surface and curvature-induced stretching due to normal propagation. Using the surface divergence identity for a smooth surface embedded in $\mathbb{R}^3$:

$$\nabla_t \cdot \vec{A}_t = \nabla \cdot \vec{A} - \hat{n} \cdot \nabla\vec{A} \cdot \hat{n}$$

and applying it to $\vec{A} = \vec{v}$, the tangential strain rate a_t is given by

$$a_t = \nabla \cdot \vec{v} - \hat{n} \cdot \nabla\vec{v} \cdot \hat{n} \tag{2.50}$$

This quantity measures the in-surface expansion or compression of the flame sheet due to the surrounding flow.

In the context of premixed flames, the flame displacement speed S_D is defined as the relative normal velocity of the flame front with respect to the unburnt mixture:

$$S_D = \vec{v}_F \cdot \hat{n} - \vec{u} \cdot \hat{n}$$

In steady flames observed in the laboratory frame, $\vec{v}_F = 0$, and the definition reduces to:

$$S_D = -\vec{v} \cdot \hat{n}$$

The full kinematic stretch rate can therefore be written compactly as:

$$\kappa = a_t + S_D(\nabla \cdot \hat{n}) \tag{2.51}$$

Here, a_t captures the tangential (flow-induced) stretch, while $S_D(\nabla \cdot \hat{n})$ accounts for curvature-propagation coupling. This decomposition is consistent with the theoretical treatments of Trouv'e [32] and Poinsot & Veynante [31], and is widely used in instability analysis for laminar and turbulent premixed flames.

This decomposition allows the stretch rate to be interpreted in terms of both flame surface curvature and tangential velocity effects. It is especially relevant in counterflow flames, where tangential strain dominates due to opposing jet flows, and curvature terms can be modified indirectly by flow or external magnetic influences. The above formulation is widely adopted in numerical studies of premixed flame instability and is used throughout this work to analyse flame dynamics under varying strain and magnetic conditions [32].

Markstein Length and Markstein Number

The Markstein length (L_b) is a key parameter used to quantify the sensitivity of a premixed flame to flow-induced stretch. It characterises how the local flame speed responds to changes in the stretch rate (κ), and thus serves as a measure of flame stability in strained configurations. Formally, it is defined as the slope of the flame speed versus stretch rate curve:

$$L_b = -\frac{dS_D}{d\kappa} \tag{2.52}$$

where S_D is the flame displacement speed and κ is the total stretch rate. A positive Markstein length indicates that the flame speed decreases under positive stretch (i.e., stabilising behaviour), while a negative L_b implies that stretch accelerates the flame, promoting instability growth. Hydrogen-air flames, especially under lean conditions with $Le < 1$, typically exhibit negative Markstein lengths [12], [14].

To allow for non-dimensional comparison across different flame conditions, the Markstein number (Ma) is introduced by normalising L_b with the flame thickness (δ):

$$Ma = \frac{L_b}{\delta} \tag{2.53}$$

The Markstein number provides a scale-independent measure of stretch sensitivity. Flames with large negative Ma are highly unstable to strain, while $Ma > 0$ indicates damping of instability due to flame response. Since both L_b and δ vary with equivalence ratio, mixture composition, and magnetic field influence, Ma serves as a compact metric for assessing flame stability trends in this study.

These parameters, the Lewis number, flame thickness, stretch rate, and Markstein metrics, form the foundational framework for evaluating premixed flame instabilities under strain. Each quantifies a specific physical mechanism that contributes to instability growth or suppression, whether through preferential diffusion, local heat and mass transport, or the kinematic response of the flame to imposed flow gradients. In the context of lean hydrogen-air combustion, where thermo-diffusive instability dominates, these quantities are particularly sensitive and must be interpreted carefully.

In the next section, the laminar counterflow premixed flames are examined as a canonical configuration for isolating and analysing these effects. This geometry allows precise control over strain rate and offers a one-dimensional structure ideal for evaluating the influence of magnetic fields on transport, flame speed, and instability behaviour.

2.4. Laminar Counterflow Flames

Laminar counterflow premixed flames provide a canonical configuration for studying flame behaviour under well-defined strain conditions. Their one-dimensional structure, geometric symmetry, and precise strain control make them highly suitable for isolating the effects of thermo-diffusive instability, particularly in lean hydrogen-air mixtures. Unlike spherically expanding or turbulent flames, counterflow configurations enable a steady and spatially resolved analysis of flame–flow interaction. This enables the systematic evaluation of how diffusion, stretch, and curvature impact flame structure and stability.

In addition to their analytical simplicity, counterflow flames are widely used in experimental and numerical studies for validating reaction mechanisms, transport models, and instability criteria. Their sensitivity to strain makes them especially relevant for investigating preferential diffusion effects in hydrogen combustion. For these reasons, the counterflow premixed flame is selected as the base configuration in this study for evaluating the influence of magnetic fields on flame stability and transport dynamics.

2.4.1. Strain Effects in Restrained Counterflow Flames

A premixed counterflow flame represents a canonical configuration for investigating flame–flow interactions in the presence of strain. In this geometry, opposing streams of unburnt reactants and hot products (or an inert

surrogate) create a stagnation region near the domain centre, where the flame is stabilised. Unlike freely propagating flames, the flame in a counterflow arrangement is spatially restrained; it cannot shift its position to adjust to changing flow conditions. As a result, the full effect of the imposed stretch is absorbed by the flame structure itself, making this configuration particularly well-suited for studying the role of transport and strain-induced instabilities [14].

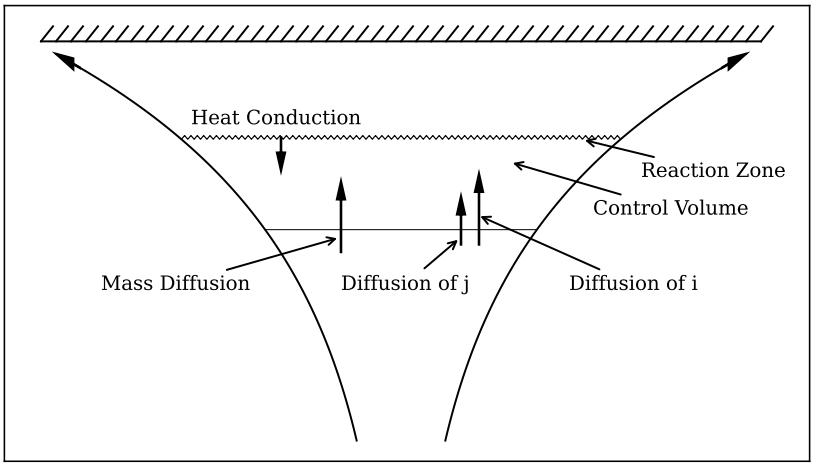

Figure 2.1: Schematic of a restrained premixed counterflow flame, illustrating the diffusion of species and heat conduction in the reaction zone for $Le < 1$. Adapted from C.K. Law [14]

In premixed hydrogen-air flames, the Lewis number (Le) plays a critical role in determining the behaviour of the flame front. Figure 2.1 describes this behaviour with a visual context. For $Le < 1$, hydrogen diffuses much faster than heat, leading to preferential diffusion where fuel (H_2) is transported into the reaction zone more rapidly than thermal energy can escape. Moreover, a positive curvature causes heat to escape the control volume, dissipating thermal energy, while species diffusion enriches the reaction zone with chemical energy [14]. An increase in the tangential stretch in a restrained flame results in the thinning of the flame surface, thus steepening all the field gradients, resulting in the enhanced diffusion of all the fluxes [14]. With $Le < 1$, the relative chemical energy increment in the reaction zone becomes higher than the heat dissipation due to conduction, resulting in the increase in reaction rates and hence, the flame speed.

This effect is also observed with differential diffusion, where the diffusivity of hydrogen is much higher than that of oxygen. As the strain rate increases, the differential diffusion effect becomes more pronounced, particularly in hydrogen-air flames. Hydrogen, being the faster-diffusing species, accumulates in the reaction zone, leading to an increase in the local stoichiometric ratio. This enrichment effect results in a richer reaction mixture, which in turn accelerates the combustion process and causes an increase in the flame speed.

The Markstein length (L_b) provides a useful measure for quantifying the sensitivity of flame speed to changes in stretch. It captures the combined effects of differential diffusion and stretch-induced flame response. As shown in Figure 2.2, a positive L_b reduces the displacement speed, whereas a negative L_b indicates that positive stretch increases the flame speed, particularly in $Le < 1$ flames [14]. As discussed earlier, increased strain steepens the species and temperature gradients, enhancing the diffusive fluxes and reaction rate. The Markstein length essentially summarises how these complex interactions impact the overall flame dynamics, providing a single scalar that links the flame's response to stretch with changes in local burning rates and flame structure [33].

When a slight perturbation occurs at the flame front, the curvature of the surface changes, leading to flame wrinkling. In $Le < 1$ flames, this wrinkling causes a positive feedback loop: as curvature increases, the strain on the flame surface also increases, which in turn accelerates the flame speed. The increase in flame speed further amplifies the curvature, making the flame more unstable. This positive feedback mechanism destabilises the flame front and makes it prone to flashbacks, with the growing instability leading to uneven propagation and increased flame wrinkling. Table 2.1 summarises the flame response in different stretch regimes for $Le < 1$ counterflow flame. Understanding these dynamics, particularly through the Markstein length, is essential for exploring potential strategies for flame stabilisation. The following section will discuss technological advancements and the various methods that have been explored to stabilise flames and control instability.

Stretch Regime	Flame Response	Key Indicators
Low to Moderate Stretch	Local ϕ shifts toward stoichiometry; burning intensifies.	$T_b > T_{ad}$, S_L increases, negative flame speed.
Critical Stretch (Ka $\approx$ 1)	Diffusive fluxes and reaction rate reach their maximum.	Peak in T_b, mass burning rate increases.
High Stretch	Residence time become insufficient for complete combustion and flame quenching.	Drop in T_b, incomplete H_2 consumption, extinction near stagnation plane.

Table 2.1: Flame response to increasing stretch in restrained $Le < 1$ counterflow configuration.

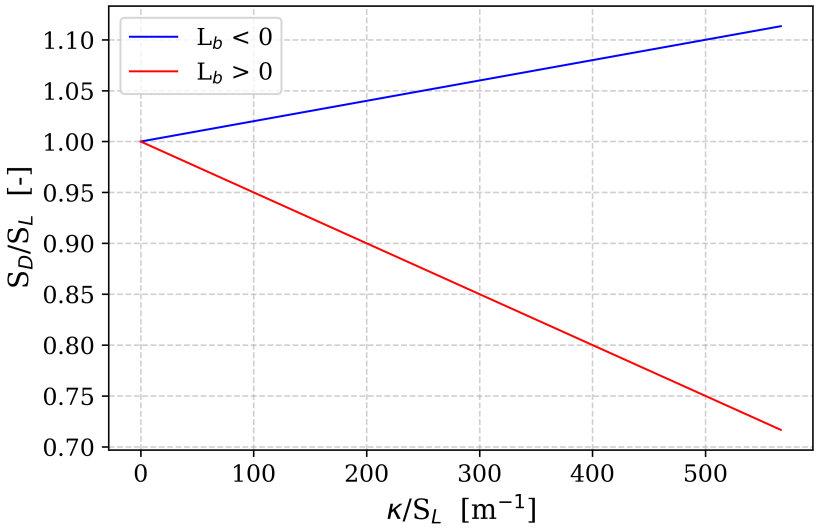

Figure 2.2: Displacement Speed variation with Stretch Rate for positive and negative L_b

2.5. Technological Advancements

Over time, various technological innovations have been introduced to address instabilities in hydrogen flames, improving combustion efficiency, reducing emissions, and enhancing stability in hydrogen combustion systems. The primary strategies explored are:

1. **Lean Premixed Combustion Techniques:** Lean premixed combustion reduces flame temperature, mitigating thermoacoustic instabilities and improving flame stability in hydrogen gas turbines and low-NOx burners [16].
2. **Advanced Fuel Injection Strategies:** Micromix burners and multi-point injection systems improve fuel-air mixing, reducing the effects of hydrodynamic and thermo-diffusive instabilities. These systems are widely used in aerospace hydrogen propulsion and industrial burners [16].
3. **Passive Control via Hydrogen Piloting:** Introducing hydrogen as a pilot fuel stabilises flames and reduces the risk of extinction due to buoyancy-driven instabilities. However, it can increase NOx emissions, which is mitigated using staged combustion [34].
4. **Active and Dynamic Flame Stabilisation:** Active control strategies, such as fuel flow modulation and electromagnetic flame stabilisation, are employed to mitigate thermoacoustic instabilities. These strategies dynamically adjust combustion parameters to reduce instabilities in hydrogen flames [35].
5. **Computational Simulations and AI-Driven Combustion Modelling :** High-fidelity CFD and AI-driven modelling are used to optimise fuel injection and flame conditions, reducing flame wrinkling and flashback in hydrogen combustion systems [36].

Active control via magnetic fields offers a promising solution to mitigate thermo-diffusive instability in hydrogen flames. By exploiting the paramagnetic properties of oxygen (O_2) and diamagnetic properties of hydrogen (H_2), magnetic fields can selectively enhance the diffusion of oxygen into the flame while slowing the diffusion

of hydrogen [17]. This adjustment can address the imbalance in diffusivities that leads to differential diffusion effects. By increasing oxygen diffusion and decreasing hydrogen diffusion, magnetic fields can help narrow the differential diffusion gap, reducing the sensitivity of flame speed to stretch. This approach can be effective particularly in lean hydrogen-air mixtures, where lean conditions make the flame more prone to thermo-diffusive instabilities [37]. Magnetic control, therefore, offers a method to actively adjust the transport properties of the flame, preventing extreme acceleration of the flame speed and improving combustion stability.

In conclusion, while various strategies have been explored to stabilise hydrogen flames, magnetic control stands out for its potential to directly address thermo-diffusive instability by manipulating the transport properties of fuel and oxidiser. The ability to enhance oxygen diffusion and regulate hydrogen diffusion through magnetic fields opens up new possibilities for flame stabilisation, particularly in lean hydrogen-air mixtures. The next chapter will delve into the existing literature on the use of magnetic fields in combustion systems, reviewing key studies and methodologies that have explored this innovative approach. It will also highlight the current gaps in research, particularly the need for further exploration into the effectiveness of magnetic control for instability suppression in real-world combustion systems and how these techniques can be scaled for practical application.

3

Magnetic Control of Flames

The manipulation of combustion dynamics through magnetic fields represents a frontier in flame control, primarily leveraging the paramagnetic properties of oxygen and the intricate interactions between combustion species and electromagnetic forces. A critical component in this process is the hydroxyl radical (OH), a highly reactive species central to flame propagation, heat release, and radical chain reactions. In most combustion systems, the OH radical serves as a reliable indicator of the flame front, delineating regions of peak heat release and intense chemical activity [38]. Consequently, precise control over the spatial distribution of OH radicals offers a direct pathway to modify the flame front's position, thereby enabling targeted alterations to the overall flame structure and stability.

In a laminar counterflow premixed flame, the flow field exhibits varying stretch rates, with the highest strain occurring near the stagnation plane. For hydrogen flames with a low Lewis number ($Le < 1$), quenching under normal operating conditions is unlikely; extinction typically occurs only at very high strain rates, where the flame thickness is reduced to the extent that the residence time becomes insufficient for complete combustion. From a pollutant-formation perspective, elevated strain rates are advantageous for NOx reduction, as they promote reduced residence time and radical redistribution on the flame surface [39]. Moreover, intensive strain in lean premixed hydrogen flamelets helps to mitigate the effects of preferential diffusion [40]. Magnetic control strategies can therefore provide an additional auxiliary stabilising mechanism in lean premixed hydrogen flame.

One potential approach is the magnetic manipulation of OH radical concentrations. Since OH is weakly paramagnetic, its transport can be subtly influenced by external magnetic field gradients, enabling targeted redistribution within the flame [17], [41]. By strategically controlling the OH radical field, it may be possible to regulate the local heat release rate and reaction zone structure, thereby influencing flame speed behaviour in high-strain regions. This could offer a non-intrusive means of suppressing stretch-induced instability growth while retaining the emission benefits associated with high strain. For $Le < 1$ hydrogen flames, such a magnetohydrodynamic (MHD) based approach represents a promising pathway to simultaneously optimise flame stability, control flashback risk, and reduce pollutant formation. By judiciously combining MHD principles with advanced flame stabilisation techniques, this approach holds considerable promise for optimising flame positioning and significantly enhancing combustion efficiency.

3.1. Theoretical Foundations of Magnetic Flame Control

The interaction between magnetic fields and flames arises from the coupled principles of electromagnetism and fluid dynamics, particularly with respect to the behaviour of paramagnetic species and, to a lesser extent, charged particles in reacting flows. Following the formulation of Yamada et al. (2003) [17], three principal mechanisms have been identified through which magnetic fields may influence combustion: modification of reaction kinetics, the Lorentz force, and the Kelvin force [42], [43].

The Lorentz force describes the effect of electric and magnetic fields on moving charged particles [44], whereas the Kelvin force results from the interaction between a magnetic field gradient and the magnetic dipole moment of a species [45]. Under typical combustion conditions, the influence of magnetic fields on chemical reaction rates is generally considered negligible [17], [46]. Furthermore, experiments in which the magnetic field direction was reversed by altering the electromagnet current reported no measurable shift in flame position [47], indicating that Lorentz forces play an insignificant role in static-field flame control.

Consequently, the effects of static magnetic fields on combustion are primarily attributed to Kelvin forces acting on paramagnetic species, most notably molecular oxygen, which modify the surrounding fluid motion and, by extension, the flame structure. For a species i, the Kelvin force is expressed as:

$$\vec{f_i} = \frac{1}{2\mu_0}\chi_i \nabla(\vec{B}^2) + \vec{g} \tag{3.1}$$

where μ_0 is the permeability of free space, χ_i is the magnetic susceptibility, $\vec{B}$ is the magnetic field vector, and $\vec{g}$ is the gravitational acceleration. The magnetic susceptibility χ_i for a paramagnetic species is given by:

$$\chi_i = \frac{N_A g_L^2 \mu_B^2 S_i(S_i+1)\mu_o}{3kTm_i} \tag{3.2}$$

where N_A is Avogadro's number, g_L is the Landé g-factor, μ_B is the Bohr magneton, S_i is the total spin quantum number, k is the Boltzmann constant, T is the temperature, and m_i is the molar mass of species i.

From Equation 3.2, it is evident that the Kelvin force in Equation 3.1 is proportional to both the gradient of the square of the magnetic field strength and the species' magnetic susceptibility. The susceptibility increases with the spin quantum number and decreases with temperature, implying that species with higher S_i values at lower T experience stronger forces. The spin quantum numbers for the main reacting species are listed in Table 3.1, where non-zero values indicate paramagnetic behaviour. The Kelvin force, therefore, acts selectively on paramagnetic

i	H_2	H	H_2O	OH	H_2O_2	HO_2	O	O_2	O_3
S_i	0.0	0.5	0.0	0.5	0.0	0.5	1.0	1.0	0.0

Table 3.1: Spin quantum number S_i of the reacting species. Non-zero values indicate paramagnetic behaviour.

species, driving preferential mass transport. This modifies local species concentrations, influences reaction rates, redistributes heat release, and alters flame structure.

To incorporate these effects into modelling, the governing equations for reacting flows are extended to include the magnetic body force. For low-Mach-number combustion, the momentum equation becomes:

$$\rho\frac{\partial\vec{v}}{\partial t} + (\vec{\phi}\cdot\nabla)\vec{v} = -\nabla p + \nabla\cdot\tau + \rho\sum_i Y_i\vec{f_i} \tag{3.3}$$

where ρ is the density, $\vec{v}$ is the velocity vector, $\vec{\phi} = \rho\vec{v}$ is the mass flux, p is the pressure, τ is the viscous stress tensor, Y_i is the species mass fraction, and $\vec{f_i}$ is given by Equation 3.1. The summation accounts for the cumulative body force weighted by species mass fractions.

The species conservation equation, accounting for magnetic-field-induced transport, is:

$$\rho\frac{\partial Y_i}{\partial t} + (\vec{\phi}\cdot\nabla)Y_i = -\nabla\cdot\vec{J_i} + \dot{\omega}_i \tag{3.4}$$

where $\vec{J}i$ is the total diffusion flux and $\dot{\omega}i$ is the net rate of production of species i by chemical reactions. The diffusion flux is decomposed into Fickian and magnetic components:

$$\vec{J_i} = \underbrace{\vec{J}_{Y,i}}_{\text{Fickian Diffusion Flux}} + \underbrace{\vec{J}_{M,i}}_{\text{Magnetic Diffusion Flux}} \tag{3.5}$$

with

$$\vec{J}_{Y,i} = -\rho D_i^m \nabla Y_i \tag{3.6}$$

$$\vec{J}_{M,i} = \rho D_i^m \vec{M}_i \tag{3.7}$$

Here, D_i^m is the mixture-averaged diffusion coefficient, and $\vec{M}_i$ is the magnetophoretic gradient factor:

$$\vec{M}_i = \frac{m_i}{m}\frac{\rho}{p}\sum_{j\neq i} Y_i Y_j(\vec{f_i} - \vec{f_j}) \tag{3.8}$$

which can be rewritten as:

$$\vec{M}_i = \frac{m_i Y_i}{m} \frac{\rho}{p} \left(\vec{f}_i - \sum_j Y_j \vec{f}_j \right)$$

For non-unity Lewis number conditions, the magnetic diffusion flux also induces an interdiffusive heat flux:

$$\vec{q}_{J_M} = \sum_i h_i \vec{J}_{M,i} \tag{3.9}$$

where h_i is the sensible enthalpy of species i.

In addition, the magnetic body force performs mechanical work on the flow, which is included in the modified energy equation for magnetic-field-influenced combustion:

$$\frac{\partial h}{\partial t} = -(\vec{\phi} \cdot \nabla)h - \nabla \cdot \vec{q} - \sum_i h_i \dot{\omega}_i + \underbrace{\sum_i \vec{f}_i \cdot \vec{J}_i}_{\text{Body Force Work}} \tag{3.10}$$

where the heat flux $\vec{q}$ is decomposed into conductive and diffusive components:

$$\begin{aligned} \vec{q} &= \vec{q}_{\text{cond}} + \vec{q}_J \\ \vec{q}_{\text{cond}} &= -\lambda \nabla T \\ \vec{q}_J &= \vec{q}_{J_Y} + \vec{q}_{J_M} \\ \vec{q}_{J_Y} &= \sum_i h_i \vec{J}_{Y,i} \end{aligned}$$

This framework fully integrates Kelvin-type magnetic forces into the conservation equations for momentum, species, and energy, enabling accurate prediction of flame behaviour under the influence of applied magnetic fields.

3.2. Developments in Magnetic Flame Control

The historical trajectory of magnetic flame control research began with an initial curiosity regarding the influence of paramagnetic oxygen on combustion dynamics, with early investigations predominantly focusing on hydrocarbon flames [48], [49]. The observed capacity of magnetic fields to modify flame propagation, stability, and emissions spurred further in-depth inquiries into radical interactions and gas flow alterations under magnetic influence. Pivotal studies meticulously explored the alignment of paramagnetic oxygen molecules, demonstrating their ability to reshape flame morphology and alter combustion rates [50], [51]. Concurrently, other research endeavours investigated the impact of magnetic gradients on critical radicals such as OH and HO_2, highlighting their profound role in reaction kinetics and heat release [17], [18].

Beyond the direct effects of paramagnetic oxygen, the enhancement of flame stability through magnetic field interactions has also been a significant area of exploration. It has been discovered that Kelvin-Helmholtz instabilities, commonly observed in flames, can be effectively counteracted by magnetic field interactions, leading to buoyancy-driven stabilisation mechanisms [47]. Furthermore, the intricate interplay between oxidiser composition and magnetic influence has been rigorously examined, particularly in the context of turbulence suppression and the reduction of soot formation [52]. These collective findings unequivocally underscore the considerable potential of magnetic fields in both controlling flame stabilisation and mitigating harmful emissions, thereby paving the way for more specialised studies on hydrogen combustion and its unique thermo-diffusive instability characteristics.

3.2.1. Early Theoretical Foundations & Experiments

The foundational research in magnetic flame control meticulously established the groundwork for comprehending how magnetic fields exert their influence on combustion dynamics, radical transport, and flame stability. Initial investigations primarily centred on hydrocarbon flames, where the inherent presence of paramagnetic oxygen and various combustion radicals facilitated measurable interactions under the application of external magnetic fields. Additionally, researchers investigated the impact of magnetic fields on fluid dynamic instabilities, such as Kelvin-Helmholtz waves and turbulence-driven flame wrinkling, thereby providing deeper insights into the mechanisms of magnetically induced stability.

- **First Observations:** One of the earliest systematic investigations into the effects of magnetic fields on combustion velocity analysed the response of different hydrocarbon fuels to external magnetic fields [48]. The results revealed that combustion velocity exhibited nonlinear variations, with certain fuels experiencing an increase in burning rates while others showed a decrease at specific magnetic field intensities. These variations strongly suggested that the effects of magnetic fields on flames are fuel-dependent and are significantly influenced by the interactions of radicals with the applied field. The observed changes were attributed to magnetic resonance effects and radical realignment, which critically impacted flame propagation and stabilisation mechanisms.
- **Paramagnetic Oxygen Alignment & Radical Transport:** The role of oxygen molecule alignment within magnetic gradients was further elucidated, leading to the identification of the ”wall of oxygen” effect, a phenomenon where aligned oxygen molecules create a localised density barrier that effectively redirects flames [49]. Experimental findings unequivocally demonstrated that magnetic fields altered both flame shape and propagation direction, particularly at lower gas flow rates, rendering flame behaviour highly dependent on localised oxygen concentration modifications. Subsequent studies further corroborated that the redistribution of paramagnetic oxygen within magnetic gradients significantly influences flame structure and stability [50]. Moreover, a deeper analysis of Kelvin-Helmholtz instabilities in flames indicated that magnetic fields possess the capability to suppress the growth of such instabilities and reinforce buoyancy-driven stabilisation mechanisms, thereby offering a novel perspective on flame stabilisation under magnetic influence [47].
- **Hydrocarbon Combustion Velocity & Turbulence Effects:** Investigations into the influence of magnetic fields on reaction pathways and radical transport, specifically concerning OH and HO_2 recombination mechanisms, revealed that magnetic fields altered species diffusion rates. This led to observable variations in combustion efficiency and NOx emissions [18], [19], [46]. The strategic application of magnetic fields was found to modify flame temperature profiles, resulting in a notable 60% reduction in NOx formation [19]. This significant finding strongly supports the potential of magnetic fields as a non-intrusive strategy for emissions control. Furthermore, evidence suggested that the interaction between oxidiser composition (e.g., CO_2 versus N_2) and magnetic fields influenced soot formation and turbulence-driven instabilities, thereby highlighting the crucial role of external magnetic forces in both turbulence suppression and overall combustion optimisation [52].

These foundational studies collectively provided compelling early evidence that magnetic fields can actively influence a wide array of combustion parameters. This realisation subsequently propelled further investigations into radical realignment, species transport, and the modification of flame stability. The stabilisation of combustion instabilities, the suppression of flame wrinkling, and the modification of turbulence under the influence of magnetic fields continue to represent critical areas of ongoing research, particularly within hydrogen combustion systems where thermo-diffusive instabilities are predominantly observed.

3.2.2. Fundamental Mechanisms

As the body of experimental evidence steadily grew, researchers progressively shifted their focus towards elucidating the intricate underlying physical and chemical mechanisms responsible for the observed magnetic effects on flames. These fundamental mechanisms encompass a range of phenomena, including modifications to radical reaction pathways, alterations in oxygen transport, and complex electromagnetic interactions with charged species present within the combustion environment.

1. **Radical Reactions & Transport:** Numerous studies have convincingly demonstrated that magnetic fields exert a significant influence on electron spin interactions within radical recombination reactions. This influence, in turn, alters reaction rates and modifies energy transfer mechanisms. Specifically, it has been shown that singlet-triplet intersystem crossing (ISC) can modify the formation rates of OH and HO_2 radicals, thereby directly impacting heat release and overall flame stability [18]. Furthermore, investigations into the redistribution of OH radicals under the influence of magnetic fields in hydrogen flames have confirmed that both combustion intensity and flame positioning are directly affected by these radical transport modifications [17]. These findings collectively suggest that the kinetics of chemical reactions and the propagation of flames can be actively controlled through the judicious application of magnetic fields.
2. **Oxygen Transport & Flow Modifications:** The pivotal role of oxygen realignment under magnetic fields in altering gas flow patterns, flame positioning, and stability has been extensively investigated [49]. Research findings have consistently indicated that magnetic gradients possess the capability to redirect combustion zones by strategically modifying local oxygen concentrations, leading to discernible changes in

flame structure and propagation characteristics. Further comprehensive investigations have confirmed that oxygen redistribution significantly impacts flame stability, particularly in diffusion flames where oxygen transport plays a dominant role in the overall combustion dynamics [50], [51]. Given these observed effects, it has been posited that hydrogen flames, which are primarily diffusion-driven due to their inherently low Lewis number ($Le < 1$), could experience analogous stabilisation effects when subjected to applied magnetic fields.

3. **Electromagnetic Effects on Charged Species:** Research has unequivocally demonstrated that ionised radicals, such as OH^+, O^+, and H^+, exhibit selective transport modifications under the influence of applied electromagnetic forces. This leads to observable shifts in flame structure and the distribution of radicals [17], [20]. Additionally, investigations into counterflow premixed flames subjected to magnetic fields have revealed that altered radical concentrations can profoundly influence reaction dynamics, further substantiating the feasibility of magnetically driven combustion control [53]. These findings collectively indicate that magnetic fields can be effectively utilised as an external force to precisely manipulate specific regions within a flame, thereby potentially enabling real-time control over combustion behaviour.

The comprehensive study of magnetic field interactions with combustion has yielded invaluable insights into the mechanisms governing flame stabilisation, radical transport, and emissions control. With a progressively deeper understanding of these intricate mechanisms, research efforts have naturally expanded towards practical applications, with a particular focus on how magnetic fields influence flame speed, structure, and the formation of pollutants. The subsequent section will delve into these key research domains, systematically categorising their impact on combustion dynamics, stabilisation, and the reduction of harmful emissions.

3.3. Key Research Domains

Magnetic fields exert a profound influence on fundamental combustion properties, including flame speed, structure, stability, and emissions. Extensive research has consistently shown that external magnetic fields modify radical transport, alter reaction kinetics, and influence gas flow behaviour, culminating in observable changes in overall combustion dynamics. These multifaceted effects can be systematically categorised into three primary research domains:

1. **Flame Speed and Combustion Dynamics:** Magnetic fields directly impact burning rates and ignition properties by altering the transport and recombination processes of highly reactive species, such as OH and HO_2 radicals. This leads to discernible variations in flame velocity and overall combustion efficiency. Experimental diagnostics have provided direct, quantitative insights into how magnetic forces influence combustion speed, oscillatory behaviour, and ignition dynamics, thereby enabling the precise quantification of flame velocity shifts under diverse magnetic field conditions.
2. **Flame Shape Modification & Stability:** Magnetic gradients are instrumental in influencing flame structure by inducing bending, compression, or stabilisation of flame fronts. This action effectively reduces turbulence-driven instabilities and significantly improves both flame anchoring and liftoff control. The inherent ability of magnetic forces to counteract buoyancy-driven and shear-induced instabilities has stimulated further exploration into how flame morphology can be precisely controlled in both diffusion and premixed configurations.
3. **Emission Control & NOx Reduction:** Magnetic field-induced radical redistribution directly alters reaction pathways, consequently modifying flame temperature and oxygen availability. This has a significant impact on NOx formation and other pollutant emissions. Furthermore, the interactions between oxidiser composition and magnetic stabilisation have been meticulously examined as a potential strategy for controlling thermal radiation, mitigating soot formation, and reducing overall pollutant emissions in various combustion systems.

A thorough understanding of these critical research domains provides invaluable insight into how magnetic control can be strategically leveraged to optimise combustion efficiency, significantly enhance flame stability, and ultimately facilitate the development of cleaner, more sustainable energy solutions.

3.3.1. Effects on Flame Speed and Combustion Dynamics

Flame speed is directly and significantly influenced by the intricate interaction between reactive radicals (OH, HO_2) and applied magnetic fields, leading to observable and quantifiable changes in combustion velocity. Experimental studies have consistently demonstrated that flame propagation speed exhibits complex oscillatory

behaviour as a function of magnetic field intensity, indicating a nuanced dependence on radical redistribution and field strength. Changes in combustion velocity under magnetic influence have been rigorously validated through experimental techniques utilising advanced optical diagnostics, including Talbot interferometry and speckle pattern interferometry. These methods provide direct, high-fidelity measurements of flame speed modifications under various magnetic field strengths [54], [55]. These findings align with previous studies, where nonlinear variations in combustion velocity were observed, suggesting a resonance-like effect in combustion dynamics [46]. Additionally, it has been conclusively shown that magnetic fields modify flame velocity by altering the transport of OH and O radicals, thereby influencing heat release rates and ignition timing [19].

In the specific context of hydrogen flames, the application of magnetic fields results in discernible variations in ignition behaviour, underscoring the critical role of radical transport in determining flame propagation speed. It has been observed that hydrogen flames exhibit magnetic-field-dependent shifts in ignition characteristics, where flame speed changes in response to field intensity due to modifications in radical recombination rates and diffusion effects [17]. Numerical simulations further corroborate these experimental findings, demonstrating that combustion speed shifts under magnetic influence, thereby reinforcing observations made in counterflow flame configurations [20], [41]. These sophisticated computational models offer deeper insights into how magnetic fields influence local strain rates, flame stretch, and preferential diffusion effects in hydrogen-air combustion systems.

These collective studies confirm that magnetic fields can serve as a highly controllable parameter for modifying flame speed and ignition properties, thereby providing a potential non-intrusive method for influencing overall combustion efficiency. By actively redistributing reactive radicals, magnetic fields can be strategically leveraged to optimise ignition delay and burning velocity, opening new avenues for advanced combustion control in both hydrogen and hydrocarbon-based energy systems.

3.3.2. Flame Shape Modification & Stabilization

Flame shape and stability are profoundly influenced by how paramagnetic oxygen molecules and reactive radicals (OH, O_2) respond to externally applied magnetic fields. Magnetic field gradients induce directional shifts in flame position, affecting critical parameters such as flame liftoff height, bending, and compression. These alterations play a crucial role in either stabilising or destabilising combustion systems. The seminal ”wall of oxygen” effect, where aligned oxygen molecules create localised gas density gradients that modify flame behaviour and redirect combustion zones, was initially identified as a pivotal mechanism for magnetic flame control [49]. This phenomenon laid the fundamental groundwork for subsequent, more detailed studies on flame stabilisation under magnetic influence, particularly in configurations where buoyancy-driven and turbulence-induced instabilities significantly impact flame dynamics.

Subsequent research has expanded upon these foundational findings, consistently confirming that magnetic gradients can substantially improve flame anchoring and effectively reduce instability. It has been observed that flame stabilisation is significantly enhanced under applied magnetic fields, particularly in diffusion flames where oxygen transport is the dominant factor governing combustion dynamics [51]. Similarly, investigations into paramagnetic oxygen redistribution in magnetically influenced flames have demonstrated that flame stability is directly affected by modifications in anchoring conditions and turbulence-driven instabilities, further supporting the considerable potential of magnetic control in practical combustion systems [50]. The stabilisation of buoyancy-driven instabilities under magnetic influence has also been extensively explored, with findings indicating that flames subjected to high-gradient fields exhibit markedly improved resistance to instability growth and wrinkling effects [47].

For counterflow premixed flames, where strain and stretch rates are critically important, studies have demonstrated that flame bending and anchoring can be actively and precisely controlled using external magnetic fields [53]. This further supports the broad applicability of magnetic stabilisation techniques across a diverse range of combustion configurations. Theoretical analyses have also quantitatively assessed how gravity modification effects influence magnetically stabilised flames, revealing that flame liftoff characteristics and overall structure are highly sensitive to the intricate interaction between magnetic and gravitational forces [56]. Experimental validation of these theoretical predictions has been successfully achieved through non-intrusive optical diagnostics, including Talbot interferometry and speckle pattern interferometry, which have provided direct and accurate measurements of flame shape modifications under varying magnetic field strengths [54], [55].

These comprehensive studies collectively confirm that magnetic fields offer a novel and highly effective method for stabilising lifted or unsteady flames, thereby significantly reducing the risk of flame quenching and substantially improving overall combustion efficiency. By selectively redistributing oxygen and reactive radicals, turbulence-driven instabilities can be effectively mitigated, particularly in high-gradient magnetic fields.

This approach proves invaluable for advanced combustion applications, including hydrogen combustion and the development of low-emission energy systems.

3.3.3. Emission Control & NOx Reduction

The influence of magnetic fields on pollutant emissions has emerged as a central focus in the study of magnetically controlled combustion, with particular emphasis on the formation and subsequent reduction of NOx emissions. Research has consistently demonstrated that magnetic fields alter both flame temperature and radical distribution, thereby directly impacting the complex pathways of NOx formation. Experimental investigations have rigorously validated that NOx emissions can be significantly reduced under magnetic influence, with various studies reporting reductions of up to 60% under optimised conditions [19], [46]. These compelling findings indicate that the magnetic tuning of radical transport and oxidation chemistry provides a viable and alternative means for achieving low-emission combustion control.

The redistribution of key reactive radicals, such as OH and O_2, plays a crucial role in modifying the emission characteristics within magnetically influenced flames. Changes in oxygen availability and alterations in radical recombination kinetics under applied magnetic fields have been observed to directly influence NO_x formation, as variations in flame temperature directly affect the thermal NOx pathway [18]. Furthermore, the intricate interactions between oxidiser composition and magnetic influence have been identified as critical factors in controlling thermal radiation, mitigating soot formation, and reducing overall pollutant emissions. Studies have convincingly demonstrated that combining magnetic fields with variations in oxidiser composition (e.g., CO_2 versus N_2) can effectively modify flame chemistry, influencing both NOx formation and soot reduction [52]. These findings strongly suggest that magnetic field-assisted oxidiser control can be effectively utilised as a novel approach to emission optimisation.

Experimental validation of these NOx reduction mechanisms has been meticulously conducted using advanced optical diagnostics, enabling direct measurements of temperature gradients and precise radical transport modifications in magnetically controlled flames. The application of techniques such as Talbot interferometry and speckle pattern interferometry has provided quantitative data on temperature distributions and reaction zone shifts under magnetic fields, thereby supporting the observed trends in NOx emission control [54], [55]. These diagnostic tools have confirmed that temperature modulation through strategic radical redistribution plays a significant role in minimising NOx production, further reinforcing the considerable potential of magnetic fields as an effective tool for developing robust emissions reduction strategies.

These collective studies unequivocally confirm that magnetic fields provide a non-intrusive and highly effective method for NOx emissions control, offering a compelling alternative to traditional post-combustion treatment technologies. By actively modifying flame temperature, radical pathways, and oxidiser availability, magnetic tuning presents a unique opportunity for developing cleaner combustion technologies with optimised pollutant formation control.

3.4. Research Gaps in Magnetic Flame Control

Research concerning the effects of magnetic fields in combustion has predominantly focused on hydrocarbon-based flames, with extensive studies dedicated to paramagnetic oxygen interactions, diffusion flames, and the influence of varying magnetic field intensities [17], [19], [51]. While these studies have yielded invaluable insights into the magnetic control of combustion, they have primarily been conducted on co-flow configurations and diffusion flames, where oxygen transport plays a dominant role in the stabilisation mechanisms [20], [50]. However, hydrogen-premixed counterflow flames, which inherently exhibit thermo-diffusive instabilities due to their low Lewis number (Le < 1), remain significantly underexplored within the context of magnetic field interactions [18], [46].

Furthermore, while a considerable body of research has examined the role of magnetic field intensity, there remains a notable paucity of work on the effects of field orientation, gradient configurations, and comprehensive parametric variations in magnetically controlled flames [47], [52]. High-fidelity numerical models that effectively incorporate magnetohydrodynamic (MHD) effects into computational fluid dynamics (CFD) simulations are also largely absent, despite the clear potential to extend existing gravity-magnetic interaction models to advanced combustion modelling [56]. These identified gaps collectively provide the compelling motivation for the present study, which aims to investigate how magnetic field gradients can be strategically utilised to shift OH radicals towards lower-strain regions within an asymmetric hydrogen counterflow flame. This approach holds the promise of significantly enhancing flame stability and extending its operational range.

3.4.1. Hydrogen Premixed Counterflow Flames

The study of magnetic fields in combustion has historically focused on hydrocarbon flames, including systems based on CH_4, LPG, and gasoline, with comparatively fewer investigations dedicated to hydrogen combustion [17], [19], [51]. Existing research has extensively examined magnetic control in diffusion flames, particularly in co-flow configurations, where the effects of paramagnetic oxygen predominantly govern stabilisation mechanisms [20], [50]. These studies have convincingly demonstrated that the alignment of oxygen molecules under magnetic fields influences flame shape, propagation, and overall stability, thereby providing a robust foundation for further exploration of other flame configurations.

Despite these significant advancements, hydrogen-premixed counterflow flames remain largely unexamined under the influence of magnetic fields. While hydrogen combustion fundamentally differs from hydrocarbon flames due to its exceptionally high diffusivity and unique reaction kinetics, research specifically addressing how magnetic fields affect hydrogen-premixed counterflow flames is remarkably scarce. The specific knowledge gaps in this critical area include:

- A notable scarcity of dedicated studies on magnetically controlled hydrogen premixed counterflow flames, despite the extensive research conducted on hydrocarbon-based and diffusion flames.
- A complete absence of investigations specifically focused on how magnetic fields influence flame stabilisation in hydrogen counterflow configurations, particularly under varying strain conditions.
- A lack of research exploring the changes in hydrogen combustion dynamics when subjected to magnetic field effects in counterflow systems, despite its direct relevance to high-performance combustion applications.

These identified gaps underscore the urgent need for further research into hydrogen-premixed counterflow flames under magnetic influence. Such investigations could yield profound insights into unique flame stability mechanisms and potential stabilisation strategies specifically tailored for hydrogen combustion. The present study directly addresses this critical gap by meticulously analysing the effects of magnetic field gradients on hydrogen counterflow flames, with a specific focus on investigating their impact on OH radical redistribution and overall flame stability.

3.4.2. Thermo-Diffusive Instabilities

Most existing research on magnetically controlled combustion has primarily concentrated on hydrodynamic instabilities, such as Darrieus-Landau instabilities, with only limited studies addressing modifications to diffusion-driven instabilities [18], [19], [46]. Given that hydrogen flames exhibit pronounced low Lewis number effects ($Le < 1$), their instability behaviour is fundamentally different from that of hydrocarbon flames. Yet, research on how magnetic fields influence these preferential diffusion-driven instabilities remains largely absent. The specific knowledge gaps in this area include:

- A limited number of studies on the effect of magnetic fields on diffusion-driven instabilities, as the majority of research has focused on hydrodynamic instability mechanisms like Darrieus-Landau instabilities.
- A lack of detailed analysis concerning how magnetic fields influence preferential diffusion mechanisms in hydrogen flames ($Le < 1$), despite the critical role of radical transport in determining flame stability.
- The absence of experimental studies extending hydrogen counterflow flame stability research to magnetically influenced systems, leaving a significant unexplored area in magnetic stabilisation techniques.

These knowledge gaps highlight the imperative need to investigate how magnetic fields influence thermo-diffusive instabilities in hydrogen counterflow flames, particularly focusing on the redistribution of OH radicals as a viable stabilisation mechanism. The present study attempts to utilise magnetic control strategies to redistribute combustion radicals with the aim of evaluating their effects on the intrinsic thermo-diffusive instability parameters.

3.4.3. Parametric Study

Most studies on magnetic flame control have primarily focused on the influence of magnetic field intensity, with comparatively limited research dedicated to the effects of field directionality, such as axial, radial, or perpendicular gradients [47], [52]. While magnetic field intensity has been demonstrably shown to influence flame shape, radical transport, and stabilisation, the specific impact of various magnetic gradient configurations on radical redistribution remains largely unexplored. Furthermore, no systematic parametric study has been conducted to comprehensively analyse how different magnetic field orientations affect OH radical transport across a wide range of varying strain rate conditions or equivalence ratios.[20], [50].

These identified gaps underscore the critical need for controlled parametric studies on magnetic field gradients to precisely determine optimal configurations for radical transport and enhanced flame stabilisation. The present study directly addresses this by introducing magnetic field gradient orientations both along and across flame surface and analysing their effects for varying applied strain and equivalence ratios.

3.4.4. High-Fidelity Computational Models

The numerical modelling of magnetically controlled flames remains a significantly underdeveloped area, particularly within the context of hydrogen combustion. While computational fluid dynamics (CFD) models have been widely employed for studying various aspects of combustion physics, existing simulations typically do not adequately account for magnetic forces acting on species transport and reaction kinetics, thereby limiting their predictive capability [18], [20] Despite the existence of theoretical frameworks that strongly suggest the applicability of magnetohydrodynamics (MHD) in combustion modeling, there is a notable absence of coupled MHD-combustion models specifically developed for hydrogen counterflow flames [12, 13]. The key gaps in the development of high-fidelity computational modelling in this domain are:

- A distinct lack of CFD models that effectively integrate magnetic field effects on species transport, leading to limited predictive accuracy in simulations of magnetically controlled combustion.
- The absence of existing MHD-based combustion models specifically tailored for hydrogen counterflow flames, despite hydrogen's distinct thermo-diffusive behaviour and its significant potential for magnetic interaction
- The unexplored potential of gravity-magnetic interaction principles, which have been successfully applied in other physical modelling frameworks but have yet to be fully incorporated into MHD-based CFD simulations for comprehensive combustion research [56].

These identified gaps highlight the urgent need for the development of advanced computational frameworks that can effectively incorporate MHD effects into CFD modelling. Such frameworks would allow for a more accurate and comprehensive representation of magnetic influence on radical transport and overall flame stability.

3.5. Summary

The application of magnetic fields in combustion research has been extensively explored, with numerous studies demonstrating their profound influence on radical transport, flame structure, stabilisation mechanisms, and pollutant formation. Significant progress has been achieved in understanding paramagnetic oxygen interactions in both hydrocarbon and diffusion flames, leading to notable advancements in the magnetic control of combustion velocity, flame anchoring, and NO_x emissions reduction [17], [19], [51]. These studies have provided invaluable insights into the role of magnetic fields in combustion control, particularly in co-flow and diffusion flame configurations, where the alignment of oxygen molecules has been shown to significantly influence stabilisation mechanisms [20], [50].

Despite these considerable advancements, several critical knowledge gaps remain unaddressed. Hydrogen premixed counterflow flames, which are highly sensitive to thermo-diffusive instabilities due to their inherently low Lewis number ($Le < 1$), have not been thoroughly investigated under magnetic influence [18], [46]. Additionally, comprehensive parametric studies on magnetic field gradients and directional effects remain limited, with the majority of research focusing on magnetic field intensity rather than the more nuanced gradient-induced radical transport modifications [47], [52]. Furthermore, while computational models have been developed for analysing magnetic combustion control, there is a distinct absence of dedicated numerical studies on the application of magnetic fields for OH radical redistribution, specifically in hydrogen counterflow flames[18], [20].

Addressing these critical gaps is paramount for advancing magnetic control strategies for flame stabilisation, particularly in strained hydrogen flames, where the precise redistribution of OH radicals can play a pivotal role in extending stability limits. Table 3.2 provides a concise summary of key research areas and their associated gaps, offering a clear perspective on the current state of existing studies.

Research Focus	**Flame Type**	**Magnetic Effects**	**Key Findings**	**Identified Gaps**
Hydrocarbon Flames	CH_4, LPG, Gasoline	Flame speed, shape, NOx control	Magnetic fields influence flame velocity and emissions reduction	Limited hydrogen-specific studies, limited analysis of preferential diffusion effects
Diffusion Flames	Co-flow flames	Oxygen transport, flame anchoring	Magnetic gradients modify oxygen distribution and flame stability	Very limited studies on counterflow flames, particularly premixed flames.
Hydrogen Flames	Co-flow diffusion flames	Limited radical transport analysis	Primary magnetic control strategy through oxygen convection	No magnetic control study in strained premixed hydrogen flames.
Parametric Studies	Various	Magnetic field intensity effects	Higher intensities affect flame shape and radical transport	No systematic study on gradient orientation, missing analysis of strain rate variations
Computational Models	CFD-based combustion simulations	Magnetic influence on radical transport	Some studies on field effects, but no targeted OH transport control	No numerical models implementing MHD effects with combustion dynamics

Table 3.2: Literature Review Summary

4

Methodology

This chapter outlines the computational approach and simulation setup used to investigate the effects of magnetic fields on thermo-diffusive instability in hydrogen combustion. The methodology focuses on the development of a numerical framework capable of simulating laminar counterflow flames under varying strain rates and magnetic field conditions. The simulation setup includes detailed descriptions of the geometry, boundary conditions, and operating conditions for the test cases. Furthermore, the chapter highlights the steps taken to modify the solver for the inclusion of magnetic field effects, ensuring it meets the specific requirements of this study. The following sections describe the solver setup, simulation execution, and the analysis framework used to interpret the results of the simulations.

4.1. Simulation Setup

This section outlines the computational setup used to simulate the flame dynamics in the study. It details the geometry, boundary conditions, and operating conditions employed to investigate thermo-diffusive instability in hydrogen flames. Additionally, the section describes the solver specifications and the test matrix used for the simulations. By establishing the simulation environment, we can better understand the factors influencing flame behaviour, particularly how strain, Lewis number variations, and magnetic field effects contribute to instability and flame speed. The choices made for these setups are explained in the context of the study's objectives to provide a solid foundation for the analysis and results that follow.

4.1.1. Geometry Description

The computational domain employed in this study is based on a 2D axisymmetric wedge geometry with a half-angle of 2.5°, representing a segment of a cylindrical counterflow flame configuration. The domain has an axial length of 0.01 m and a radial extent of 0.005 m, forming a thin wedge that is sufficient to resolve the flame structure without introducing azimuthal variations. The setup is well-suited to study flame stabilisation and thermo-diffusive instability in a counterflow configuration.

A visualisation of the domain is shown in Figure 4.1. The red patch corresponds to the reactant inlet, where a premixed hydrogen-air mixture is introduced axially. The green patch is the exhaust inlet at $x = 0.01$ m, where the hot products enter the domain axially. The blue patch denotes the radial outlet, where the flow exits the domain. The grey surface represents the azimuthal symmetry plane having a wedge-type patch. The domain is assumed to be axisymmetric, and the symmetry axis is treated with an empty boundary condition.

The computational grid consists of 448 × 224 × 1 hexahedral cells with uniform spacing, suitable for axisymmetric simulation in OpenFOAM. Mesh refinement details and convergence behaviour are discussed in a later section.

4.1.2. Boundary Conditions

In this study, the boundary conditions for temperature, species composition, and velocity are defined for various boundary patches in the computational domain. These patches represent different parts of the system, such as the reactant inlet, exhaust inlet, and outlet, as well as symmetry boundaries for the axis, front, and back. The boundary conditions ensure accurate representation of flow and thermal dynamics in the counterflow configuration.

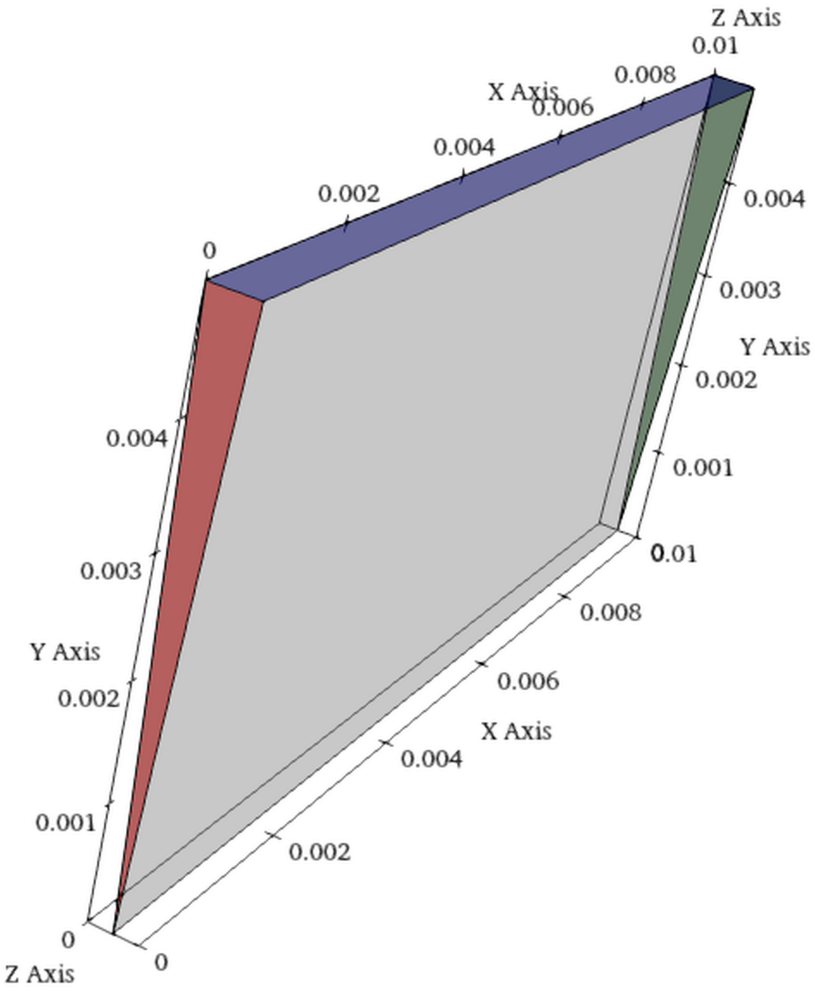

Figure 4.1: Computational domain used for simulating the counterflow premixed hydrogen flame. The red patch is the reactant inlet, the green patch is the hot product inlet, the blue patch is the outlet, and the grey faces represent the azimuthal symmetry planes.

The following is an overview of the boundary types used for each variable:

- **reactantInlet_pos:** This boundary defines the inlet for the premixed reactants.
- **exhaustInlet_neg:** This boundary represents the inlet for the combustion products.
- **outlet:** This boundary simulates the radial outflow from the domain.
- **axis:** The axis boundary condition is set as empty, meaning no physical flow or variable change occurs along the symmetry axis.
- **front and back:** These boundaries define the front and back of the computational domain, with wedge conditions applied to maintain axisymmetry.

Table 4.1 summarises the boundary types for each variable at the respective patches. It details the type of boundary condition applied (e.g., fixedValue, inletOutlet, zeroGradient, etc.) used at the inlets and outlet. The boundary type for the **front** and **back** is set to a wedge-type, and the **axis** is set to empty for all the variables.

Variable	reactantInlet_pos	exhaustInlet_neg	outlet
Temperature (T)	fixedValue	fixedValue	zeroGradient
Hydrogen (H_2)	fixedValue	fixedValue	inletOutlet
Oxygen (O_2)	fixedValue	fixedValue	inletOutlet
Nitrogen (N_2)	fixedValue	fixedValue	inletOutlet
Water Vapour (H_2O)	fixedValue	fixedValue	inletOutlet
Pressure (p)	fixedValue	fixedValue	inletOutlet
Velocity (U)	fixedValue	fixedValue	pressureInletOutletVelocity

Table 4.1: Boundary patch types for each variable.

The values of each variable at the boundaries vary with changes in the equivalence ratio (ϕ) and the applied strain rate. As the strain rate and equivalence ratio change, the velocity values at the inlets and exhaust, as well as the species mass fractions and temperature at the inlets, will be adjusted accordingly. Table 4.2 and Table 4.3 provide specific values for these variables under different strain rates and equivalence ratios, respectively. The detailed boundary conditions for equivalence ratio $\phi = 0.4$ and the applied strain $a = 1000s^{-1}$ are provided in Appendix B to give a full picture of the applied conditions. These values ensure that the simulations account for the variations in flow conditions as they relate to the changes in mixture strength and imposed strain, which ultimately affect the flame dynamics.

Applied Strain Rate (s^{-1})	Reactant Inlet Velocity (m/s)	Exhaust Inlet Velocity (m/s)
1000	5	-5
1500	7	-8
2000	10	-10

Table 4.2: Velocity values at reactant and exhaust inlets for different strain rates.

Variable	$\phi = 0.4$			$\phi = 0.8$		
	Reactant Inlet	**Exhaust Inlet**	**Outlet**	**Reactant Inlet**	**Exhaust Inlet**	**Outlet**
H_2	0.0115	0	0	0.0228	0	0
O_2	0.2304	0.1383	0	0.2278	0.0454	0
H_2O	0	0.1037	0	0	0.2052	0
N_2	0.7581	0.758	0	0.7494	0.7494	0
T (K)	292	1425	292	292	2205	292

Table 4.3: Species mass fractions and temperature at the boundaries for $\phi = 0.4$ and $\phi = 0.8$.

The boundary conditions for pressure are defined using a `zeroGradient` condition at both the inlet boundaries `reactantInlet_pos` and `exhaustInlet_neg`, indicating that there is no gradient in pressure at the inlets. For the `outlet` boundary, a `totalPressure` boundary condition is applied, where the `internalField` value of pressure (101325 Pa) is used to maintain a constant total pressure across the domain. This reflects the assumption of low Mach number flow, where pressure variations are minimal and do not significantly affect the flow dynamics. While pressure does change inside the domain, the changes are discontinuous and do not influence the results directly, as the pressure field serves more as a Lagrange multiplier to satisfy the velocity field. Given the nature of the flow and the fact that pressure is not a primary variable of interest in this study, the exact values of pressure are less critical for the analysis of flame stability and thermodiffusive effects.

4.1.3. Lewis Number Cases

In this study, two distinct Lewis Number (Le) cases are considered: the unity Lewis number case ($Le = 1$) and the non-unity Lewis number case ($Le < 1$), specifically for hydrogen-air mixtures.

- $Le = 1$ **(Benchmark Case):** The unity Lewis number case assumes equal diffusivities for thermal and mass transport. This case was used primarily to identify and assess the effects of various magnetic field configurations on the flame, which helped in selecting the most relevant configurations and test cases for further analysis.
- $Le < 1$ **(Hydrogen-Air Mixtures):** For hydrogen-air mixtures, where $Le < 1$, hydrogen diffuses faster than heat, leading to preferential diffusion. Under strained conditions, this creates a fuel-enriched reaction zone that accelerates combustion. These cases are the focus of the detailed analysis in this study.

The choice of these cases enables a comparative understanding of flame dynamics, with $Le = 1$ serving as a baseline for identifying the most impactful field configurations, and $Le < 1$ providing insight into how preferential diffusion contributes to instability and flame behaviour under varying strain rates and magnetic fields.

4.1.4. Solver Specifications

This subsection outlines the key specifications of the solver used for simulating the counterflow flame dynamics, including the transport models, combustion models, thermodynamic assumptions, diffusion models, and the incorporation of magnetic fields. For further details on the **fvSchemes** and **fvSolutions**, please refer to Appendix A.

Transport Model

The transport model in this study consists of three primary components: momentum transport, species transport, and energy transport, each handled as follows:

- **Momentum Transport:** The flow is assumed to be laminar, and the momentum equation is solved using the Navier-Stokes equations for incompressible flow. The dynamic viscosity (μ) is computed using a log-polynomial model with a degree-3 polynomial, where the viscosity varies with temperature. This approach ensures that the transport of momentum in the laminar flow is accurately captured.
- **Species Transport:** The transport of species is described using the Fickian transport model, where the diffusion of each species is driven by concentration gradients. The solver employs mixture-averaged diffusivities, which are computed using the binary diffusion coefficients and the log-polynomial model, as explained in a later section. This model accounts for the interactions between species and their diffusion in the mixture.
- **Energy Transport:** The energy equation is solved using the sensible enthalpy method. The thermal diffusivity (κ) follows a log-polynomial model with a degree-3 polynomial, describing the conductive heat diffusion. The species interdiffusion is handled separately through the species transport model, ensuring that both thermal and species diffusivities are accurately represented in the energy equation.

These transport models are used to solve the governing equations for momentum, species, and energy, capturing the complex flame dynamics in non-unity Lewis number cases.

Combustion Model

The combustion is assumed to be laminar, where the flame structure is steady and symmetric. The reaction rates are governed by the San Diego mechanism for hydrogen combustion, which models the chemical kinetics involved. This approach is suitable for low-Mach, steady-state flames where turbulence effects are not significant.

Chemistry Model

The chemistry model used in this study is based on the San Diego mechanism, which is a detailed chemical reaction model for hydrogen combustion. This model includes 21 reactions and 9 species detailed in Chapter 2.

The solver for the chemical kinetics is based on an ODE (Ordinary Differential Equation) solver, with the specific solver chosen as seulex, which is used to solve the differential equations governing the species concentrations. The solver is configured with an absolute tolerance of 1e-12 and a relative tolerance of 0.1 to ensure precision in the integration of the chemical reactions over time.

In terms of reaction handling, differential diffusion is enabled, while thermal diffusion is turned off. This allows the solver to account for the preferential diffusion of species based on their diffusivity, which is particularly important for understanding the thermo-diffusive instability in lean hydrogen flames. The chemistry model includes the following key properties and settings:

- **EulerImplicitCoeffs:** Used for implicit time-stepping, with a time step for chemical reactions set to 1e-10 seconds.

- **odeCoeffs:** The `seulex` solver is used to solve the ODEs, with strict tolerances for accuracy in the calculation of reaction rates and species concentrations.
- **Prandtl and Schmidt Numbers (Prt and Sct):** These are set to 0.7, typical for air-like mixtures, and control the thermal and species diffusivity in the flow.

Thermodynamic Model
The thermodynamic model used in this study assumes ideal gas behaviour for all species involved in the combustion process. This simplifies the calculation of thermodynamic properties such as enthalpy and specific heat, which are crucial for solving the energy equation.

- **Ideal Gas Law:** The ideal gas law is applied to all species, which relates pressure, volume, temperature, and the number of moles of each species. This assumption is valid for the temperature and pressure ranges typical in combustion simulations.
- **JANAF Polynomial:** The thermodynamic properties of each species, such as specific heat capacity (C_p) and the specific heat ratio (γ), are computed using the JANAF polynomial. The JANAF polynomial provides a temperature-dependent formula for calculating these properties, which is particularly useful for high-temperature combustion processes. The polynomial fits the experimental data for specific heats and enthalpies over a wide range of temperatures.

  The standard JANAF polynomial is used to compute the specific heat (C_p) of each species, based on the temperature dependence:

$$C_p = a + b\log(T) + c\log(T)^2 + d\log(T)^3 + e\log(T)^4$$

  where a, b, c, d, and e are constants specific to each species.
- **Sensible Enthalpy:** The energy equation is solved using sensible enthalpy (h), which represents the internal energy of the system. The change in sensible enthalpy is used to compute the temperature changes in the system, taking into account the heat released from chemical reactions and the heat transported through the flame front.

This thermodynamic model enables the simulation of realistic combustion processes by accurately modelling the energy transport and species-specific temperature-dependent properties.

Mixture Model
In this study, the species diffusion is modelled using the multi-component mixture model, which accounts for the interactions between species in the mixture. The diffusion coefficients are calculated using the binary diffusion coefficients (D_{ij}), which represent the diffusion between each pair of species.

- **Binary Diffusion Coefficients (D_{ij}):** The binary diffusion coefficients are computed using the log polynomial model, which depends on temperature, and the coefficients are defined for each pair of species. These coefficients are essential for accurately modelling the species transport in the domain.
- **Mixture-Averaged Diffusion Coefficient (D_m):** The mixture-averaged diffusion coefficient for each species in the mixture is calculated using the following formula:

$$D_{m_i} = \frac{1 - Y_i}{m_i \sum_{j \neq i} Y_j / m_j D_{ij}}$$

  where m_i is the molecular mass and Y_i is the mass fraction of the species i.

This model accurately accounts for the inter-species diffusion and provides a robust framework for simulating multi-component mixtures in combustion, particularly for studying the effects of preferential diffusion in $Le < 1$ flames.

Magnetic Field Implementation
The magnetic field effects are incorporated into the solver through a spatially varying magnetic field, defined in the magneticProperties file. This file specifies the magnetic field configurations and how they interact with species in the mixture.

- **Field Configuration:** The magnetic field is defined as $B(x) = B_0 \cdot \exp(-k(x - r_0))$ for $r_0 \leq x \leq r_f$, where:

  - B_0 is the magnetic field strength at r_0,
  - k is the decay constant (in m^{-1}),
  - r_0 and r_f are the spatial boundaries defining the region over which the magnetic field is applied.
  - The field decays exponentially along the direction specified by `gradDir`. The inv parameter allows for the reversal of the decay direction, meaning the decay can either proceed from r_0 to r_f (default) or from r_f to r_0 if `inv` $= 1$.

- **Spin Value and Susceptibility:** Each species has a defined spin value (S_i), which influences its interaction with the magnetic field. The species' magnetic susceptibility (χ_i) is calculated using the spin value and is used to adjust their diffusion properties under the magnetic field. The susceptibility is calculated using Equation 3.2.
- **Magnetic Properties File:**
  - `nFields`: Number of magnetic field configurations.
  - `field1`/`field2`: Defines magnetic field properties, including type, gradient direction, and decay coefficients.
  - `gradDir`: Direction of the magnetic field gradient (axial or radial).
  - `r0`, `rf`: Defines the spatial range over which the field applies.
  - `inv`: Inverts the direction of decay if set to 1.
  - `expCoeff`, `linCoeff`: Defines B_0 and k for exponential or linear decay of the magnetic field.
  - `speciesProperties:` Defines the species' spin values and molecular weights, which determine their response to the magnetic field.

These magnetic fields influence species through the Kelvin force and magnetic diffusion corrections, which are included in the species transport equations. A correction term ensures that species fluxes remain consistent with mass conservation when magnetic fields affect species diffusion.

For further details on the equations and solver modifications, refer to Chapter 3.

Solver Settings and Configurations

The solver is configured with advanced numerical methods for accuracy and efficiency:

- `fvSchemes`: Utilises fourth-order gradient schemes, cubic interpolation, and Gauss cubic schemes for divergence to ensure high accuracy in the solution.
- `fvSolutions`: The pressure field is solved using PCG (Preconditioned Conjugate Gradient) with the GAMG preconditioner, while the velocity and species fields are solved using smoothSolver with Gauss-Seidel smoothing.
- PIMPLE Algorithm: For transient simulations, the solver uses the PIMPLE algorithm (a combination of PISO and SIMPLE), which employs three correctors and an outer corrector to ensure the solution converges.

The detailed configuration of these settings in the `fvSchemes` and `fvSolutions` files is shown in Appendix A.

4.1.5. Test Matrix

The test matrix is designed to investigate the impact of magnetic field configurations, strain rates, and operating conditions on flame stability and diffusion, particularly for conditions with $Le = 1$ and $Le < 1$. Below is an overview of the test matrix setup, along with justifications for the choices made for each operating condition:

Magnetic Field Configurations

To examine how externally imposed magnetic fields influence the flow and flame structure, four idealised configurations were prescribed over the counterflow domain ($x \in [0, 0.01]$ m, $y \in [0, 0.005]$ m). The configurations differ by orientation (axial vs. radial) and spatial variation (exponential decay, inverse exponential, and localised Gaussian). For all cases, the characteristic decay coefficient is set to $k = 120\ \mathrm{m}^{-1}$, and the reference strength is varied as $B_0 \in 0, 0.5, 1.0, 1.5, 2.0$ T. The four configurations are summarised in Figure 4.2, with each panel referenced below.

Axially Decaying Exponential Field (Figure 4.2a)

The axial field decreases monotonically from the left boundary according to

$$B_x(x) = B_0 \exp(-kx),$$

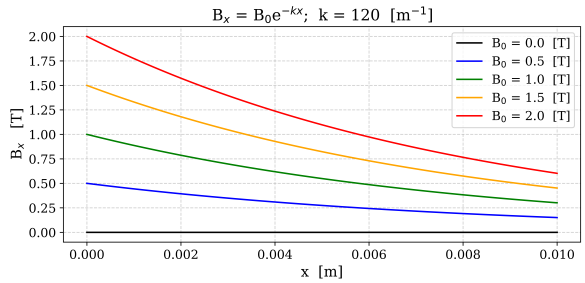

(a) Axially decaying field $B_x = B_0 \exp(-kx)$ with $k = 120\ \mathrm{m}^{-1}$ and $B_0 \in 0, 0.5, 1.0, 1.5, 2.0$ T.

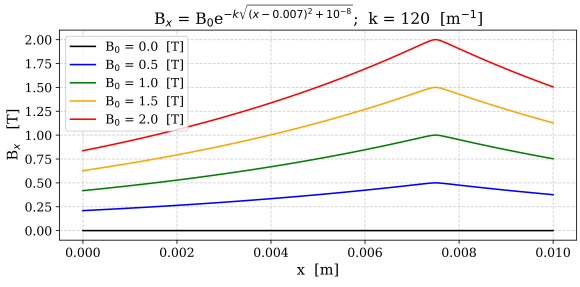

(b) Axial Gaussian field $B_x = B_0 \exp\big(-k\sqrt{(x-r_0)^2+\varepsilon^2}\big)$ with $r_0 = 0.0075$ m and $k = 120\ \mathrm{m}^{-1}$.

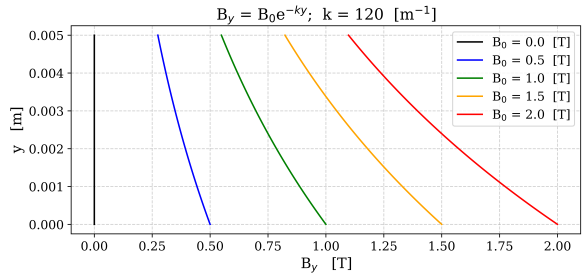

(c) Radially decaying field $B_y = B_0 \exp(-ky)$ with $k = 120\mathrm{m}^{-1}$. Core-peaked forcing that weakens towards $y = 0.005$ m.

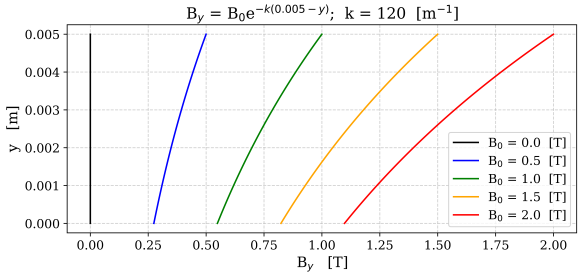

(d) Radially increasing field $B_y = B_0 \exp!\big(-k(y_0 - y)\big)$ with $y_0 = 0.005$ m and $k = 120\ \mathrm{m}^{-1}$.

Figure 4.2: Magnetic field configurations used in this study. Panels (a)–(d) correspond to the analytic forms. All fields are imposed over $x \in [0, 0.01]$ m and $y \in [0, 0.005]$ m; the reference strength B_0 is varied as listed in the captions.

which yields the strongest forcing near $x = 0$ and a progressive attenuation towards the stagnation region and outlet. This profile provides a simple benchmark for axial forcing with a single spatial scale.

Axial Gaussian Field (Figure 4.2b) A localised axial field is imposed via

$$B_x(x) = B_0 \exp\Big(-k\sqrt{(x-r_0)^2+\varepsilon^2}\Big),$$

centred at $r_0 = 0.0075$ m, with a small ε used only to regularise the peak. This concentrates magnetic forcing over a finite axial extent, enabling assessment of spatially confined perturbations to the flow and reaction zone.

Radially Decaying Exponential Field (Figure 4.2c)
Here, the field is oriented radially and strongest on the axis:

$$B_y(y) = B_0 \exp(-ky),$$

so that forcing diminishes towards the outer radius. This configuration preferentially influences the core region of the counterflow.

Radially Increasing (Inverse Exponential) Field (Figure 4.2d)
An opposing radial distribution is obtained from

$$B_y(y) = B_0 \exp\big(-k(y_0 - y)\big), \qquad y_0 = 0.005\ \mathrm{m},$$

which peaks near the outer boundary and weakens towards the axis. This edge□enhanced profile probes how peripheral forcing redistributes momentum and species transport.

Strain Rate Variations
Strain rates are varied at 1000, 1500, and 2000 s^{-1} to examine the effects of different stretching conditions on flame stability. The selected strain rates are justified as follows:

- **1000 $\mathbf{s}^{-1}$:** This value represents a typical strain rate found in many combustion systems, serving as a baseline for flame stability analysis under moderate strain conditions.

- **1500 and 2000 s^{-1}:** These higher strain rates are chosen to simulate more extreme flame stretching scenarios. Such conditions are anticipated to introduce significant levels of instability, particularly when magnetic fields influence species diffusion and flame dynamics. Higher strain rates typically increase the sensitivity of the flame to magnetic field effects.

Operating Conditions
Equivalence ratios of ϕ = 0.4 and ϕ = 0.8 are selected to investigate the influence of different fuel-air mixtures on flame stability and dynamics:

- **ϕ = 0.4:** Represents a lean mixture, which is particularly significant for studying thermo-diffusive instabilities. These instabilities are more pronounced under lean conditions, making them ideal for exploring the interaction between magnetic fields and flame dynamics in such regimes.
- **ϕ = 0.8:** Represents a richer mixture, providing a contrast to the lean case. This ratio is chosen to investigate whether the sign of the Markstein Length L_b influences magnetic control, as L_b changes sign at $\phi = 0.7$ for premixed hydrogen flames.

Magnetic Field Strengths
For $Le = 1$, magnetic field strengths range from $B_0 = 0 - 2$ T. The upper limit of 2 T is selected based on the following considerations:

- Magnetic field strengths above 2 T are generally non-realisable in practical combustion systems, as they result in expensive systems with high power consumption and massive weight.
- According to Mizutani et al. [46], reaction kinetics are not significantly influenced by magnetic fields below 5 T, making 2 T an adequate strength to capture the effects of Kelvin forces without the interference of magnetically modified reaction kinetics.
- The chosen range of 0 to 2 T is both realistic and sufficiently varied to explore the influence of magnetic fields on species diffusion and flame structure, while remaining within the domain of Kelvin forces.

4.2. Preliminary Tests

Before conducting the main simulations, a mesh convergence study was performed to ensure that the flame was adequately resolved while maintaining computational feasibility. The guiding principle was to capture the thermal flame structure with at least ten computational cells across the flame thickness, which is considered the minimum requirement for a flame-resolved simulation [57].

4.2.1. Mesh Resolution and Flame Thickness

The first step was to evaluate how the estimated thermal flame thickness and the number of grid points within the flame region varied with mesh refinement. Figure 4.3 shows the results of this investigation.

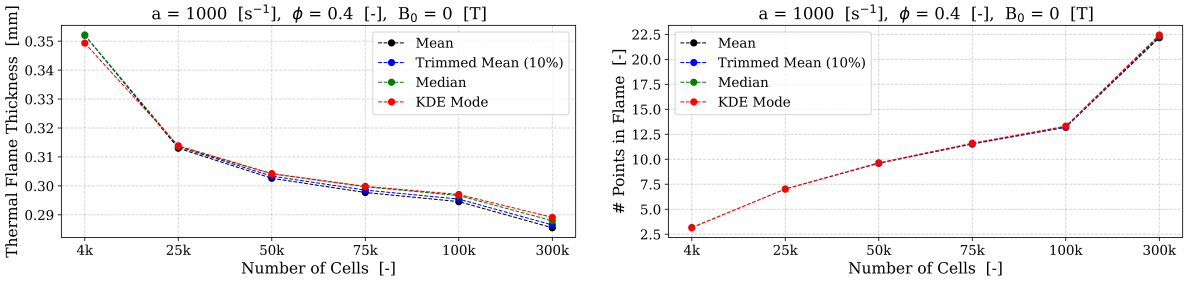

(a) Thermal Flame Thickness variation with mesh resolution.

(b) Number of Points within the flame.

Figure 4.3: Variation of flame thickness and grid resolution. With mesh refinement, the estimated flame thickness decreases while the number of cells across the flame region increases.

The results demonstrate two opposing trends:

- The estimated flame thickness decreases as the mesh is refined.
- At the same time, the number of computational cells across the flame region increases, thereby improving spatial resolution.

From Figure 4.3, it is evident that meshes with more than 75k cells satisfy the minimum requirement of ten points across the flame. Thus, 75k cells represent the threshold for flame-resolved simulations. However, refining beyond this introduces significant computational challenges, which are discussed below.

4.2.2. Convergence and Computational Cost

To verify that the solutions converged satisfactorily, the residual histories of enthalpy were monitored for different meshes. At all resolutions, the residuals flattened out, confirming convergence. However, the computational cost increased drastically with refinement, as shown in Figure 4.4. The following points highlight the key findings:

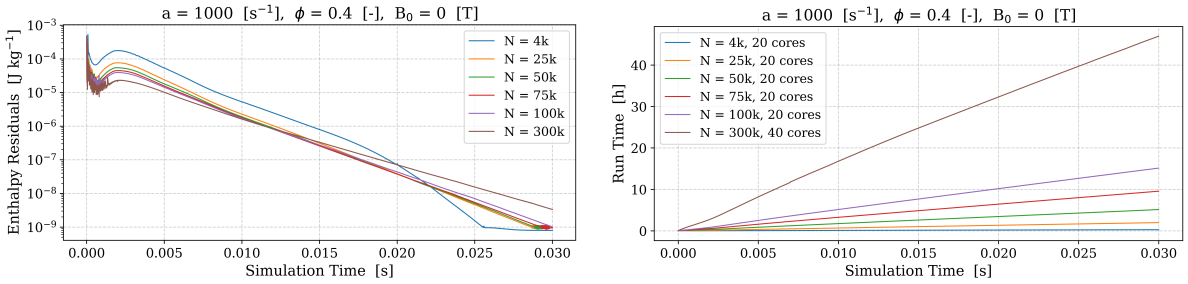

(a) Residuals of enthalpy for different mesh resolutions.

(b) Wall-time required for different mesh resolutions.

Figure 4.4: Convergence behaviour and computational cost for various mesh resolutions.

- At a mesh size of 0.3 million cells, simulating just 0.03 s of physical time required almost 2 days on 40 cores.
- With 96 cores (the maximum allowed on the HPC12 cluster), the runtime reduced to about 23 hours per simulation for 0.03 s.
- However, reaching steady state required at least 40 ms of physical time, which equates to approximately 1.5 days even with 96 cores.
- For the test matrix consisting of at least 16 primary simulations (two strain rates $\times$ two equivalence ratios $\times$ two magnetic field strengths $\times$ two configurations), the minimum total computational cost would amount to about 16 days for one complete sweep.
- For higher strain rates and higher equivalence ratios, the time required to reach steady state extended to 50 ms or more, demanding up to two days of runtime per case.

4.2.3. Effect of Mesh Resolution on Flame Structure

The influence of mesh refinement on the flame shape was also assessed by comparing the isocontours of the progress variable C at coarse and fine resolutions, shown in Figure 4.5.
The results reveal that:

- Near the axis, the flame structure is relatively insensitive to mesh refinement.
- Near the radial outlet, however, the flame shape changes substantially with increasing resolution. These differences alter curvature estimates, which are particularly sensitive to the flame periphery.

This indicates that while coarse meshes may underpredict certain structural features (e.g., curvature at the periphery), the central flame zone remains robust. Given that this study is aimed at understanding dominant mechanisms and qualitative trends, this level of accuracy is acceptable.

4.2.4. Final Choice of Mesh

Balancing physical accuracy against computational feasibility, a mesh resolution of 0.1 million cells was selected for all subsequent simulations. This resolution was chosen based on the following considerations:

- It satisfies the minimum requirement of ten cells across the flame.
- Each run requires approximately 8 hours on 96 cores, providing a practical turnaround time.
- The reduced runtime allows sufficient buffer to rerun simulations in case of solver modifications or setup adjustments.
- Residual flattening confirmed convergence, ensuring the reliability of the results.

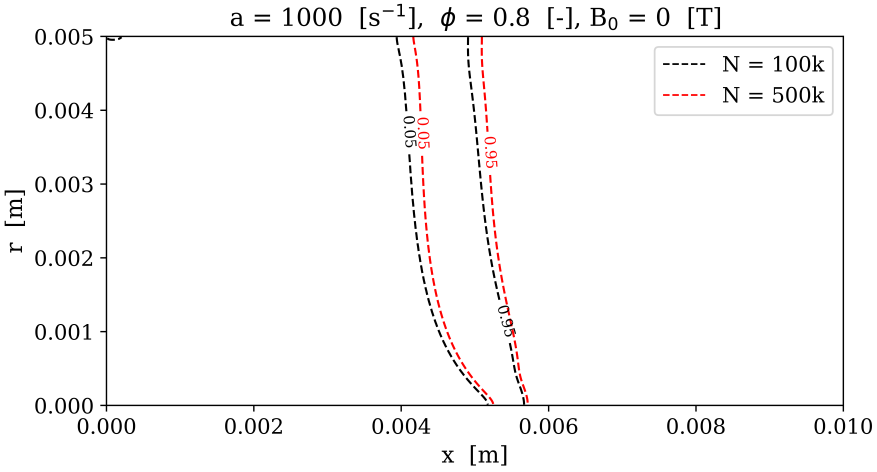

Figure 4.5: Isocontours of the progress variable C at values 0.05 and 0.95 for $N = 100$k and $N = 500$k. The flame shape changes significantly near the outlet, while differences near the axis remain small.

Mesh size (cells)	Cells across flame	Time for 0.03 s on 96 cores	Notes
75k	$\geq$10	$\sim$2.5 h	Meets minimum requirement
100k	12–14	$\sim$8 h	Chosen baseline resolution
300k	$>$20	$\sim$23 h	$\sim$1.5 days to steady state
500k	$>$30	$>$2 days	Significant detail, but prohibitive

Table 4.4: Summary of mesh convergence study.

The trade-offs between mesh size, accuracy, and computational cost are summarised in Table 4.4.

In summary, although finer meshes provide more detail in the flame periphery, the increase in computational cost was prohibitive for the scope of this study. A compromise resolution of 0.1 million cells was therefore adopted, enabling a sufficiently resolved flame while keeping the simulations manageable within the allocated computational resources.

4.3. Analysis Framework

This section outlines the methodology adopted for analysing the simulation results, including the parameters evaluated, their extraction or derivation procedures, and the rationale for the selected analytical approaches. The analysis employs a custom Python-based framework built around the `foamcase.py` and `simAnalysis.py` modules, with `pyvista` utilised for data processing and visualisation.

4.3.1. Global Flame Parameters

The global flame parameters considered in this work are:

1. Thermal Flame Thickness
2. Flame position relative to the flow field
3. Flame Displacement Speed

The definitions and computational procedures for each are provided below.

Flame Thickness

The thermal flame thickness is calculated according to Equation 2.47. While this definition is appropriate for one-dimensional flames, where the flame normal direction coincides with the computational grid [58], it becomes less representative for curved, two-dimensional flames. In such cases, the flame thickness varies spatially due to local curvature and strain effects, making a single global value based on domain-wide extrema of T unsuitable.

Instead, a statistical approach is adopted, computing local flame thicknesses along normals to the flame surface and determining a measure of central tendency [59].

The flame normals are shown in Figure 4.6 together with iso-contours of the progress variable C at values 0.05, 0.5, and 0.95.

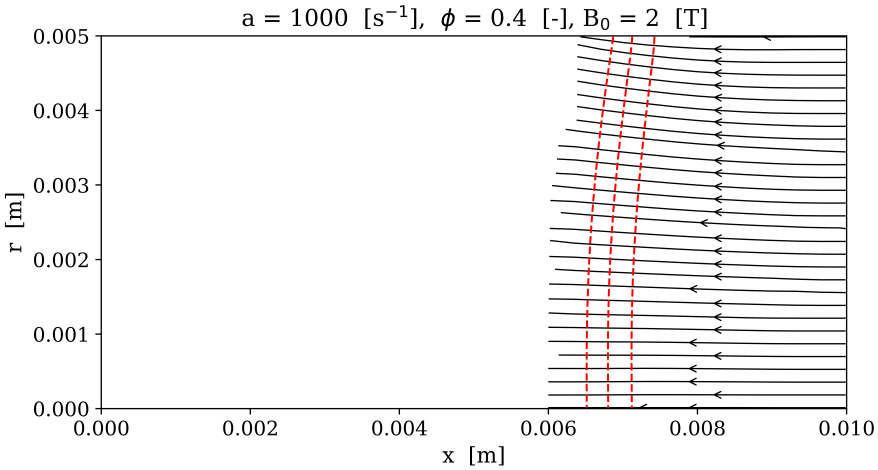

Figure 4.6: Flame normals pointing from the burnt gas to the unburnt gas, overlaid with iso-contours of the progress variable (red-dashed lines) with $C = 0.05, 0.5, 0.95$.

The temperature field is sampled along $n = 224$ normals (one per y-grid location), and δ_L is computed for each profile. The resulting distribution of flame thickness values is shown in Figure 4.7.

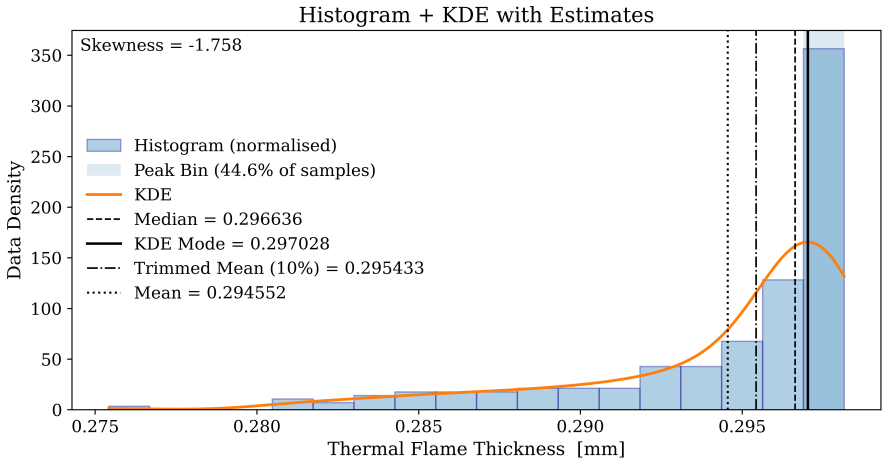

Figure 4.7: Histogram of thermal flame thickness values with measures of central tendency, for $a = 1000\ \mathrm{s}^{-1}$ and $\phi = 0.4$.

The distribution is notably skewed, rendering both the arithmetic mean and trimmed mean poor representatives of the dataset. Instead, the mode from a kernel density estimate (KDE) is adopted, as it aligns with the histogram bin containing 44% of all samples, thereby serving as a statistical representative of the thermal flame thickness.

Flame Displacement Speed

The flame displacement speed, also referred to as the flame propagation speed, is defined as the velocity at which the flame front advances perpendicular to its surface into the unburnt mixture. It quantifies the combined effects of chemical reactions and molecular transport processes at the flame front and serves as a key metric for assessing flame–flow interactions [14], [60]. In a general formulation, the displacement speed can be expressed as:

$$S_D = \frac{1}{|\nabla C|}\left(\frac{\partial C}{\partial t} + \vec{v}\cdot\nabla C\right) \tag{4.1}$$

where C is a scalar quantity used to define the flame surface, $\vec{v}$ is the flow velocity vector, and ∇C is the gradient of C normal to the flame surface. The choice of C is critical, as it directly influences the interpretation of S_D. Common options include isocontours of temperature or of species mass fractions that vary monotonically through the flame front [31].

In this study, the flame surface is identified using the progress variable C, defined in terms of the fuel mass fraction as:

$$C = 1 - \frac{Y_{H_2}}{Y_{H_2,u}} \tag{4.2}$$

where Y_{H_2} is the local mass fraction of hydrogen and $Y_{H_2,u}$ is the corresponding value in the unburnt mixture. This definition ensures that $C = 0$ in the unburnt region and $C = 1$ in the fully burnt gases, with intermediate values tracing the flame front. By substituting this definition into the hydrogen transport equation, the displacement speed can be reformulated as:

$$S_D = \frac{1}{\rho|\nabla C|}\left(- \underbrace{\frac{\dot{\omega}_{\mathrm{H_2}}}{Y_{H_2,u}}}_{\text{Kinetic Contribution}} + \underbrace{\frac{\nabla \cdot \vec{J}_{\mathrm{H_2}}}{Y_{H_2,u}}}_{\text{Diffusive Contribution}} \right) \tag{4.3}$$

where ρ is the density, $\dot{\omega}_{\mathrm{H_2}}$ is the chemical source term for hydrogen (negative in consumption), and $\vec{J}_{\mathrm{H_2}}$ is the total hydrogen diffusion flux. This decomposition separates the displacement speed into two physically distinct components:

- **Kinetic Contribution:** Arising from chemical reaction rates, dependent on local temperature, species concentrations, and chemical kinetics.
- **Diffusive Contribution:** Arising from molecular and thermal diffusion processes, influenced by local gradients, transport coefficients, and strain effects.

Such a decomposition is particularly valuable in analysing premixed flames subject to strain, curvature, or external field effects, as it allows identification of whether variations in S_D are driven primarily by changes in chemical kinetics or by transport-related mechanisms. For example, in strained hydrogen flames, high curvature or stretch rates can enhance diffusive transport, increasing S_D even when chemical kinetics remain unchanged [14], [15]. Conversely, kinetic contributions may dominate under conditions of altered temperature or radical concentrations, such as those induced by magnetic field manipulation of paramagnetic species.

This framework thus provides a way for investigating how flame dynamics respond to both intrinsic chemical processes and externally imposed flow or field conditions.

4.3.2. Instability Parameters

Thermo-diffusive instabilities are a defining characteristic of lean premixed hydrogen flames, particularly under low-Lewis-number conditions ($Le < 1$). These instabilities originate from the disparity between thermal and mass diffusivities, which results in preferential diffusion of the deficient reactant and non-uniform burning rates along the flame surface. In $Le < 1$ flames, small perturbations on the flame front may amplify over time, leading to cellular flame structures, enhanced burning in convex regions, and potential local extinction in concave regions [12], [14].

In the context of developing magnetic flame control strategies, the primary objective is to determine whether externally applied magnetic fields can mitigate the negative impacts of such instabilities while preserving, or even enhancing, flame stability. To assess this, it is necessary to quantify instability-related parameters that reflect both the geometric configuration of the flame and the associated transport phenomena. In this study, three principal metrics are evaluated:

1. **Flame Curvature:** Describing the local geometry of the flame front and its correlation with burning rate asymmetry.
2. **Kinematic Stretch Rate:** Capturing the combined effects of flame curvature and flow-induced strain.
3. **Markstein length:** Linking the flame's response to stretch rate with its intrinsic transport–chemistry coupling.

Together, these quantities provide a rigorous diagnostic framework for investigating how magnetic fields influence instability parameters in lean hydrogen combustion.

Flame Curvature
The local geometry of the flame front, whether convex or concave relative to the unburnt mixture, can be quantified through the divergence of the flame front normal vector, $\nabla \cdot \hat{n}$. In this work, the flame normals are defined to point from the burnt gases towards the unburnt mixture (Equation 2.49) using the progress variable C. A positive value of $\nabla \cdot \hat{n}$ indicates that the flame is convex towards the unburnt gases, whereas a negative value corresponds to a concave configuration.

This metric is particularly relevant for lean hydrogen flames with $Le < 1$, where curvature significantly influences local burning behaviour [14]. Convex regions experience intensified burning due to preferential diffusion of hydrogen towards the reaction zone, increasing the local flame speed. In contrast, concave regions suffer from reduced reactant replenishment, which can lead to diminished burning rates or even localised quenching [12], [14].

Flame curvature also directly contributes to flame surface stretch, with the curvature-induced stretch rate expressed as $S_D(\nabla \cdot \hat{n})$, where S_D is the flame displacement speed. This term, in combination with strain-induced stretch, determines the overall kinematic stretch rate experienced by the flame [32]. Accurate determination of $\nabla \cdot \hat{n}$ is therefore essential for subsequent evaluation of stretch rate and for diagnosing instability dynamics.

Kinematic Stretch Rate
The evaluation of the kinematic stretch rate is essential for characterising thermodiffusive instabilities, as it quantifies the local deformation of the flame front due to curvature and flow. As an instability parameter, the stretch rate allows for the assessment of how perturbations in the flame geometry influence local flame speeds, particularly in $Le < 1$ flames, where variations in curvature can amplify or suppress thermodiffusive effects. Accurate estimation of this parameter is therefore critical for understanding the onset and growth of intrinsic flame instabilities. The kinematic stretch rate is directly computed from the flow variables as per Equation 2.51, Equation 2.50 and Equation 4.3.

Note on S_D evaluation. In a steady flame and with sufficient spatial resolution, the kinematic form $S_D = -\vec{u} \cdot \hat{n}$ and the transport-based evaluation of S_D are mathematically equivalent when evaluated on the same C-isosurface. Discrepancies between the two can arise due to incomplete resolution of the reaction zone, numerical diffusion, or interpolation errors in gradient evaluation. In the present analysis, S_D obtained from the transport equation is used for consistency across diagnostics, with observed deviations from $-\vec{u} \cdot \hat{n}$ attributed to these numerical factors. Mesh refinement or higher-order reconstruction schemes can reduce such mismatches.

Markstein Length
The Markstein length L_b characterises the first-order sensitivity of flame propagation to stretch. Based on the flame speed used, there are two types of Markstein lengths: The displacement Markstein length L_b^d and the consumption Markstein length L_b^c [31]. In its displacement-based form, it is obtained from the approximate linear relation between flame displacement speed S_D and the kinematic stretch rate κ in the small-stretch regime:

$$S_D \approx S_L - L_b \kappa \tag{4.4}$$

where S_L is the unstretched laminar burning velocity. In one-dimensional, quasi-planar flames, this definition is unambiguous, since κ is uniform along the flame front. Under these conditions, L_b can be extracted from the slope of the S_D–κ curve, and behaves as a material property: positive L_b values are usually associated with $Le > 1$ mixtures (flame speed decreases with stretch), whereas negative L_b values occur in lean hydrogen–air flames ($Le < 1$) where stretch enhances burning [31].

In counterflow flames, the situation is more complex. Both S_D and κ vary locally along a given progress-variable isosurface, and the value of S_D depends on which isosurface C^* is chosen. Poinsot and Veynante note that in stagnation geometries, this ambiguity can lead to non-monotonic variations of S_D with C, and therefore recommend defining L_b from the consumption speed S_c, which provides a unique, integrated flame speed for each imposed strain rate [31]. In principle, L_b could then be extracted by computing S_c across a series of strain rates.

In the present configuration, only two applied strain values were simulated, making such a regression impractical. Nevertheless, S_c was explicitly computed following an integral formulation. For each radial discretisation in the computational domain, flame normals were constructed, and the hydrogen rate of production ($\dot{\omega}_{\mathrm{H_2}}$) was sampled along these normal lines. The consumption speed was then evaluated by integrating the chemical source term along the flame normal:

$$S_c = -\frac{1}{\rho_u Y_{H_2,u}} \int_{-\infty}^{\infty} \dot{\omega}_{\mathrm{H_2}} ds \tag{4.5}$$

where ρ_u and $Y_{H_2,u}$ denote the density and hydrogen mass fraction of the unburnt gas, respectively, and ds is the arc length along the normal. In practice, ds was obtained from the spacing between consecutive discretisation points. The rate of production values was linearly interpolated to the midpoints of these intervals, such that each segment was represented by a cell-centred contribution. Multiplying the interpolated $\dot{\omega}_{\mathrm{H2}}$ by the corresponding ds and summing over all intervals provided the integral. Division by $\rho_u Y H_2, u$ yielded the final S_c value.

This formulation ensures that S_c is independent of any arbitrary choice of progress-variable isosurface and remains robust across different flame normals. Although only two applied strain rates were available in this study, preventing a direct regression for L_b, the methodology provides a consistent framework for comparing cases and for potential extension to larger parametric datasets.

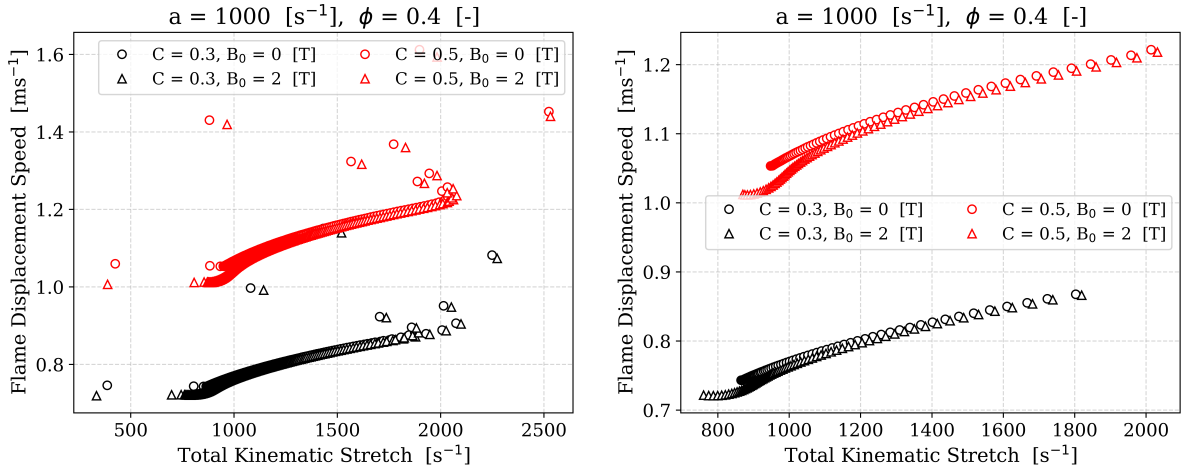

(a) Full (S_D, κ) scatter distribution extracted along isosurfaces $C = 0.3$ and $C = 0.5$ for two magnetic field cases ($B_0 = 0$ T and $B_0 = 2$ T).

(b) Subset of (S_D, κ) points restricted to the approximate small-stretch regime, illustrating the qualitative linear response.

Figure 4.8: Methodology for qualitative assessment of the displacement-based Markstein relation. (a) shows the full local scatter distribution, highlighting variability across the flame front. (b) isolates the small-stretch region where S_D–κ is approximately linear. These plots serve as diagnostics for the sensitivity of flame speed to stretch at different C^* values, without attempting a formal regression for L_b.

Complementary to this, local S_D–κ scatter plots were evaluated along several C^* isosurfaces ($0.1 \leq C \leq 0.7$). The purpose of these plots is not to extract L_b quantitatively, but to qualitatively assess the sensitivity of S_D to κ across different C^* values, thereby illustrating how apparent Markstein behaviour varies along the flame front. Within $C < 0.7$, the scatter shows an approximately linear trend, supporting the use of S_D as a local diagnostic of stretch effects.

4.3.3. Direct and Indirect Control Strategies

Magnetic fields influence transport in premixed reacting flows via two pathways: a *direct* pathway, which enters the governing equations as geometry-independent diffusion and heat–work terms, and an *indirect* pathway, which arises when magnetic forcing modifies the bulk convection and couples with geometry (curvature, strain, stagnation topology). In premixed flames, convection by itself shifts the flame without changing the internal flame structure; therefore, any convective influence is *indirect* and becomes effective only through its coupling with geometry and differential diffusion.

The *direct* contributions of magnetic fields manifest themselves first in the species conservation equation as the magnetic diffusion flux $\vec{J}_{M,i}$ (Equation 3.5), where a magnetophoretic gradient $\vec{M}_i$ drives an additional diffusive transport of species i independent of the flow geometry. This magnetically induced diffusion flux then appears in the energy equation as the magnetic interdiffusive heat flux $\vec{q}_{J_M}$ representing the enthalpy transport directly attributable to $\vec{J}_{M,i}$. In addition, the energy equation contains the *magnetic body force work* term

$$\sum_i \vec{f}_i \cdot \vec{J}_i,$$

where $\vec{J}_i$ is the total diffusive flux of species i. These three terms: $\vec{J}_{M,i}$, $\vec{q}_{J_M}$, and $\sum_i \vec{f}_i \cdot \vec{J}_i$, form the complete set of geometry-independent magnetic effects. Their magnitudes depend on species susceptibilities, local magnetic field gradients, and thermodynamic properties.

The *indirect* pathway originates from the momentum equation term $\sum_i Y_i \vec{f}_i$, where the net magnetic force density alters the bulk flow field. In a counterflow configuration, such changes in convection can modify the strain rate κ and flame curvature, shift the flame position relative to the stagnation plane, and change local mixture fraction gradients. These geometric modifications alter preferential diffusion behaviour: for $Le < 1$ lean hydrogen flames, a reduction in hydrogen enrichment ahead of the flame front decreases local mixture fraction, lowers the peak heat release rate $\dot{Q}$ and temperature T, and thereby reduces the Arrhenius rate constant $k \propto \exp(-E_a/RT)$. The consequent drop in reaction rate reduces the burning velocity S_L; conversely, in some regimes, induced curvature and strain changes can increase local enrichment and lead to S_L enhancement.

In summary, the direct effects act by explicitly adding magnetic diffusion and heat work terms to the transport equations, while the indirect effects work through magnetically altered convection coupled with geometry to modify the thermo-diffusive balance. The analysis in this work aims to compare the relative strengths of these control mechanisms to identify and establish a strategy to control hydrogen flames using magnetic fields.

4.3.4. Parametric Study

The parametric study examines how the effectiveness of magnetic flame control varies with changes in equivalence ratio ϕ and applied strain rate S. For each case, the analysis is based on the comparison of global flame parameters with and without the applied magnetic field, followed by a qualitative explanation of the observed trends in terms of changes in magnetic force magnitudes, flow inertia, and their interplay with the control mechanisms.

1. **Equivalence Ratio:** Cases at $\phi = 0.4$ and $\phi = 0.8$ were compared to assess the role of mixture composition on control effectiveness. Richer mixtures generally produce higher flame temperatures, which can increase the magnitude of magnetically induced forces through temperature-dependent species properties. Conversely, leaner mixtures exhibit lower thermal energy but may respond differently due to changes in density and diffusion characteristics. The differences in control effectiveness are interpreted in terms of these factors and their influence on both direct and indirect magnetic effects.
2. **Applied Strain Rate:** Strain rates of $a = 1000$ s^{-1} and $a = 2000$ s^{-1} were investigated to determine how applied strain rate impacts magnetic control. Higher strain rates can alter flame thickness and stability, while also affecting the velocity field against which the magnetic forces act. The resulting changes in the force-to-inertia ratio provide insight into why the magnetic influence is enhanced or diminished at different strain levels.

For all parametric variations, the interpretation remains focused on the observed changes in global flame behaviour and their correlation with the relative strength of the magnetic forcing compared to the flow's inertial and diffusive resistances.

4.3.5. Data Extraction and Processing

The raw data from OpenFOAM simulations are processed using a custom Python framework. The `foamcase.py` module provides the `foamCASE` class, which serves as the primary interface for loading and pre-processing the simulation results. This class utilises `pyvista` to read OpenFOAM data files (`.foam` extension) and extract relevant fields such as density (`rho`), velocity (`U`), temperature (`T`), pressure (`p`), and species mass fractions (`Y`). The processing workflow comprises several key steps:

Mesh Loading and Slicing

The `foamCASE` object first loads the mesh and solution data from the OpenFOAM case. For counterflow flames, only a specific 2D symmetry plane is required for analysis. The `read()` method uses the `OpenFOAMReader` in `pyvista` to read the mesh and field data, and slices the computational domain to extract the analysis plane.

Progress Variable Space

To facilitate the comparison of flames with different positions and curvatures, the simulation data were transformed from the physical (x, y) coordinate system into a (C, y) coordinate system, where C is the progress variable. This transformation allows alignment of the flame front across cases, removing apparent shifts and curvature effects when visualising the field variables. The transformation procedure treats all variables, whether scalar or vector components, initially in the same way, followed by an additional scaling for certain vector components as described below.

1. **Scalar Field Transformation:** For a given y-level, the set of (x, C) pairs is first extracted from the simulation data. All unique C values at that y-level are identified, denoted as C_{unique}. For each C_{unique} value, the corresponding values of the scalar variable (e.g. temperature T) are extracted. In most cases, this yields a single value per C_{unique}, except near $C \approx 0$ and $C \approx 1$ (e.g. $C \in [10^{-6}, 10^{-5}]$ or $1 - C \in [10^{-6}, 10^{-5}]$), where multiple points may occur due to mesh structure. In such cases, the average of these multiple values is taken.

   The resulting $(C_{\text{unique}}, \varphi_{\text{unique}})$ pairs (where φ represents the scalar field) are then interpolated onto a refined and uniform C grid, $C_{\text{uniform}} \in [0.0001, 0.9999]$, consisting of 1500 equally spaced points. A cubic interpolation scheme is applied:

$$\varphi_{\text{uniform}} = \mathcal{I}_{\text{cubic}} \left(C_{\text{unique}}, \varphi_{\text{unique}}; C_{\text{uniform}} \right)$$

   This procedure is repeated for each y-level, producing a uniform (C, y) representation for the scalar field.
2. **Vector Field Transformation and Scaling:** For vector quantities with x-components (e.g. u_x in m/s, $J_{x,i}$ in kg/(m^2,s)), the above interpolation procedure is first applied to each component as if it were a scalar. However, since these components are originally defined with respect to the x-coordinate, a scaling is applied to represent them correctly in the C-space. Specifically, the transformation

$$\frac{\partial}{\partial x} \rightarrow \frac{\partial}{\partial C} \frac{\partial C}{\partial x}$$

   implies that the x-components of velocities and fluxes are multiplied by $\dfrac{\partial C}{\partial x}$, effectively converting them from units referenced to x into a representation referenced to C.
3. **Data Interpretation:** In the progress variable space, iso-lines formally extend across the entire computational domain, whereas several diagnostic quantities (e.g., flame displacement speed and curvature) are physically meaningful only within the flame. To ensure consistency, the range of progress variable considered in this study is restricted to $0.015 \leq C \leq 0.985$, which effectively bounds the flame region. This interval already excludes far-field regions, since the flame itself is typically defined between $0.1 \leq C \leq 0.9$. As illustrated in Figure 4.9, the adopted range captures the flame structure while avoiding artefacts outside the reactive zone.

   For interpretation, a more targeted division is applied by analysing specific bands of progress variable associated with flame sub-structures. The interval $C \leq 0.6$ is identified as the preheat zone, while $0.6 \leq C \leq 0.9$ corresponds to the reaction zone. All quantitative discussions of magnetic field effects are therefore confined to these regions, which represent the physical loci of diffusive heating and dominant exothermicity, respectively. The extension of the upper bound to $C = 0.985$ is retained to ensure that late-forming species are fully captured: in particular, the peaks of OH and O occur around $C \approx 0.97$, and truncating below this value would omit important features of radical formation.
4. **Purpose and Limitations:** This transformation is intended solely for representation purposes. No physical gradients, divergences, or other differential operators are computed in the (C, y) space. The procedure allows direct visual comparison of fields in a flame-aligned coordinate system, mitigating the effects of curvature and displacement while preserving the original physical gradients in the (x, y) domain.

Gradient and Derivative Computations

The `foamCASE` class includes methods such as `compute_gradients()` and `compute_derivative()` to calculate spatial gradients, divergence, and other derivative quantities. These are essential for evaluating transport terms in the governing equations, including diffusive fluxes, convective terms, and source terms.

Residuals Analysis

When a residual file (`res_file`) is available, the `foamCASE` class can also load solver residual histories. This capability allows for a check on the convergence quality of the OpenFOAM simulations and for discarding any data from non-converged runs.

4.3.6. Summary of Analysis Approach

The analysis framework developed in this work integrates both physical diagnostics and computational tools to provide a rigorous basis for evaluating magnetic flame control. Global flame parameters such as thermal

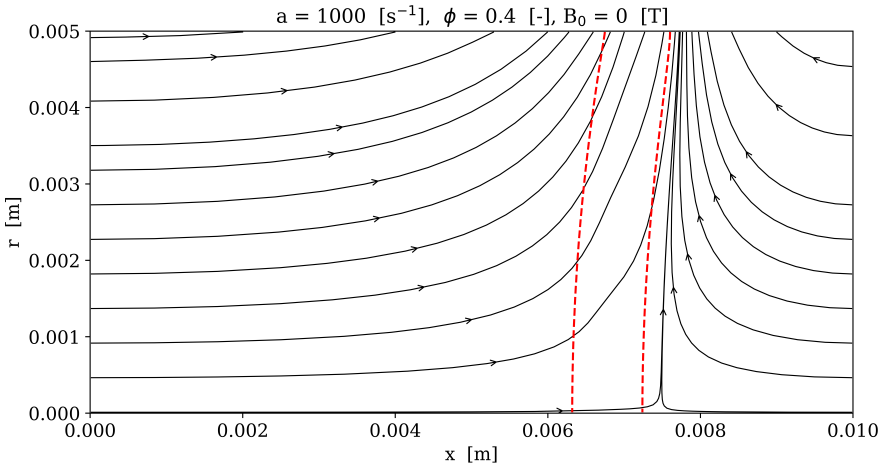

Figure 4.9: Spatial range of the progress variable space. The red-dashed lines represent the isocontour of the progress variable with isovalues $C = 0.015$ (left) and $C = 0.985$ (right).

thickness, displacement speed, and flame position establish baseline measures of flame structure and propagation. Instability metrics, including curvature, kinematic stretch rate, and Markstein length, enable mechanistic insight into thermo-diffusive behaviour and its modulation under magnetic forcing. The distinction between direct and indirect magnetic contributions links the governing equations to observable flame responses, while the parametric variations in equivalence ratio and strain rate test the robustness of these mechanisms under different operating conditions.

Complementing these diagnostics, a dedicated Python-based post-processing framework ensures consistent extraction, transformation, and interpolation of simulation data, allowing all cases to be compared in a flame-aligned coordinate system. This combination of physical interpretation, parametric evaluation, and robust data handling constitutes a comprehensive methodology for addressing the central research objective: to assess and quantify the feasibility of controlling lean hydrogen counterflow flames using applied magnetic fields.

5

Results

This chapter presents the central findings of the study in a structured sequence, progressing from reference cases to detailed mechanistic analysis. The effects of magnetic fields are interpreted relative to baseline conditions; therefore, the discussion begins by contrasting the fundamental behaviour of flames with unity and sub-unity Lewis numbers. Establishing these baseline characteristics provides the necessary framework to identify how magnetic forcing modifies flame dynamics.

Building on this foundation, the chapter then explores the selection and configuration of magnetic fields through Le = 1 flames before extending the analysis to Le < 1 cases. The subsequent sections assess their impact on global flame parameters, followed by the influence on instability measures such as curvature, stretch rate, and Markstein length. These observations motivate a deeper investigation into energy, species, and momentum transport mechanisms that mediate the changes. A final parametric study addresses the sensitivity of magnetic effects to strain rate and mixture richness, before concluding with an integrated discussion of the key outcomes.

5.1. Baseline Flame Characteristics

The baseline flame characteristics are first established for both the unity and sub-unity Lewis number cases, as these provide the reference conditions for all subsequent analyses. Since both flame types are used throughout the study, it is necessary to outline their intrinsic properties in the absence of magnetic fields. Presenting these baseline structures clarifies the spatial extent of the flames, their thermal thickness, and the associated profiles of temperature, mixture fraction, and species distributions. While differences between the two cases naturally emerge, most notably in flame position, thickness, and super-adiabatic flame temperatures, the primary purpose here is to document their fundamental behaviour and define consistent zones of preheat and reaction. This provides a clear starting point from which the role of magnetic fields on each flame type can be assessed in later sections.

5.1.1. Flame Structure

The flame front structure is first illustrated through the isocontours of the progress variable C for both $Le = 1$ and $Le < 1$ cases. These contours provide a visual indication of the spatial extent of the flame, as well as the relative flame thickness. Figure 5.1 shows the $C = 0.05$ and $C = 0.95$ isocontours extracted from the computed fields. The $Le = 1$ flame exhibits a compact front with a relatively sharp transition between reactants and products, consistent with diffusive balance at unity Lewis number. In contrast, the $Le < 1$ flame is more spatially extended, reflecting the enhanced diffusion of hydrogen relative to heat. This broadening is particularly evident in the separation between the $C = 0.05$ and $C = 0.95$ contours, which highlights the thicker preheat and reaction layers. Such spreading is a well-documented feature of hydrogen flames with $Le < 1$, where preferential diffusion effects lead to wider flame fronts and altered transport behaviour.

The differences in flame spreading can be quantified by examining the thermal flame thickness. Figure 5.2 compares global values with statistical estimates obtained from kernel-density evaluation. The global thickness is computed by utilising the maximum temperature gradient magnitude in the domain as the denominator in Equation 2.47. The statistical values are obtained by computing δ_L along each flame normal (accounting for curvature) and then forming a probability distribution, from which the mode is extracted.

For $Le = 1$, the representative thickness is $\delta_L \approx 0.269$, whereas for $Le < 1$ it increases to $\delta_L \approx 0.298$,

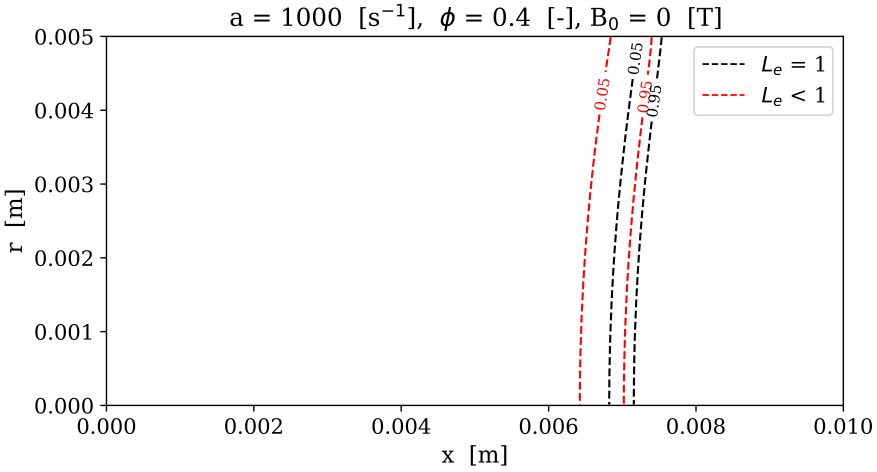

Figure 5.1: Progress variable isocontours ($C = 0.05$ and 0.95) for $Le = 1$ and $Le < 1$ flames. The $Le = 1$ flame shows a compact and sharp front, whereas the $Le < 1$ flame is significantly more spread due to preferential diffusion of hydrogen, resulting in thicker preheat and reaction layers.

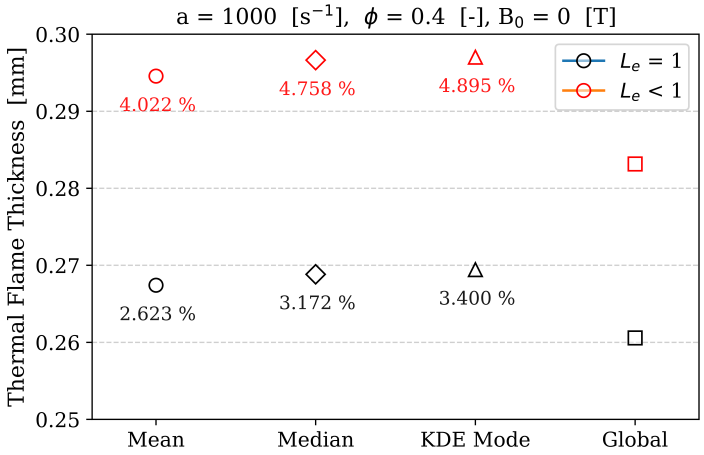

Figure 5.2: Statistical estimates of the thermal flame thickness compared with the global value. The percentages show the relative difference from the global value of that particular Lewis number case.

corresponding to a relative difference of about 11 %. This broader flame is consistent with the enhanced diffusivity of hydrogen. Within each case, the KDE mode is observed to be approximately 5 % higher than the global estimate. This deviation is not a physical effect, but rather reflects differences between global averaging and local statistical estimation methods. Overall, the results confirm that $Le < 1$ flames are systematically thicker, providing a more spread-out baseline structure for subsequent analysis.

Since the two cases differ in both flame thickness and spatial location, all subsequent fields are presented in the progress variable space. This ensures consistency in the analysis across the flames, allowing direct comparison of profiles and transport behaviour despite structural differences.

5.1.2. Centreline Temperature and Mixture Fraction Profiles

The centreline temperature profiles for $Le = 1$ and $Le < 1$ flames are shown in Figure 5.3. In physical space, the $Le = 1$ flame exhibits the expected sigmoid transition from unburnt to burnt gas, with the temperature smoothly increasing across the reaction zone. In contrast, the $Le < 1$ flame displays a super-adiabatic temperature rise, exceeding the adiabatic flame temperature. This behaviour arises due to preferential diffusion of hydrogen, which enriches the mixture locally in the reaction zone and drives stronger heat release.

When represented in progress variable space (Figure 5.3b), the trends become clearer: while both cases show an increase of temperature with C, the $Le < 1$ flame reaches a peak higher than the adiabatic flame temperature due to the additional fuel diffusion into the reaction zone. The super-adiabaticity observed here is consistent with

verified 1D solvers like Cantera in lean hydrogen flames, where differential diffusion of hydrogen leads to local enrichment and elevated temperature levels.

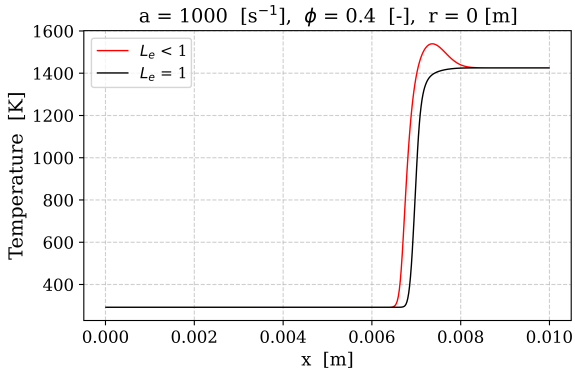

(a) Temperature profile at the centreline in physical space.

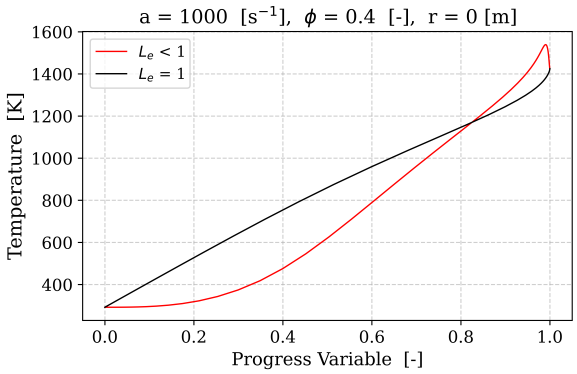

(b) Temperature profile at the centreline in progress variable space.

Figure 5.3: Centreline temperature profiles for $Le = 1$ and $Le < 1$ flames. The $Le = 1$ flame shows a smooth sigmoid transition, while the $Le < 1$ flame exhibits super-adiabatic temperatures due to preferential diffusion of hydrogen.

The mixture fraction distribution, plotted along the centreline in progress variable space, provides further insight into this super-adiabatic behaviour (Figure 5.4). For the $Le < 1$ flame, Z first decreases in the preheat zone, reflecting hydrogen diffusing out ahead of the flame front. However, as the reaction zone is approached ($C \gtrsim 0.8$), Z increases again due to hydrogen accumulation in the restrained environment. This two-regime behaviour directly explains the super-adiabatic temperature rise observed in Figure 5.3, as the additional local fuel supply intensifies reaction and heat release. In contrast, the $Le = 1$ flame shows no such deviation, with Z remaining essentially uniform since diffusion and heat transport are balanced.

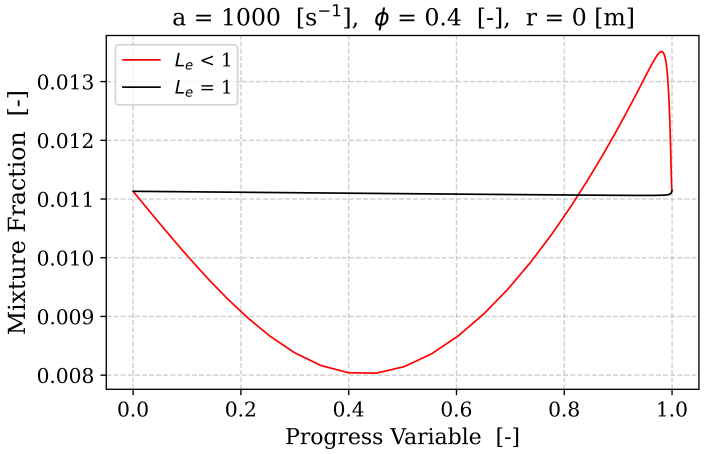

Figure 5.4: Centreline mixture fraction profiles in progress variable space. For $Le = 1$, Z remains nearly uniform across the flame, while for $Le < 1$ it first decreases in the preheat zone and then increases in the reaction zone, leading to local enrichment and super-adiabatic temperature rise.

5.1.3. Minor Species and Heat Release Rate

To delineate the flame's preheat and reaction zones, the centreline distributions of minor radical species (H, O, OH) are compared with the volumetric heat release rate $\dot{Q}$ in progress variable space (Figure 5.5). While radical concentrations provide useful indicators of chemical activity, their maxima do not necessarily coincide with the region of maximum exothermicity. In particular, the OH radical, commonly employed in experiments as a proxy for reaction intensity, has been shown not to align with the true HRR peak in premixed hydrogen flames. [38] demonstrated that, irrespective of equivalence ratio or strain rate, the OH* peak is displaced downstream of the heat release maximum.

As can be seen in Figure 5.5, the maximum heat release lies between $C = 0.6$ and $C = 0.9$. We therefore define the preheat zone as $C \lesssim 0.6$ and the reaction zone as $0.6 \lesssim C \lesssim 0.9$, which encompasses the dominant exothermic region. This convention ensures consistency with both theoretical flame structure descriptions and hydrogen-specific findings.

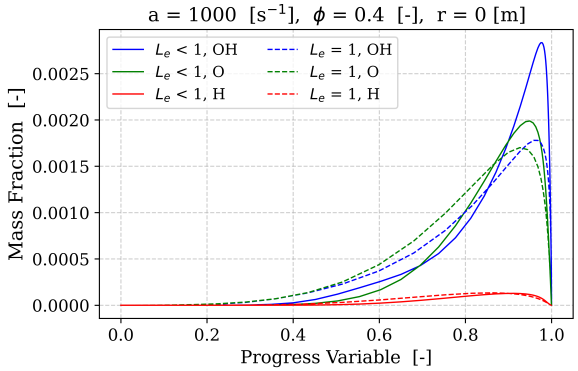

(a) Minor radical mass fractions (H, O, OH) along the centreline in progress variable space.

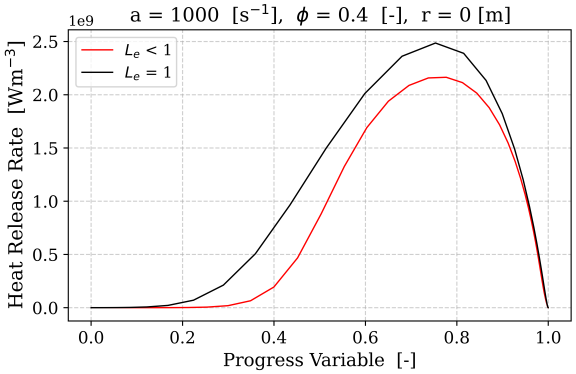

(b) Heat release rate at the centreline in progress variable space.

Figure 5.5: Centreline profiles of minor species and heat release rate. Consistent with [38], the reaction zone is defined by the HRR peak, which lies between $C = 0.6$ and $C = 0.9$. The OH* peak is shifted downstream because of excited-state kinetics, making HRR the more reliable zone marker.

5.1.4. Major Species and Choice of Progress Variable

To motivate the choice of the progress variable definition used throughout this study, the centreline distributions of major species are presented in both physical and progress variable space (Figure 5.6). The main species of interest are the fuel (H_2), oxidiser (O_2), and the primary product (H_2O).

For $Le = 1$, all species profiles exhibit smooth monotonic transitions across the flame, with fuel consumption directly mirrored by oxidiser depletion and product formation. For $Le < 1$, however, the influence of preferential diffusion is evident. The O_2 and the H_2O distribution show a non-monotonic trend with the progress variable. These non-monotonic behaviours highlight that O_2 or H_2O are not ideal choices for defining a progress variable, as they do not provide a consistently increasing or decreasing marker across the flame.

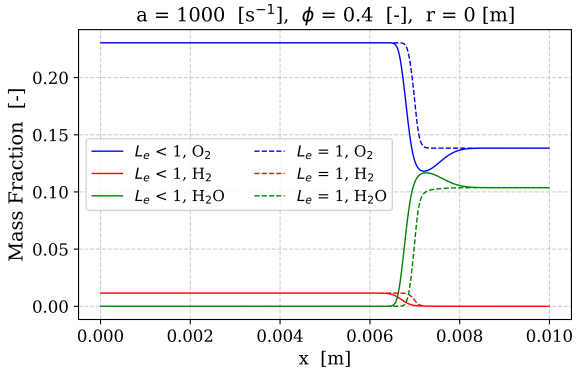

(a) Major species mass fraction profiles along the centreline in progress variable space.

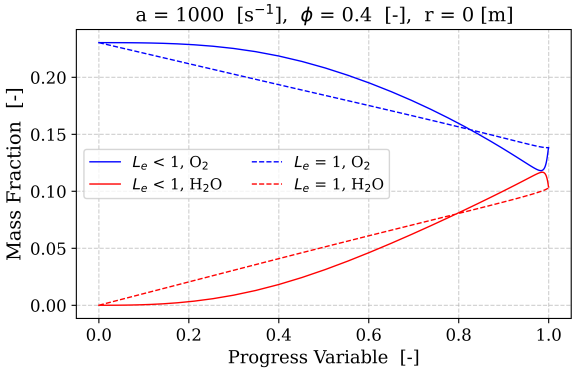

(b) Major species mass fraction profiles along the centreline in progress variable space.

Figure 5.6: Major species distributions in physical and progress variable space. Non-monotonic behaviour of O_2 and H_2O under $Le < 1$ conditions makes them unsuitable as progress variable definitions. Hydrogen decreases monotonically, making it a reliable choice for defining C.

In contrast, hydrogen shows a monotonic decrease from its unburnt to burnt state across all cases, making it a robust marker of reaction progress. For this reason, we define the progress variable as per Equation 4.2. This choice ensures that C varies smoothly from 0 to 1 and provides a physically consistent representation of flame advancement. The selection of fuel-based definitions of C is widely employed in hydrogen flame studies, given

the monotonicity of fuel consumption compared to oxidiser or product species.

5.2. Magnetic Field Selection

Having established the baseline flame behaviour in the absence of external forcing, the analysis is extended to assess how applied magnetic fields influence the unity Lewis number configuration. In this regime, thermo-diffusive instabilities are suppressed, so any observable changes in flame structure must arise from the imposed magnetic forcing alone. This makes it possible to disentangle the direct action of magnetic diffusion terms from the indirect modifications of the velocity field driven by paramagnetic oxygen. The simulations span a systematic range of field strengths and orientations, allowing the influence of intensity and configuration to be examined independently. By comparing these cases, the analysis identifies whether measurable variations in temperature fields, global flame parameters, and flow patterns occur under unity Lewis number conditions, and thereby sets a reference for interpreting the richer dynamics expected in $Le < 1$ flames.

5.2.1. Field Strengths

To evaluate the threshold effects of magnetic fields, flame behaviour was simulated for various magnetic field strengths: 0 T, 0.5 T, 1.0 T, 1.5 T, and 2.0 T. The objective was to determine whether the magnetic field effects increase linearly with field strength or if a particular threshold induces more significant changes in flame dynamics. Since this study considers a unity Lewis number case, the changes observed are not due to differential diffusion effects but primarily related to the shift of the flame as a result of the magnetic field's influence on the flow. The following figures show the flow field and isocontours of the progress variable C (represented by dashed lines) for each magnetic field strength, zoomed near the flame region.

At a magnetic field strength of 0.5 T (Figure 5.7), the shift in the flame position is barely noticeable. The field has minimal effect on the flame structure, with the isocontours of C showing no substantial shift. The flame remains essentially in its original position, suggesting that at 0.5 T, the magnetic field does not significantly affect the flow or the flame position.

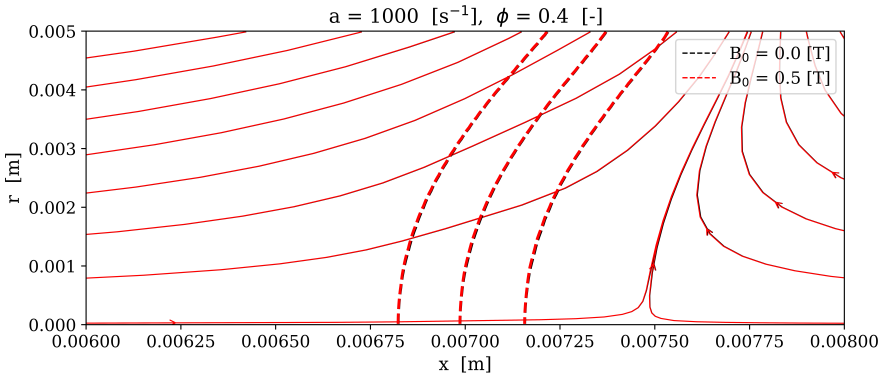

Figure 5.7: Flow field and isocontours of progress variable $C = 0.05, 0.5, 0.95$ (dashed lines) for 0 T and 0.5 T fields, zoomed near the flame region. The magnetic field at 0.5 T results in negligible changes to the flame position, with no observable shift.

Upon increasing the field strength to 1.0 T (Figure 5.8), a slight shift in the flame position upstream becomes evident. The flame moves slightly against the flow direction, indicating that the 1.0 T field is beginning to reduce the flow's inertia. The change remains subtle, and the flame still maintains a relatively similar position compared to the 0.5 T case.

At 1.5 T, the flame's shift upstream is more noticeable. The magnetic forces begin to significantly reduce the inertia of the incoming flow, leading to a clearer upstream displacement of the flame and the stagnation plane. The flame front moves further upstream, indicating that the magnetic field is increasingly influencing the flame dynamics by slowing the incoming flow.

At the maximum field strength of 2.0 T (Figure 5.9), the shift in the flame position becomes significantly larger. The flame and stagnation plane are clearly displaced upstream, with the isocontours of C showing a distinguishable shift. This result confirms that at 2.0 T, the magnetic field effectively reduces the flow's inertia to the greatest extent, leading to a prominent displacement of the flame upstream.

These observations demonstrate that the effect of magnetic fields on the flame structure increases with field strength, with the primary effect being a shift of the flame upstream, toward the stagnation plane. The magnetic

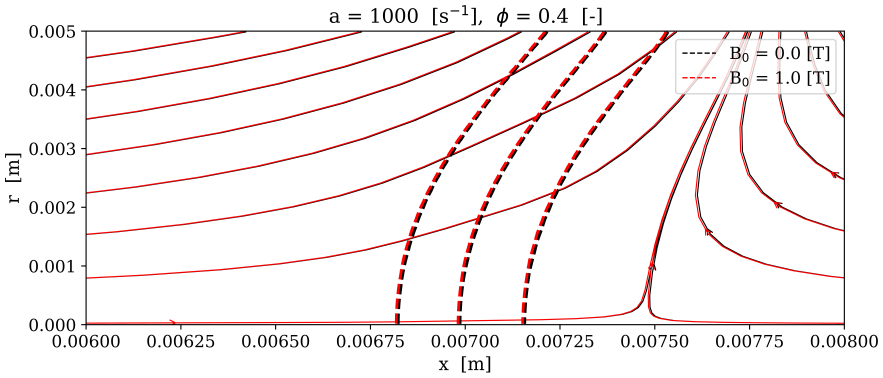

Figure 5.8: Flow field and isocontours of progress variable $C = 0.05, 0.5, 0.95$ (dashed lines) for 0 T and 1.0 T fields, zoomed near the flame region. The flame shifts upstream in response to the magnetic field at 1.0 T, although the change remains subtle.

forces reduce the incoming flow's inertia, pushing the flame in the opposite direction to the flow. The flame curvature and diffusion processes remain unaffected, as expected for a unity Lewis number case, where preferential diffusion effects are absent.

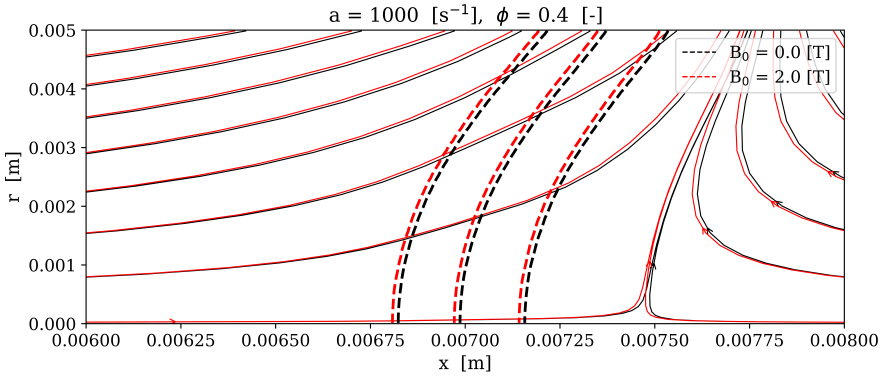

Figure 5.9: Flow field and isocontours of progress variable C (dashed lines) for 0 T and 2.0 T fields, zoomed near the flame region. A distinguishable upstream shift of the flame is observed, indicating the most pronounced effect of the magnetic field at 2.0 T.

Given that the 2 T field produces the most distinct shift in flame position, it was selected for further analysis to explore the effects of different magnetic field configurations. The following section will investigate how axial, radial, and Gaussian field profiles at this 2 T strength affect the flame dynamics, helping to identify which configuration results in the most significant changes in flame behaviour.

5.2.2. Field Topology

Building upon the findings from the previous section, where we concluded that a 2 T magnetic field shows the most distinguishable effect among the various field strengths, we now explore the impact of different magnetic field topologies on flame dynamics. Specifically, we analyse four field configurations: axially decreasing, axial Gaussian, radially decreasing, and radially increasing, to investigate their effects on the flame position and structure. The goal is to determine which configuration induces the most pronounced shift in the flame and provides the most practical application in the context of flame control.

Axially Decaying Field

The axially decaying magnetic field, as shown in Figure 4.2a, produces a subtle upstream shift in the flame position (Figure 5.10). This field is defined by the equation

$$B_x(x) = B_0 \exp(-kx),$$

with the strength decaying along the axis. As seen in the figure, the flame front shifts upstream, but there is no significant change in the flame's curvature or structure. The primary effect of the axial decaying field is the

reduction of flow inertia, which leads to a slight upstream displacement of the flame and stagnation plane. The forces are aligned against the flow direction, reducing the velocity of the incoming flow and pushing the flame upstream. However, the magnitude of the effect is minimal, and the flame's overall shape remains unchanged.

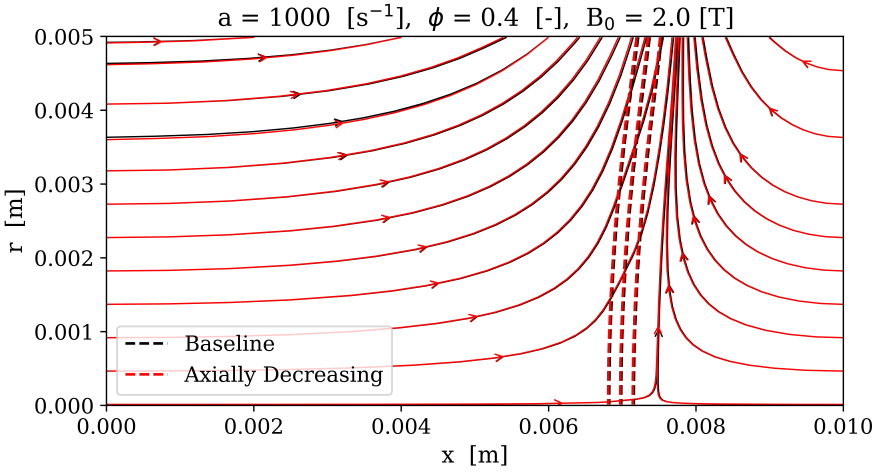

Figure 5.10: Flow field and isocontours of progress variable C (dashed lines) for the axially decaying 2 T field. The magnetic field produces a subtle upstream shift in the flame position without significant changes to flame curvature. The primary effect is the reduction of flow inertia, pushing the flame upstream.

Axial Gaussian Field

The axial Gaussian field, shown in Figure 4.2b, exhibits a different behaviour. This field has a spatially localized peak, which induces forces that are directed towards the flow direction, i.e., towards from the stagnation plane. As a result, this field increases the flow's inertia near the flame, leading to a minor shift in the flame's position downstream (Figure 5.11). However, the overall effect remains minimal. While the Gaussian field does influence the flow dynamics, its impact on the flame structure is not as pronounced. In this case, the forces generated by the Gaussian profile do not reduce flow inertia significantly but instead contribute to a slight increase in the incoming flow's velocity. Therefore, the flame's shift is less pronounced, and the changes in flame position remain small.

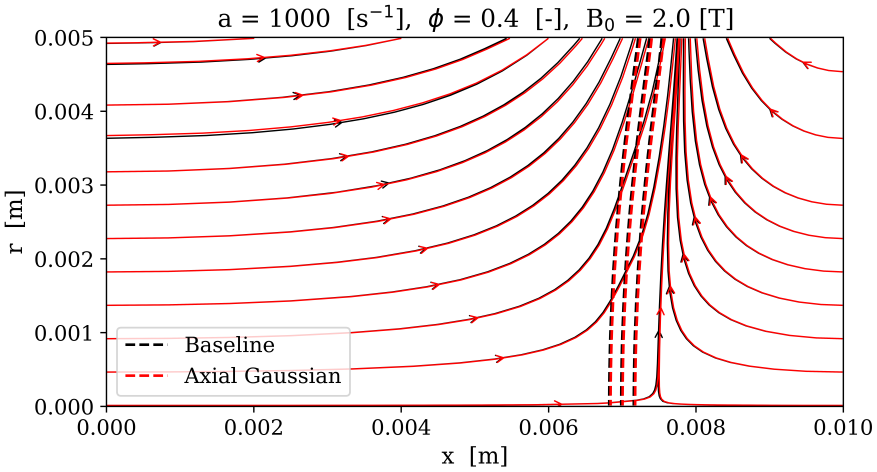

Figure 5.11: Flow field and isocontours of progress variable C (dashed lines) for the axial Gaussian 2 T field. The forces generated by the Gaussian field increase the flow inertia, leading to a minor shift of the flame downstream. However, the changes are still minimal and do not significantly alter the flame position or curvature.

Radially Decreasing Field

The radially decreasing magnetic field, depicted in Figure 4.2c, produces the most distinguishable effect on the flame. In this configuration, the magnetic forces are applied in the radial direction and decay with distance from

the axis, leading to a stronger effect near the centerline of the flame. The result is a clear shift of the flame downstream and an observable change in the flame curvature near the axis (Figure 5.12). This field configuration has the most noticeable influence on the flame structure, as it induces changes both in the flame's position and its shape.

The key advantage of the radially decreasing field is that it is practically realizable in many experimental setups. By placing the magnetic poles along the axis, it is possible to create this type of field in a controlled environment. This configuration provides a good balance between practical feasibility and effectiveness in flame control. The pronounced downstream shift, combined with the curvature change, makes this topology an ideal candidate for further analysis in the context of $Le < 1$ cases, where flame instability and stretch sensitivity are more significant.

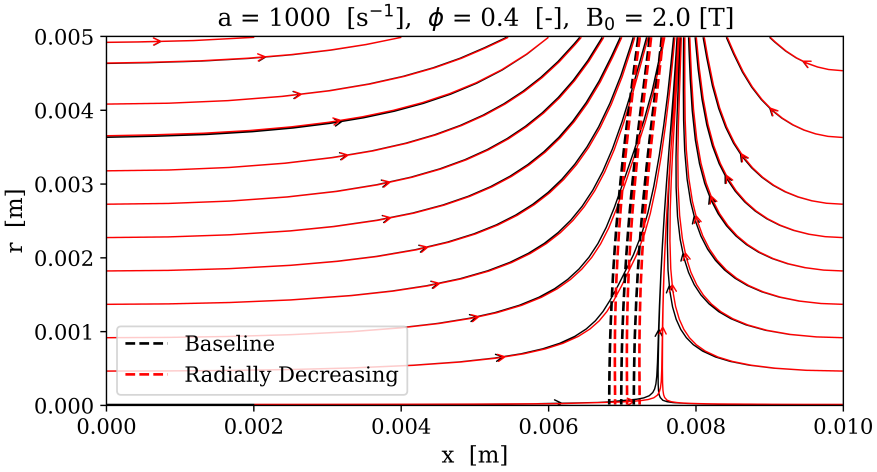

Figure 5.12: Flow field and isocontours of progress variable C (dashed lines) for the radially decreasing 2 T field. The field induces the most significant downstream shift in the flame position and alters the flame curvature near the axis. This configuration is also practically realisable, making it the preferred choice for further analysis.

Radially Increasing Field

Finally, the radially increasing magnetic field, shown in Figure 4.2d, has a more complex effect on the flame. This configuration, where the field strength increases radially from the centre towards the outer boundary, induces a shift in the flame position upstream. It also leads to a change in the flame curvature near the axis (Figure 5.13). However, the overall effect is minimal compared to the radially decreasing field. Furthermore, this configuration is difficult to realise practically without intruding on the flow, making it less desirable for real-world applications.

Although this field configuration does induce a flame shift and curvature change, the effects are weaker than those of the radially decreasing field, and the practical challenges in generating such a field make it less feasible. As a result, this topology was rejected in favour of the radially decreasing field, which provides a more pronounced and realisable effect.

In summary, the analysis of the four magnetic field topologies reveals that the radially decreasing field produces the most significant and practical effects on the flame structure. This configuration not only induces the most pronounced downstream shift in the flame but also alters the flame curvature near the axis, making it the most effective and realisable topology for controlling flame position. Due to its practical feasibility and effectiveness, the radially decreasing field was chosen as the final configuration for further analysis in $Le < 1$ cases, where differential diffusion effects and thermo-diffusive instabilities play a more prominent role.

5.3. Impact of Magnetic Fields on Global Parameters

This section establishes how a radially decreasing magnetic field modifies *macroscopic* properties of a lean H_2/air counterflow flame with differential diffusion enabled. The forcing landscape is first characterised so that the subsequent global comparisons to the 0 T baseline can be interpreted in a consistent physical setting. Throughout, results are reported in the combustion–coordinate system with fixed zone thresholds: the *preheat* band is taken as $C < 0.6$ and the *reaction* band as $0.7 \leq C \leq 0.9$.

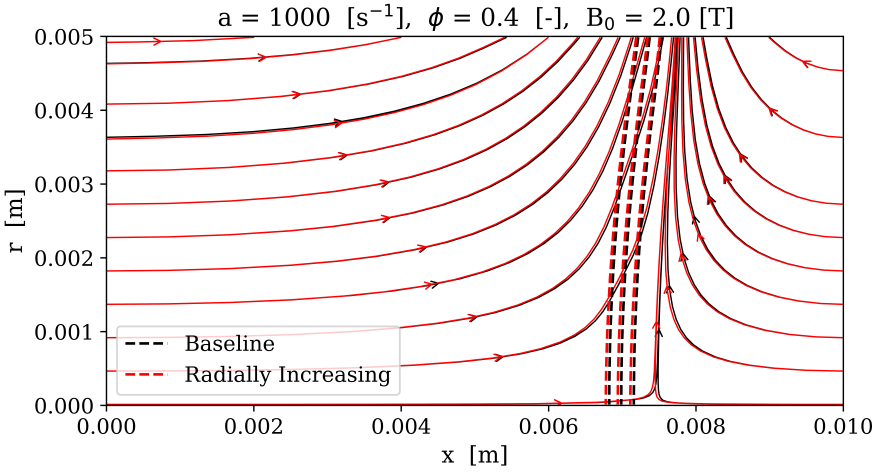

Figure 5.13: Flow field and isocontours of progress variable C (dashed lines) for the radially increasing 2 T field. Although this field shifts the flame upstream and alters its curvature near the axis, the effect is minimal. Additionally, this configuration is challenging to realise in practical setups, leading to its rejection.

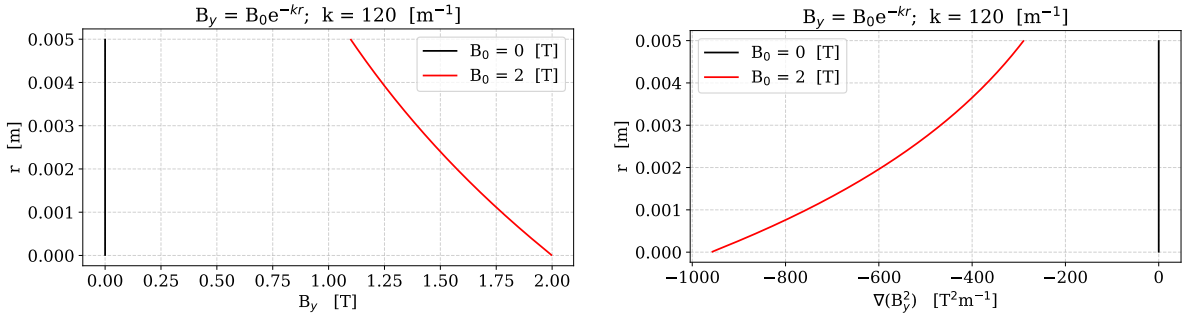

(a) y–component of the magnetic field, B_y.

(b) Squared gradient of B_y (proxy for regions of strongest forcing).

Figure 5.14: Radially decreasing magnetic–field configuration used for all comparisons. Gradients, and hence body–force intensity on paramagnetic species, concentrate near the axis on the cold side of the flame; the influence weakens downstream as temperature rises.

Figure 5.14 summarises both the field orientation and where forcing is expected to be most effective. In the counterflow geometry, the highest gradients occur near the axis upstream of the flame, so magnetic influence is anticipated to imprint primarily within the preheat band before weakening across the reaction band owing to the temperature dependence of susceptibility and the competing effects of thermal expansion.

5.3.1. Flow Field and Flame Interaction

This section examines the interaction between the flow field and the flame, focusing on how the magnetic field influences flame dynamics. The flame displacement and reduction in laminar flame speed are analysed, along with the effects of convection and strain rates on the flame structure.

Flame Position Shift

As shown in Figure 5.15, the flame and stagnation point shift towards the product gases. For a counterflow configuration, the axial velocity decreases closer to the stagnation point. Since the flame front is nearly planar, this shift towards a low axial velocity region could be due to either a reduction in laminar flame speed (S_L) or an increase in convective velocity at the flame front. Since the flame is stationary, the flame speed is given by:

$$S_D = -\vec{v} \cdot \hat{n}$$

where $\vec{v}$ is the velocity vector and $\hat{n}$ is the unit normal vector to the flame front. A reduction in S_L indicates that the flame stabilises at a lower speed, potentially due to the magnetic field's impact on species diffusion or reaction rate.

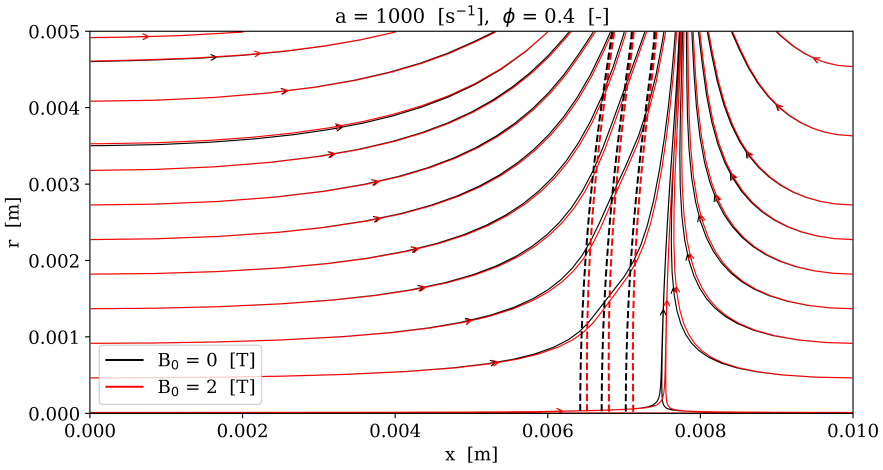

Figure 5.15: Velocity streamlines in radially decreasing magnetic field configuration. The dashed lines represent the iso-contours of the progress variable C with iso-values 0.05 (left), 0.5 and 0.95 (right).

The difference plot of the laminar flame speed (shown in Figure 5.16) reveals an approximate 5% reduction in S_D near the axis in the reaction zone. This decrease is primarily attributed to changes in the kinetic speed and strain effects within the flame. A reduction in S_D suggests that the flame front is stabilising at a slower speed, which can be further explored by comparing the displacement speeds.

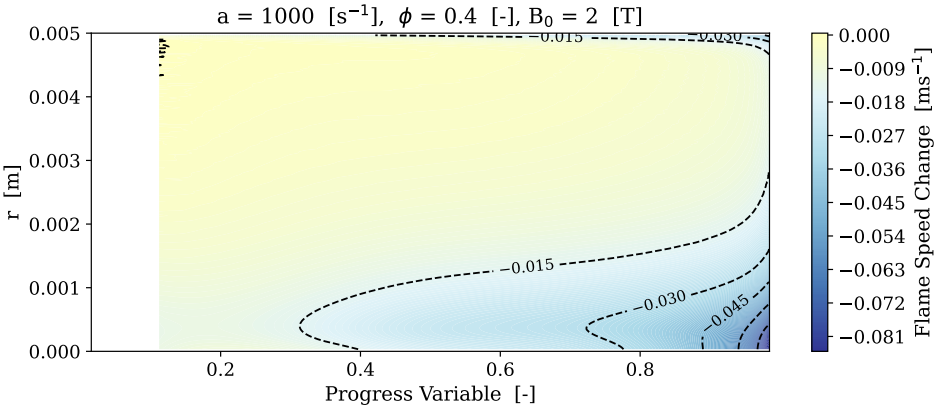

Figure 5.16: Absolute change in the laminar flame speed S_D from the base case in the progress variable space.

Flame Displacement Speed

The flame displacement speed (S_D) represents the propagation speed of the flame front. The displacement speed (Equation 4.3) can be decomposed into S_D^k and S_D^{diff}, representing the kinetic and diffusion components of the flame displacement speed, respectively.

Figure 5.17 shows a reduction in the flame displacement speed S_D in the flame coordinate system. The reduction in the flame displacement speed is observed to be in the range of 4.5% to 6%, with the primary contributor being the decrease in kinetic displacement speed (S_D^k), which is influenced by the rate of species consumption.

Kinetic vs. Diffusion Contributions

Figure 5.18a shows that the reduction in the flame displacement speed is predominantly attributed to the decrease in kinetic displacement speed (S_D^k), which is influenced by the rate of hydrogen consumption ($\dot{\omega}_{H_2}$). This reduction is due to lower species concentrations and temperature, with temperature being the dominant factor, as reaction rates are exponentially dependent on temperature.

Although Figure 5.18b shows that there is an increase in the diffusion displacement speed (S_D^{diff}) due to increased tangential strain and increased hydrogen diffusion due to convective accumulation, the kinetic speed reduction remains the dominant factor for the overall decrease in the flame speed.

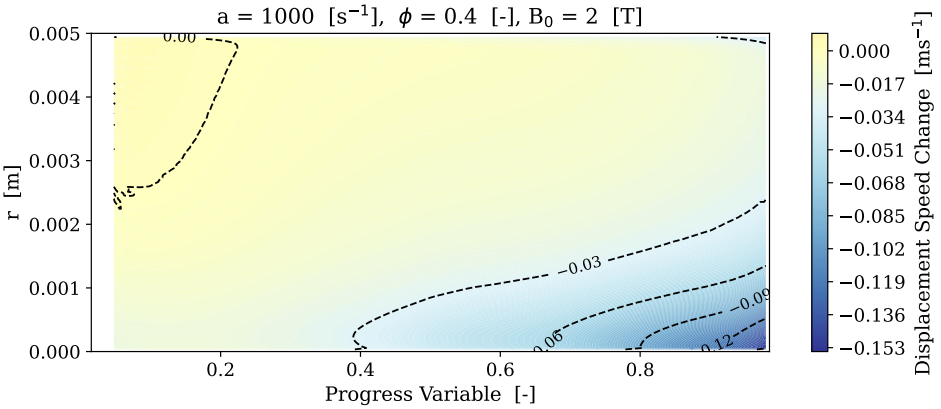

Figure 5.17: Absolute change in the flame displacement S_D from the base case in the progress variable space.

5.3.2. Flame Thickness

Figure 5.19 compares four statistical representatives of the local–normal thermal flame thickness field: the mean, the 10% trimmed mean, the median, and the kernel–density (KDE) mode. The global flame thickness is also presented to analyse the difference in behaviour between the statistical estimates and the global value. Black markers denote the 0 T case and red markers the 2 T case.

Across all four statistics, the change from 0 T to 2 T is negligible, with all estimates and the global value within 0.5% difference: mean $+0.133\%$, trimmed mean $+0.069\%$, median -0.081%, KDE mode $+0.157\%$, and the global value -0.476%. Within the present resolution, the applied 2 T field does not produce a meaningful change in the representative thermal thickness.

5.4. Influence on Instability Parameters

This section presents an analysis of the influence of magnetic fields on the key parameters influencing flame instability. The analysis focuses on how changes in the global flame parameters, radical redistribution and temperature change affect flame curvature, stretch rate and Markstein Length. These parameters are crucial for understanding the dynamics of flame propagation, particularly under varying strain rates and magnetic field configurations. Each subsection will explore how these parameters interact with one another and how their modifications affect the flame's response to instabilities.

5.4.1. Flame Curvature

Flame curvature significantly influences the behaviour of premixed flames, primarily through two distinct mechanisms: flame stretch effects induced by curvature and the subsequent chemical-thermal energy imbalance. For flames characterised by a Lewis number $Le < 1$, curvature plays a particularly crucial role in determining local flame characteristics.

A flame surface with positive curvature (convex shape towards the unburnt gas) promotes greater chemical energy influx compared to the thermal energy loss due to geometrically divergent heat diffusion. In systems where $Le < 1$, the chemical energy diffusion (predominantly driven by species with high diffusivity, such as hydrogen) significantly outweighs thermal energy diffusion, leading to local enrichment and a resultant increase in burning intensity and flame temperature. Conversely, regions exhibiting negative curvature (concave shape towards the unburnt gas) experience increased outward diffusion of species, causing local lean conditions. This imbalance can lead to reduced flame temperature, weakening of reaction rates, and in extreme cases, local flame extinction or opening.

To clearly illustrate this effect, Figure 5.20 shows the flame curvature under two conditions: without magnetic influence ($B_0 = 0$ T) and with a radially decreasing magnetic field of peak intensity $B_0 = 2$ T. In the absence of a magnetic field (Figure 5.20a), the flame surface exhibits predominantly convex curvature. Upon application of a magnetic field (Figure 5.20b), the flame's curvature becomes noticeably concave near the axis and further convex in the mid-radial region.

The observed changes in flame curvature under magnetic influence arise from two main phenomena. First, the magnetic field enhances axial velocity near the axis, causing a backwards displacement of the flame front closer to the stagnation plane. This displacement inherently increases convexity in the mid-radial regions of the flame.

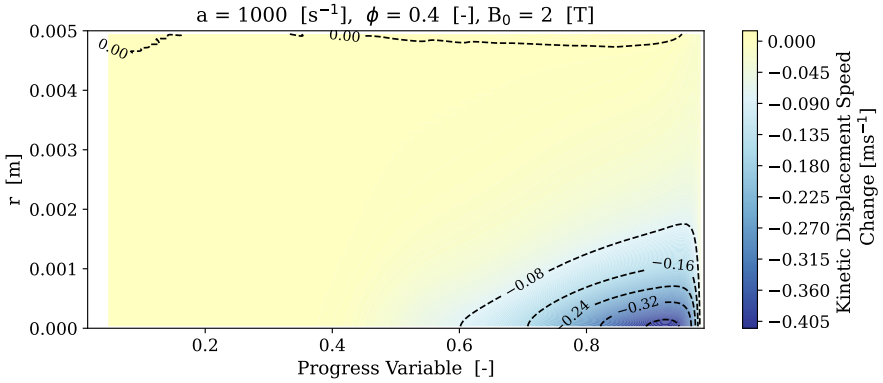

(a) Change in kinetic displacement speed S_D^k.

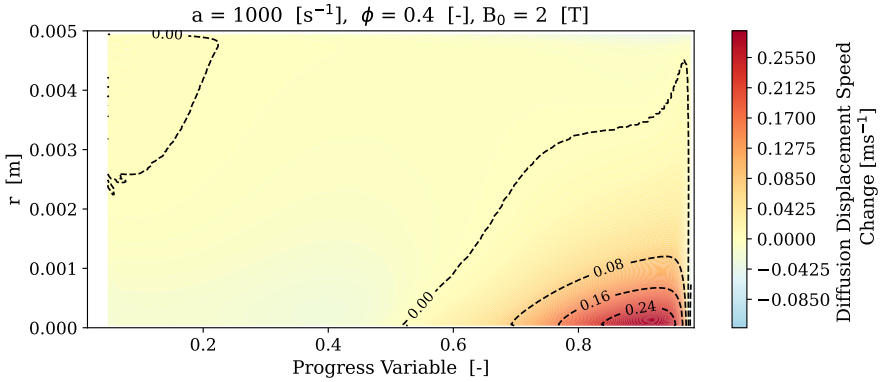

(b) Change in diffusion displacement speed S_D^{diff}.

Figure 5.18: Component-wise absolute change in the flame displacement speed S_D. The reduction in kinetic speed S_D^k dominates the increase due to diffusion speed S_D^{diff}, resulting in an overall reduction of the displacement speed

Second, a significant reduction in temperature near the axis further affects flame stabilisation. This reduction is most pronounced at the flame centreline and progressively decreases radially outward, resulting in a radial gradient of the kinetic flame speed (S_D^k). Near the axis, S_D^k is the lowest, positioning the flame closest to the stagnation plane. With increasing radial distance, S_D^k rises, stabilising the flame progressively further from the stagnation plane. This interplay between velocity and temperature gradients manifests as the observed concave curvature near the axis. The resultant concavity further intensifies the local chemical-thermal energy imbalance, exacerbating the reduction in the reaction rate and amplifying the risk of local flame extinction.

Thus, the applied magnetic field not only modifies the flame's geometric structure but also significantly alters the local flame chemistry and temperature distribution, highlighting the complex interplay between curvature, stretch, and diffusion processes in flames characterised by $Le < 1$.

5.4.2. Kinematic Stretch Rate

The total kinematic stretch rate is decomposed into the tangential strain rate and the curvature–induced contribution multiplied by the local displacement speed, both evaluated along the flame normal. Results are discussed in the progress variable space, with the preheat layers at $C < 0.7$ and the reaction layers at $0.7 \leq C \leq 0.95$.

The total kinematic stretch experiences a net *reduction* at 2 T (Figure 5.21), most prominently in the preheat layers near the axis (order 5–13% decrease). However, the tangential strain rate decreases in the preheat region by roughly 5–8% but *increases* by about 6–8% in the reaction layers (Figure 5.22). Thus, this overall reduction in the kinematic stretch rate is attributed to curvature-induced strain, which is evident from the flame curvature change from convex to concave near the axis. Even though the curvature-induced strain is negligible compared to the tangential strain, the change in the total kinematic stretch is dominated by the reduction in the curvature-induced strain. This spatial contrast aligns with the velocity changes in the progress variable space: the axial component decreases almost everywhere (Figure 5.23), while the radial component exhibits a two-regime behaviour (Figure 5.24). Near the axis and at low C, the radial sweep weakens, lowering the local tangential strain

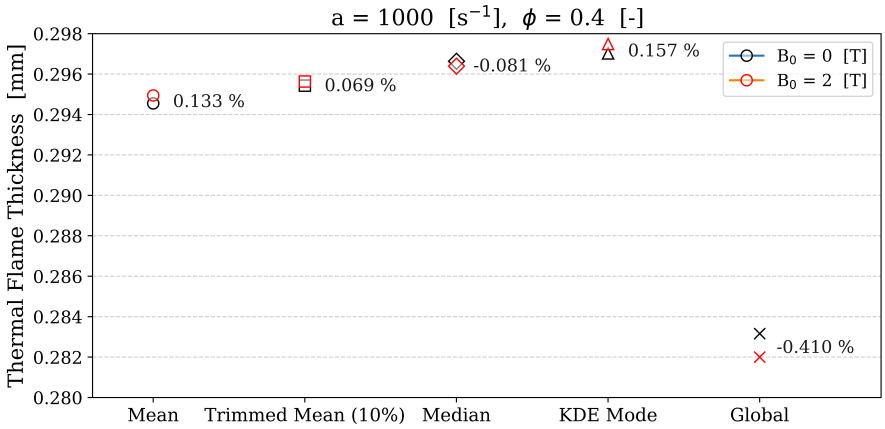

Figure 5.19: Statistical representatives of the local–normal thermal flame thickness δ_L for a lean H_2/air counterflow flame at $a = 1000$ s^{-1} and $\phi = 0.4$. Markers show mean, 10% trimmed mean, median, and KDE mode for $B_0 = 0$ T and $B_0 = 2$ T. All estimates and the global value witness negligible changes (< 0.5 %). The KDE Mode estimate shows a 0.16 % increase in the flame thickness while the global values depict a 0.4 % reduction in flame thickness.

in the preheat layers. Downstream in C (beyond $C \approx 0.5$) and closer to the stagnation region, the axial inflow that remains must be redirected radially for mass conservation; this strengthens the radial sweep and produces the observed 6–8% rise in tangential strain across the reaction layers.

The curvature–induced contribution changes sign near the axis (front becomes concave to the reactants) and its magnitude increases sufficiently that its *reduction* overwhelms the modest increase in tangential strain. In relative terms, the curvature term exhibits a change exceeding 100% (a sign reversal), so although the tangential strain grows in the reaction layers, the net effect on the sum is a decrease in the total stretch of order 5–13%. This explains why the total-stretch map shows a widespread negative change while remaining positive in absolute terms.

The redistribution between tangential strain and curvature stretch under magnetic forcing has direct implications for the flame's response to stretch sensitivity. In particular, the relative weakening of preheat-zone stretch and the curvature reversal near the axis are closely tied to the effective Markstein behaviour of the flame, which encapsulates how displacement speed adjusts to imposed stretch. The next subsection, therefore, quantifies this impact through the evaluation of the Markstein length.

5.4.3. Markstein Length

The Markstein length (L_b) is an important parameter quantifying the sensitivity of flame speed to variations in stretch rate. The impact of the applied radially decreasing magnetic field on the Markstein length is qualitatively assessed in Figure 5.25.

As shown in Figure 5.25, there is a clear reduction in the flame displacement speed (S_D) near the flame axis under magnetic field influence. This indicates an increased sensitivity of the flame speed to stretch effects in this region. However, despite the observed changes in flame speed, the slope of the relationship between flame speed and stretch rate (and thus the Markstein length) appears unchanged when compared to the non-magnetised case. This observation is consistent across different values of the progress variable (C), as illustrated in Figure 5.25.

This invariance is further captured by the negligible change in the consumption speed of the flame shown in Figure 5.26, which plots the radial variation of the flame consumption speed for $B_0 = 0$ T and 2 T.

These findings suggest that while the radially decreasing magnetic field notably affects local flame speed distributions, particularly at lower stretch conditions, it does not significantly alter the Markstein length itself. This indicates that the intrinsic sensitivity of the flame to stretch, as captured by the Markstein length, remains robust against magnetic field-induced modifications, despite noticeable local flame speed variations.

The analysis presented in this section highlights the significant roles of flame curvature, kinematic stretch rate, and Markstein length in governing flame stability under the influence of magnetic fields. Notably, the primary effects resulting from these variable changes predominantly manifest as reductions in kinetic flame properties, notably flame displacement and kinetic speeds, which are closely linked to the local reaction rates. Since the rate of reaction is exponentially sensitive to temperature, the observed variations in kinetic quantities inherently point towards the critical role of temperature distribution within the flame structure. Consequently, to fully elucidate

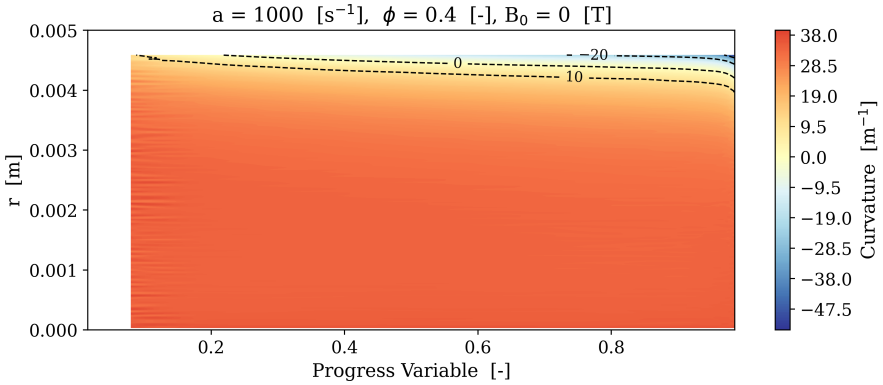

(a) Flame curvature $\nabla \cdot \hat{n}$ for $B_0 = 0$ T. Positive values imply convexity while negative values imply concavity.

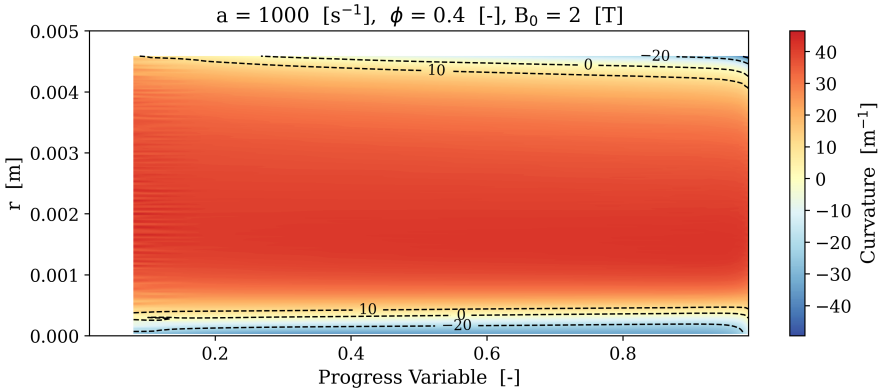

(b) Flame curvature $\nabla \cdot \hat{n}$ for $B_0 = 2$ T. Positive values imply convexity while negative values imply concavity.

Figure 5.20: Illustration of flame curvature demonstrating the effects of a radially decreasing magnetic field configuration. The flame surface curvature changes from purely convex (no magnetic field) to partially concave near the axis and increasingly convex in the mid-radial region under magnetic influence.

these observed phenomena and their implications on flame stability, an in-depth analysis of energy transport mechanisms, particularly temperature variations induced by magnetic fields, will be undertaken in the subsequent section.

5.5. Energy Transport Mechanisms

The evolution of the temperature field within a reacting flow is governed by the conservation of energy, which, under transient conditions with magnetic field effects, is expressed as:

$$\rho \frac{\partial h}{\partial t} = - \underbrace{\vec{\phi} \cdot \nabla h}_{\text{Convective Transport}} - \underbrace{\nabla \cdot \vec{q}}_{\text{Diffusive Transport}} + \underbrace{\sum_i h_i(-\dot{\omega}_i)}_{\text{Heat Release Rate}} + \underbrace{\sum_i \vec{f}_i \cdot \vec{J}_i}_{\text{Body Force Work}}$$

where h denotes the specific sensible enthalpy and $\vec{\phi}$ is the mass flux vector. The convective and diffusive contributions are governed by the convective enthalpy flux $h\vec{\phi}$ and the total diffusive heat flux $\vec{q}$, respectively. At steady state, the net change in thermal energy within a control volume is determined by the balance among these four competing mechanisms.

Figure 5.27 presents the spatial variation in the temperature field induced by the application of a radially decaying magnetic field with a peak strength of $B_0 = 2$ T. A temperature reduction of approximately 10–13 K (corresponding to a relative change of about 1–2 %) is observed near the flame axis within the reaction zone. This implies a shift in the local energy balance, indicating that the magnetic field has influenced either the transport or the source terms in the energy equation.

To evaluate whether this observed reduction in temperature is a direct consequence of magnetic field effects, such as body force work or magnetically induced diffusion fluxes, or the result of indirect mechanisms, such as

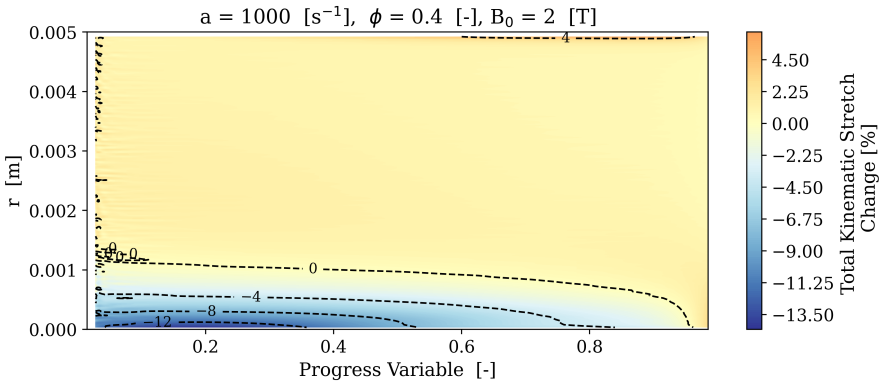

Figure 5.21: Relative change in total kinematic stretch (per cent) for the 2 T case at $a = 1000\ \mathrm{s}^{-1}$ and $\phi = 0.4$. The field is reduced most strongly near the axis and in the preheat layers (order 5–13% decrease).

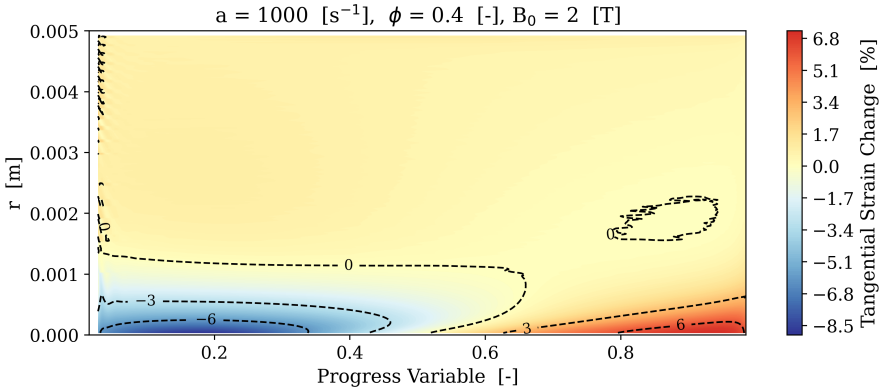

Figure 5.22: Relative change in tangential strain rate (per cent). A decrease of ∼5–8% is observed in the preheat layers, whereas the reaction layers exhibit a consistent increase of ∼6–8%.

changes in local mixture composition and subsequent variation in heat release, the following subsection analyses and compares the relative contributions of each term in the energy equation. This allows identification of the dominant mechanism responsible for the shift in thermal balance.

5.5.1. Mechanism Analysis

The terms in the energy transport equation, namely convection, diffusion, heat release rate, and body force work, can be broadly categorised into two classes: (i) transport-based flux mechanisms, consisting of convection and thermal diffusion, and (ii) volumetric source/sink mechanisms, consisting of chemical heat release and body force work. While the former redistributes thermal energy spatially, the latter generates or absorbs thermal energy locally within the flow field.

As evident from Figure 5.28, the contribution of magnetic body force work is several orders of magnitude (approximately 8–9) smaller than the other thermal mechanisms. This confirms that direct magnetic contributions to the energy balance via body force work are negligible and can be omitted from further analysis.

The dominant mechanism governing the observed temperature decrease is instead the reduction in heat release rate $\dot{Q}$. This decline is most prominent near the axis within the reaction zone, and contributes substantially to the enthalpy reduction in that region (Figure 5.28a). Moreover, a net decrease in $\dot{Q}$ is observed throughout the flame domain, consistent with the overall temperature reduction previously discussed.

Key observations from Figure 5.29 and Figure 5.28 are as follows:

1. **Heat Release Rate ($\dot{Q}$):** A sharp reduction is observed near the flame axis within the reaction zone, which correlates strongly with the observed enthalpy and temperature drops. The reduction in $\dot{Q}$ appears to be the primary driver of the overall decrease in thermal energy.
2. **Convective Contribution:** Convection primarily enhances enthalpy in the preheat zone, especially near the axis (Figure 5.29a). A detailed investigation of the convective mechanism is provided in the following

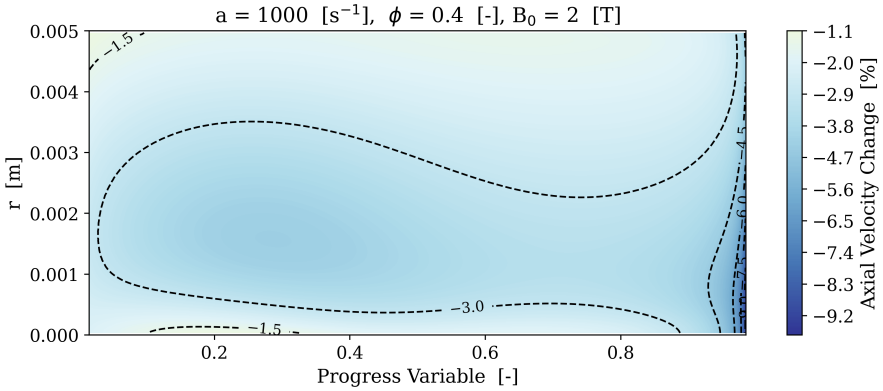

Figure 5.23: Relative change in axial velocity (per cent) in the progress variable space. The axial component weakens across the field, with the strongest reductions close to the axis and towards larger C.

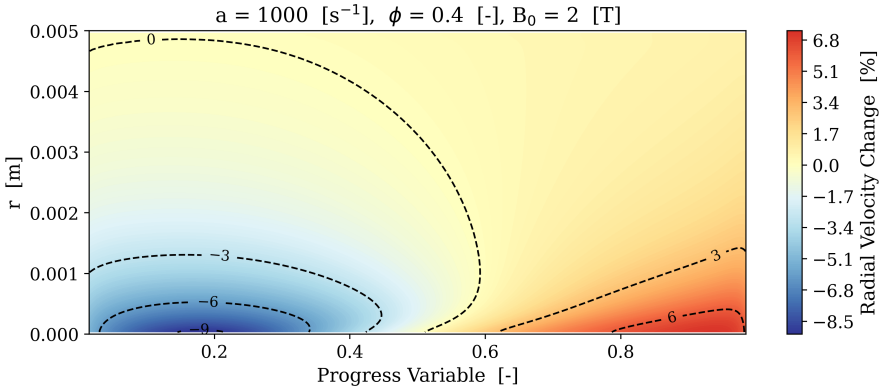

Figure 5.24: Relative change in radial velocity (per cent). The radial sweep weakens in the preheat layers near the axis but strengthens beyond $C \approx 0.5$ and across the reaction layers, consistent with enhanced axial-to-radial redistribution near the stagnation region.

subsection and will be discussed further in the context of the momentum equation.

3. **Diffusive Response:** Thermal diffusion acts as a stabilising mechanism, redistributing energy from the relatively enriched preheat zone to compensate for losses in the reaction zone (Figure 5.29b). A detailed analysis of diffusion will be presented in a dedicated section.

Taken together, these results indicate that the dominant thermal influence of the magnetic field manifests indirectly, primarily through the modulation of heat release rather than via direct magnetic body force effects. Magnetic field-induced alterations in bulk flow and local mixture composition likely drive this indirect influence. In particular, local enrichment or depletion of reactants (e.g., oxygen or hydrogen) can affect the mixture fraction, resulting in changes in the local equivalence ratio and, consequently, the heat release rate.

This hypothesis will be explored further in the context of species transport. However, before proceeding to that, the following subsection presents a detailed analysis of the convective mechanism, which is found to play a significant role in shifting thermal energy into the preheat zone and potentially modifying the local reactivity field.

5.5.2. Convective Heat Flux

The influence of magnetic fields on the convective heat flux is visualised in Figure 5.30, which shows the spatial variation in the convective enthalpy flux within the progress variable space. The plotted contours represent the change in volumetric convective heat generation, with streamlines superimposed to illustrate the net convective transport pathways.

The results indicate a net influx of convective energy from the reaction zone into the preheat zone, which is primarily attributed to a combination of two effects: (i) a magnetic field-induced shift in the flow field, and (ii) a modified flame position relative to the stagnation plane. This combined displacement redistributes the axial velocity field in a manner that promotes increased upstream transport of enthalpy.

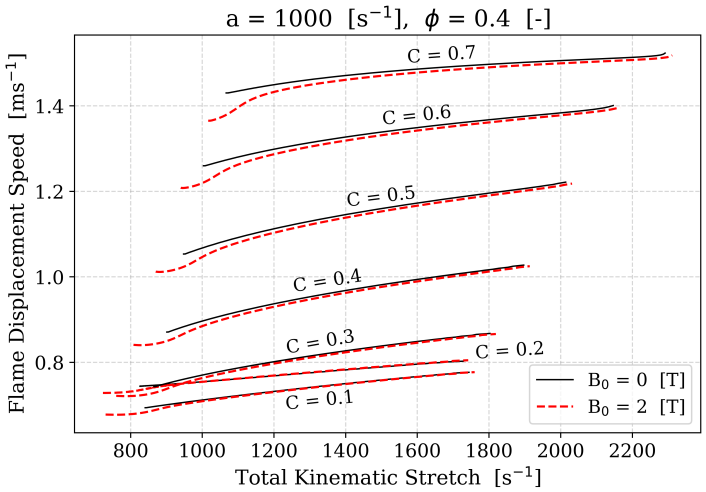

Figure 5.25: Qualitative assessment of the Markstein length (L_b) under the influence of radially decreasing magnetic fields. A notable reduction in flame speed is primarily evident at low-stretch regions; however, the Markstein length remains largely unchanged.

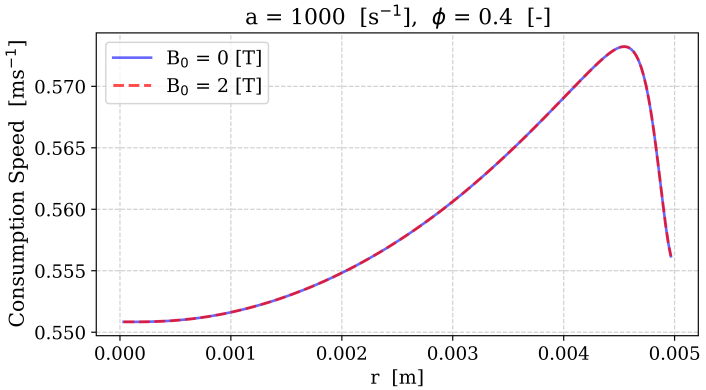

Figure 5.26: Flame Consumption Speed for 0 T and 2 T cases. Although results show a radial variation in S_c, this change is insignificant and the values are nearly constant.

A more detailed breakdown reveals that axial convection is the primary driver of this increase in upstream convective heat flux. In contrast, radial convection slightly offsets this effect, acting to weaken the net heat input in certain regions. To fully interpret the magnetic field's influence on convection, especially the apparent reduction in axial heat convection near the axis, a detailed analysis of the underlying mass flux field is required. This will be addressed in the dedicated momentum transport mechanism analysis section.

In summary, convection plays a non-negligible role in redistributing thermal energy across the flame, particularly through increased enthalpy transport into the preheat zone. However, since the magnetic field's direct control over convection is limited to radial dynamics, its potential for targeted thermal control via convection alone appears limited. To explore whether a more direct control pathway exists, the next subsection focuses on diffusive heat transfer, with special attention to identifying whether magnetic fields can meaningfully influence thermal diffusion through interdiffusive mechanisms. This analysis will help determine the feasibility of using magnetic fields as an active control strategy through the modulation of multicomponent diffusion.

5.5.3. Diffusive Heat Flux

Diffusive heat transfer within the reacting flow is governed by the diffusive flux vector $\vec{q}$, which comprises conductive and interdiffusive contributions, expressed as:

$$\vec{q} = \vec{q}_c + \vec{q}_J$$

Here, $\vec{q}_c$ represents the conductive heat flux, while $\vec{q}_J$ corresponds to the interdiffusive heat flux. The interdiffusive flux, in turn, includes contributions from species gradients ($\vec{q}_{J_Y}$) as well as from magnetically induced

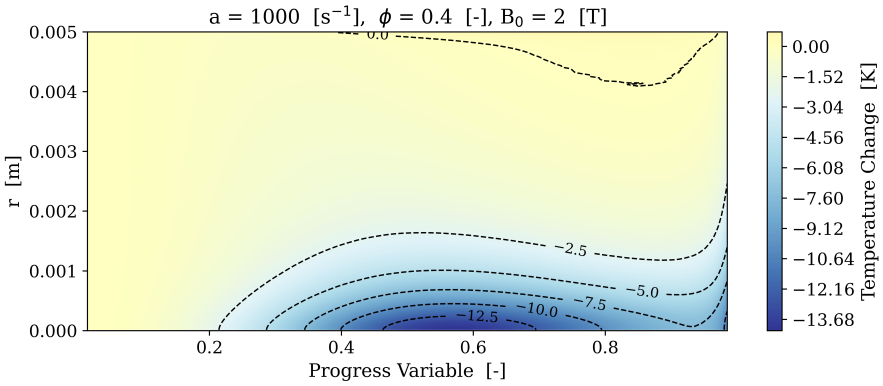

(a) Absolute change in the temperature field in the progress variable space.

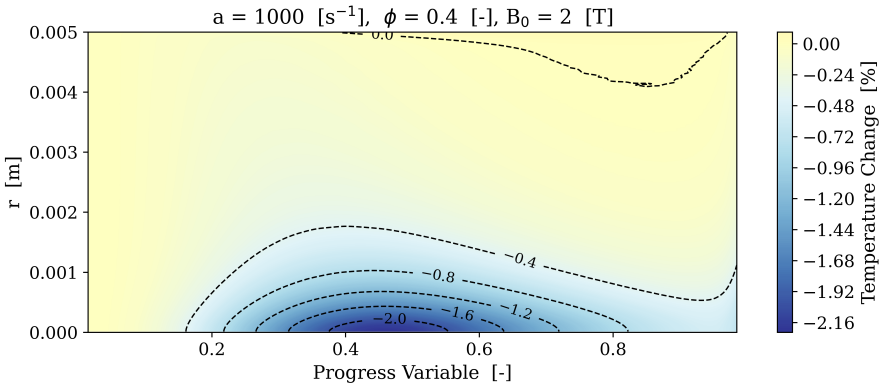

(b) Relative change in the temperature field in the progress variable space.

Figure 5.27: Change in the temperature field under the influence of a radially decreasing magnetic field configuration. Around 1–2 % reduction is observed in the reaction zone, corresponding to an absolute reduction of approximately 10–13 K.

diffusion fluxes ($\vec{q}_{J_M}$). Diffusion acts as a smoothing mechanism, redistributing thermal energy and reducing gradients induced by the other transport processes, such as convective heat transfer and heat release. Therefore, diffusion can be viewed as a secondary mechanism arising in response to alterations in local temperature gradients driven by factors like changes in reaction rates or species distribution.

The shift in the diffusive heat flux pattern under the influence of the magnetic field is illustrated in Figure 5.31. The figure indicates a net radially inward and axially forward diffusive flux, resulting in heat generation within the reaction zone and heat depletion in the preheat zone.

As previously discussed, diffusion exhibits the least pronounced influence among the three primary heat transport mechanisms (convection, diffusion, and heat release). Nevertheless, the magnetic field's direct impact on diffusion manifests through the magnetic diffusion flux, driven by magnetophoretic gradients (which will be elaborated upon in the species transport mechanism analysis). To identify the dominant diffusive mechanism, a detailed comparative study between conductive and interdiffusive flux contributions is performed in the following subsections.

Conduction

Figure 5.32 illustrates the change in conductive heat generation resulting from the application of a radially decreasing magnetic field. Comparison with the overall diffusive pattern shown earlier in Figure 5.29b indicates that conductive heat transfer dominates the diffusive response. The significant alteration in conductive flux patterns strongly suggests that the magnetic field indirectly influences diffusion through modifications in the local temperature gradient, itself driven by the altered heat release rate.

Interdiffusion

The interdiffusive heat flux ($\vec{q}_J$) comprises two distinct components: the species gradient-driven interdiffusive flux ($\vec{q}_{J_Y}$) and the magnetically induced interdiffusive flux ($\vec{q}_{J_M}$). These are expressed collectively as:

$$\vec{q}_J = \vec{q}_{J_Y} + \vec{q}_{J_M}$$

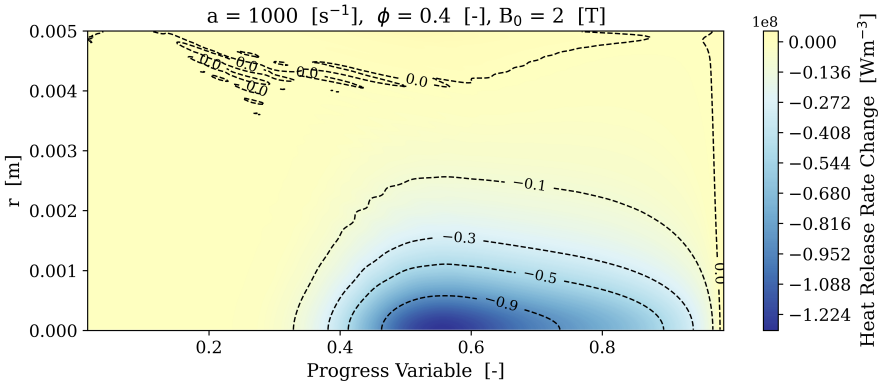

(a) Change in the volumetric heat release rate in the progress variable space.

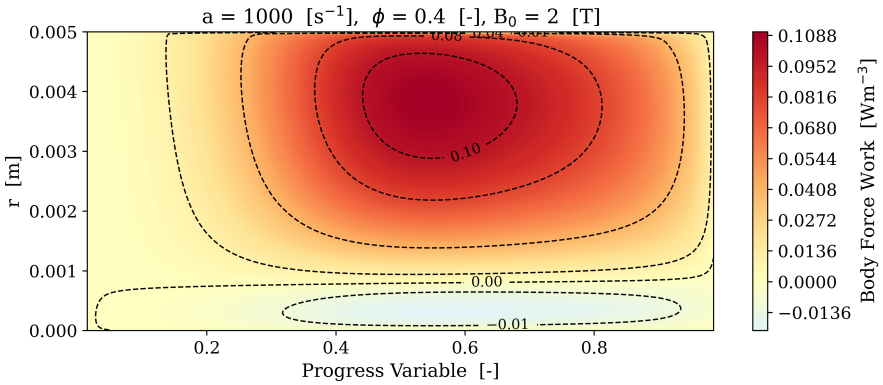

(b) Volumetric heat generation due to the work done by the magnetic body force.

Figure 5.28: Illustration of the change in volumetric heat generation due to source/sink mechanisms. Results show that the heat release rate decreases by approximately 5% in the reaction zone and remains the dominant thermal mechanism. In contrast, the contribution from body force work is at least eight orders of magnitude smaller.

Figure 5.33 compares these two interdiffusion contributions. It is evident from the magnitude comparison presented in the figures that the magnetophoretic gradient-driven diffusive flux ($\vec{q}_{J_M}$) is several orders of magnitude (approximately seven orders lower) smaller than the species gradient-driven flux ($\vec{q}_{J_Y}$). This significant disparity conclusively indicates that direct magnetic control of heat transfer via magnetically induced interdiffusion is practically negligible in the current configuration, precluding its use as a viable direct magnetic control strategy.

An interesting contrast emerges upon examining Figure 5.33a and Figure 5.32. The conductive heat flux and species gradient-driven interdiffusion exhibit opposing effects. Specifically, conduction acts to increase thermal energy in the reaction zone and remove it from the preheat zone. In contrast, species gradient-driven interdiffusion transports thermal energy away from the reaction zone and deposits it into the preheat zone. This directional opposition is explicitly illustrated in Figure 5.34, which presents the altered pattern of interdiffusive heat flux induced by species concentration gradients.

Given that species gradient-driven interdiffusion inherently depends upon the species diffusion fluxes, a detailed investigation of this mechanism's underlying dynamics is essential. This aspect will therefore be further analysed in the subsequent section dedicated to species transport mechanisms. Such an investigation will clarify the precise role of species gradients and their coupling with thermal energy redistribution under magnetic field influences.

5.5.4. Heat Release Rate

The heat source term $\dot{Q}$ has emerged as the dominant mechanism influencing the energy transport within the flame. The observed reduction in heat release, particularly pronounced near the axis in the reaction zone, is clearly illustrated in Figure 5.28a.

The term $\dot{Q}$ originates from exothermic reactions described by detailed chemical kinetics, such as those encapsulated in the San Diego Mechanism for hydrogen-air combustion, comprising 21 elementary reactions. Previous

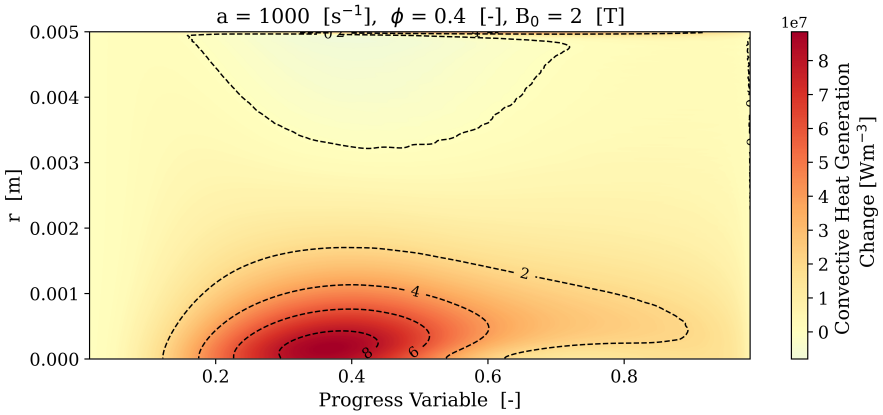

(a) Change in the volumetric convective heat flux in the progress variable space.

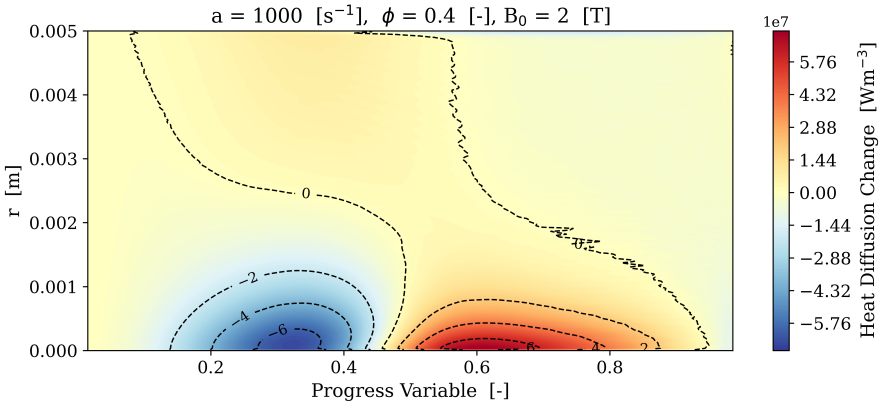

(b) Change in the volumetric diffusive heat flux in the progress variable space.

Figure 5.29: Illustration of the change in thermal energy redistribution via transport-based mechanisms. Convection increases thermal flux in the preheat zone near the axis, while diffusion attempts to smooth the imbalances created by convective and reactive shifts.

analysis identified the species production rate $\dot{\omega}_i$ as the critical variable governing heat release. For a general reversible reaction $aA + bB \underset{k_r}{\overset{k_f}{\longleftrightarrow}} cC + dD$, the reaction rate r is formulated as:

$$r = k_f[A]^a[B]^b - k_r[C]^c[D]^d; \quad \frac{k_f}{k_r} = K_c = \exp\left(-\frac{\Delta G^\circ}{RT}\right)$$

The production rate for each species i is expressed as:

$$\dot{\omega}_i = \nu_i r$$

Here, ν_i is negative for reactants and positive for products. Consequently, for any species involved in multiple reactions, the overall species production rate depends on both the local concentration of reacting species and the reaction rate constant k for each specific reaction. For the San Diego Mechanism, the majority of reactions follow Arrhenius kinetics, described by:

$$k = AT^\beta e^{-\frac{E_a}{RT}}$$

Accurately resolving $\dot{Q}$ by individually tracking species production rates and concentrations presents substantial computational challenges due to the stiffness of the governing chemical kinetics equations, their sensitivity to rapid local concentration fluctuations, and pronounced temperature dependencies. To circumvent this complexity while retaining critical combustion dynamics, a simplified conserved scalar is required. This scalar should be chemically inert, capturing only mixing and transport processes while remaining unaffected by reaction chemistry.

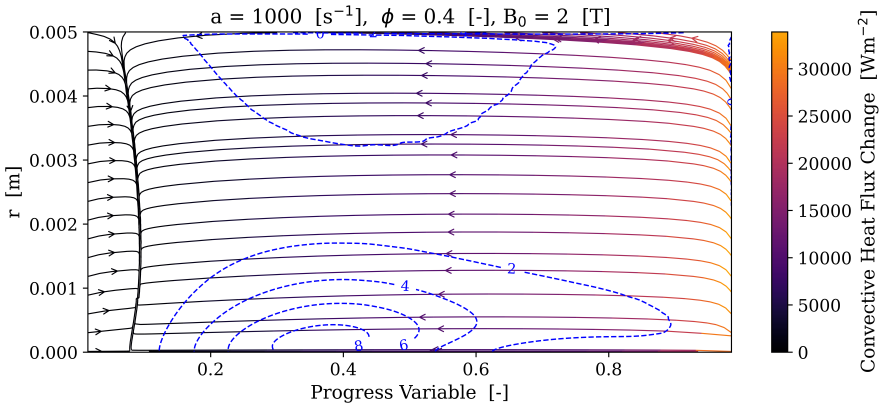

Figure 5.30: Change in the convective heat flux in the progress variable space. Blue contours indicate the volumetric convective heat generation. The observed pattern reflects a net influx of enthalpy from the reaction zone into the preheat zone, driven by shifts in both the flow field and the flame front.

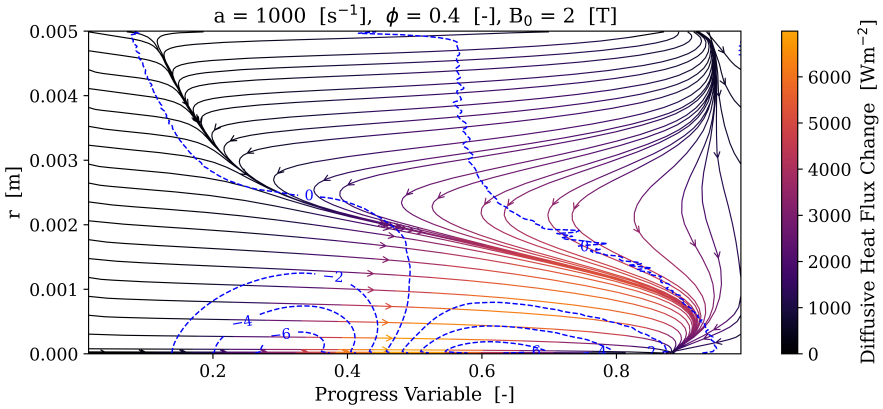

Figure 5.31: Change in the total diffusive heat flux pattern, overlaid with contours representing total diffusive heat generation (blue dashed lines). Results demonstrate a net radially inward and axially forward diffusion, causing heat accumulation in the reaction zone and depletion in the preheat zone.

Bilger Mixture Fraction

While individual species concentrations can vary substantially due to chemical reactions within a flame, the elemental mass fractions remain conserved. This elemental conservation underpins the utility of an element-based mixture fraction as a chemically inert scalar, providing a robust variable for simplified combustion analysis. For hydrogen-air combustion, the Bilger mixture fraction Z is particularly suitable and is employed in this analysis to interpret local mixture composition changes resulting from the applied magnetic field.

Figure 5.35 illustrates the effect of the radially decreasing magnetic field on the distribution of the Bilger mixture fraction within the progress variable space. In Figure 5.35a, the absolute change in mixture fraction clearly indicates a reduction near the flame axis within the reaction zone. Figure 5.35b quantifies this reduction, showing an approximately 2% decrease in the local mixture fraction. This observed decrease in Z indicates a shift toward leaner local conditions, thereby significantly affecting the local heat release rate. Thus, the reduction in mixture fraction emerges as the primary contributor to the overall reduction in heat release observed under the influence of a magnetic field.

The Bilger mixture fraction Z can be expressed as a linear combination of species mass fractions Y_i:

$$Z = \sum_{i\ =\ \text{species}} A_i Y_i + A_1$$

where the coefficients A_i are species-specific sensitivity parameters reflecting how strongly each species mass

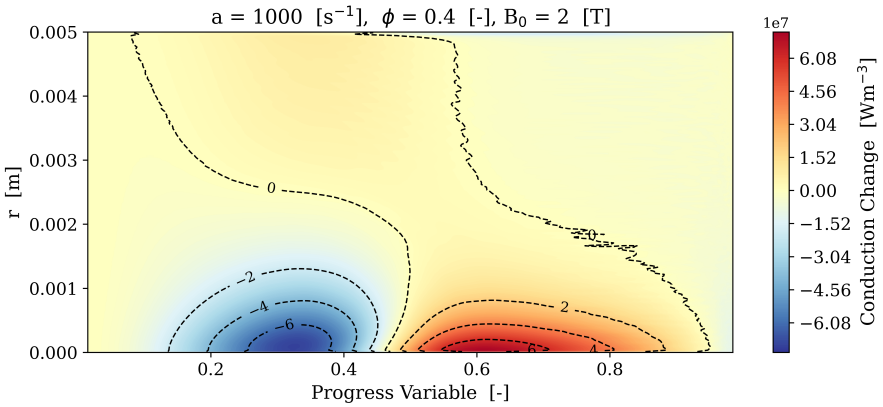

Figure 5.32: Change in conductive heat flux within the progress variable space due to a radially decreasing magnetic field. Conductive heat transfer emerges as the dominant mechanism responsible for the overall changes observed in the diffusive heat transfer pattern.

fraction influences the mixture fraction. These coefficients are given by:

$$\text{where,} \quad A_i = \left(\frac{n_{H,i} m_H}{m_i} - \frac{n_{O,i} m_O}{8 m_i} \right) / A_0$$

$$A_0 = 1 + \frac{0.23}{8}$$

$$A_1 = \frac{0.23/8}{A_0}$$

Table 5.1 summarises the values of these sensitivity coefficients for each relevant species in the hydrogen-air system. The mixture fraction Z shows a markedly high sensitivity to changes in the mass fraction of atomic hydrogen (H) and molecular hydrogen (H_2).

i	H_2	H	H_2O	OH	H_2O_2	HO_2	O	O_2	O_3
A_i	0.97	0.97	0.0	-0.057	-0.057	-0.088	-0.12	-0.12	-0.12

Table 5.1: Sensitivity coefficients A_i of the Bilger Mixture Fraction (Z) to changes in species mass fractions (Y_i).

Given the sensitivity of the mixture fraction to the species mass fractions, particularly those involving hydrogen atoms, a detailed examination of individual species distribution changes will be critical. Consequently, these species-level variations, their underlying causes, and implications for combustion chemistry and reaction kinetics will be explored comprehensively in the subsequent section dedicated to species transport mechanisms.

5.6. Species Transport Mechanisms

The species conservation equation governs the evolution of species mass fractions within reacting flows. Under transient conditions and the presence of magnetic fields, the governing equation for the mass fraction Y_i of species i is expressed as:

$$\rho \frac{\partial Y_i}{\partial t} = - \underbrace{\vec{\phi} \cdot \nabla Y_i}_{\text{Convective Transport}} - \underbrace{\nabla \cdot \vec{J_i}}_{\text{Diffusive Transport}} + \underbrace{\dot{\omega}_i}_{\text{Rate of Production}}$$

Here, convective transport is governed by the mass flux $Y_i \vec{\phi}$, diffusive transport by the diffusive flux $\vec{J_i}$, and the production rate $\dot{\omega}_i$ reflects chemical kinetics. At steady state, a balance among these competing mechanisms determines the spatial distribution of species within the flame.

Given the previously discussed sensitivity of the Bilger mixture fraction Z to variations in species mass fractions (see Table 5.1), Figure 5.50 and Figure 5.36 present the spatial distribution of changes in mass fractions for the species most significantly affecting Z: namely, O_2, O, H, and O_3.

Figure 5.50 reveals that the observed reduction in the Bilger mixture fraction Z primarily results from the combined effects of changes in O_2 and H mass fractions. Conversely, the species O exhibits a positive contribution

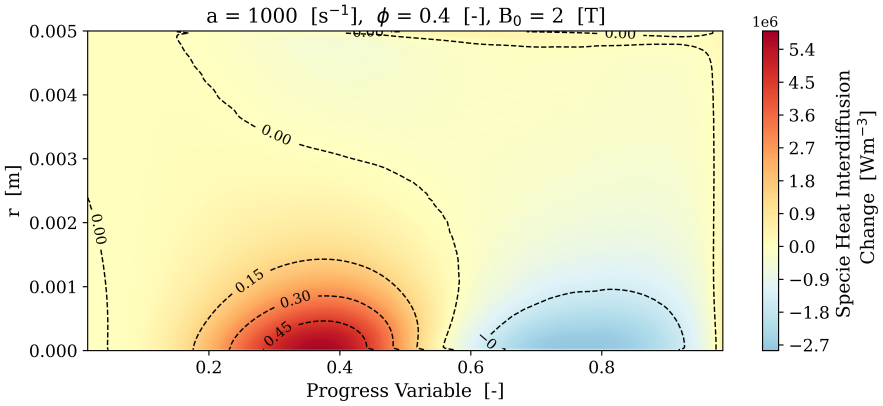

(a) Change in volumetric interdiffusive heat distribution due to species gradient-driven heat flux (q_{J_Y}) in the progress variable space.

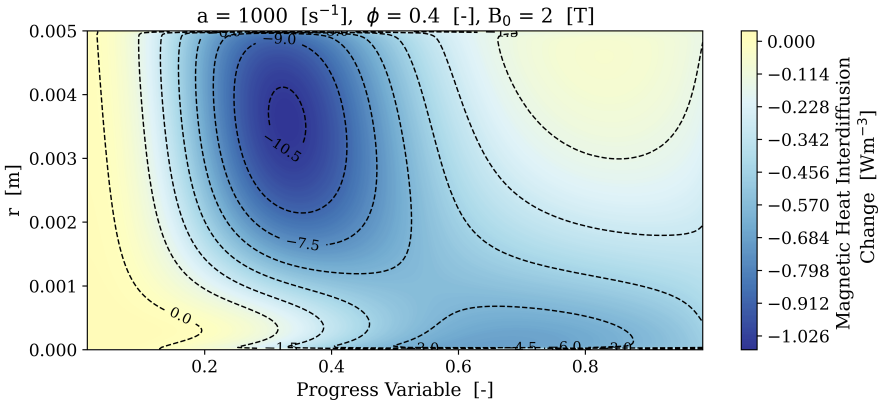

(b) Change in volumetric interdiffusive heat distribution due to magnetophoretic gradient-driven heat flux (q_{J_M}) in the progress variable space.

Figure 5.33: Comparative analysis between species gradient-driven diffusive heat flux and magnetophoretic gradient-driven diffusive heat flux. The magnetically induced heat diffusion is found to be negligible relative to the dominant species gradient-driven mechanism.

to Z. However, given that the sensitivity coefficient A_i for atomic hydrogen (H) is nearly an order of magnitude higher than that for atomic oxygen (O), and its mass fraction change is approximately an order of magnitude lower, their net contributions largely cancel each other out. Consequently, molecular oxygen (O_2) emerges as the most influential species governing the observed variation in mixture fraction.

Considering the significance of O_2 in determining local combustion characteristics, along with hydroxyl radical (OH), a key indicator of flame front location and combustion intensity, the subsequent sections will provide detailed mechanism analyses of these two species. The goal is to elucidate the underlying physical processes and interactions driving their respective mass fraction changes under magnetic field influences, thus offering deeper insights into the mechanisms governing flame dynamics and stability.

5.6.1. O_2 Field

The mass fraction of O_2 within the flame is governed by the interplay of three primary mechanisms: convection, diffusion, and chemical production or consumption (rate of production). Magnetic fields directly influence species distribution through magnetophoretic gradients $\vec{M}$, which drive magnetic diffusion fluxes $\vec{J}_M$.

Figure 5.36 illustrates the change in the O_2 mass fraction distribution resulting from the application of a radially decreasing magnetic field. It clearly shows a significant local increase in O_2 concentration near the axis within the reaction zone. This increase in O_2 mass fraction is identified as the principal reason behind the observed local reduction in the mixture fraction, subsequently affecting the reaction kinetics and the overall heat release rate.

To evaluate the relative significance of the contributing mechanisms, Figure 5.38 compares the magnitude of convective and diffusive transport contributions to the redistribution of O_2. Both mechanisms are observed to be significant and of comparable magnitude. Furthermore, Figure 5.37 depicts the change in the chemical

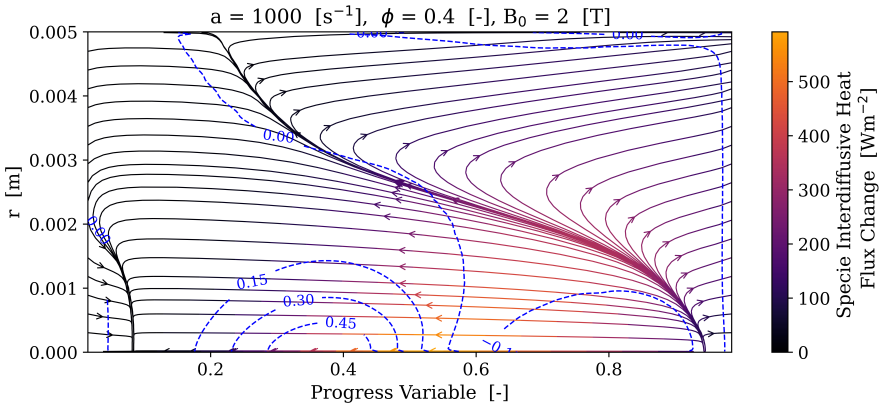

Figure 5.34: Change in the species gradient-driven interdiffusive heat flux pattern within the progress variable space under the influence of a radially decreasing magnetic field. The resulting patterns indicate a clear extraction of heat from the reaction zone, subsequently deposited into the preheat zone.

production rate of O_2, highlighting a substantial reduction in O_2 consumption rates near the flame axis within the reaction zone.

From these analyses, it is apparent that the reduced rate of O_2 consumption dominates near the reaction zone, causing the accumulation of oxygen. Conversely, convection acts to redistribute oxygen away from the reaction zone, particularly near the axis, while diffusion serves to moderate these gradients by smoothing out disparities between the convective and chemical mechanisms.

Convection

Figure 5.39 demonstrates the changes in the convective flux pattern of O_2 mass fraction induced by the magnetic field. The magnetic influence results in a pronounced outward transport of O_2 from the reaction zone along the flame axis, moving away from the stagnation point. This observation can be attributed to the altered axial velocity profile caused by the magnetic field: as the flame stabilises closer to regions of lower axial velocity, the net axial convective flux diminishes toward the stagnation point. Thus, the magnetic field effectively reduces the forward convective transport of O_2, manifesting as a reversed flux direction in the difference plots.

The following section will delve deeper into the diffusive transport mechanisms, specifically focusing on the role of magnetic diffusion fluxes and species gradient-driven diffusion, to further clarify the relative importance of these processes in determining the overall mass fraction distribution of O_2.

Diffusion

The diffusive transport of O_2 mass fraction in the presence of a magnetic field is governed by two primary components: the species-gradient-driven diffusion flux ($\vec{J}_Y$), resulting from concentration gradients, and the magnetically induced diffusion flux ($\vec{J}_M$), which arises from magnetophoretic effects. To evaluate the potential for a direct magnetic control strategy, it is essential to assess the relative strengths of these two fluxes.

Figure 5.40 compares the spatial changes in $\vec{J}_Y$ and $\vec{J}_M$ induced by the application of a radially decreasing magnetic field. The analysis indicates that the magnetic diffusion component is negligible, at least six orders of magnitude smaller than the species-gradient-driven flux. This establishes that magnetic diffusion plays no significant role in O_2 redistribution under the current configuration, rendering direct magnetic control via $\vec{J}_M$ infeasible.

The pattern of the species-gradient-driven diffusion flux ($\vec{J}_Y$) is shown in Figure 5.41. The results reveal a net outward transport of O_2 from the reaction zone toward the preheat zone, with an overall flux directed away from the flame axis. This behaviour closely mirrors the earlier observations from the interdiffusive heat transfer analysis (see Figure 5.34), reaffirming that O_2 is the dominant species contributing to enthalpy redistribution via interdiffusion.

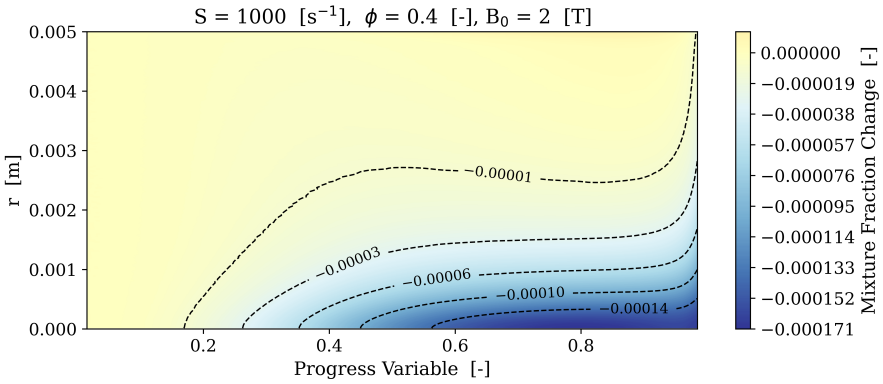

(a) Absolute Change

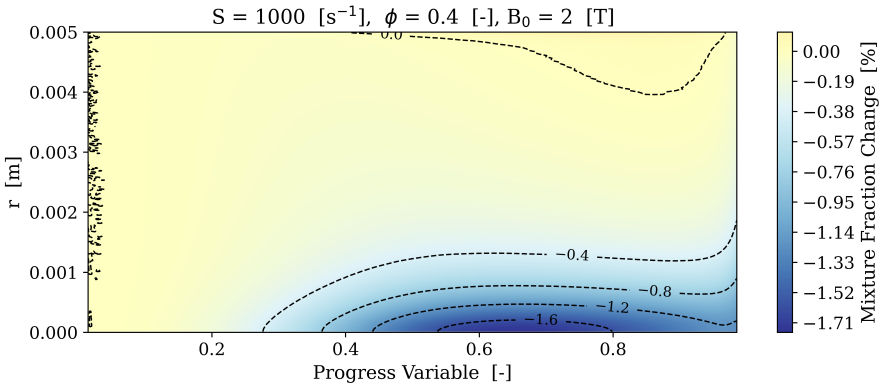

(b) Percentage Change

Figure 5.35: Spatial distribution of changes in the Bilger Mixture Fraction Z due to the influence of a radially decreasing magnetic field. A notable reduction of approximately 2% near the flame axis in the reaction zone is observed, directly correlating to the reduction in heat release rate.

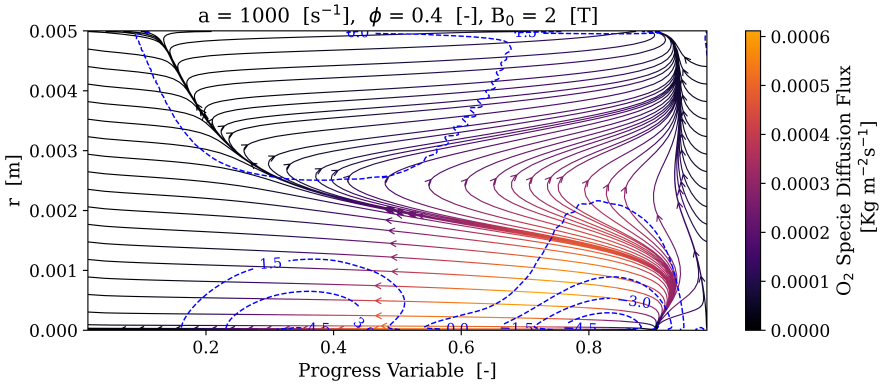

Figure 5.41: Change in the species-gradient-driven diffusion flux $\vec{J}_Y$ of O_2 in the progress variable space. The flux pattern demonstrates outward transport from the reaction zone and accumulation in the preheat zone, especially near the flame axis.

Although magnetic diffusion is weak in magnitude, its directionality still provides useful physical insights. Specifically, $\vec{J}_M$ aligns with the direction of the magnetophoretic gradient factor $\vec{M}_i$, which governs the magnetically induced drift. To confirm this alignment, Figure 5.42 compares the radial components of the magnetophoretic gradient factor and the corresponding magnetic acceleration for O_2.

The comparison confirms that $\vec{J}_M$ is directed along the magnetic acceleration vector $\vec{f}_i$, further validating its physical consistency. Although this alignment supports the theoretical behaviour of magnetic diffusion, the magnitude remains insufficient for any practical control effect in this configuration.

Having fully assessed the O_2 field and its governing transport mechanisms, the next subsection will analyse

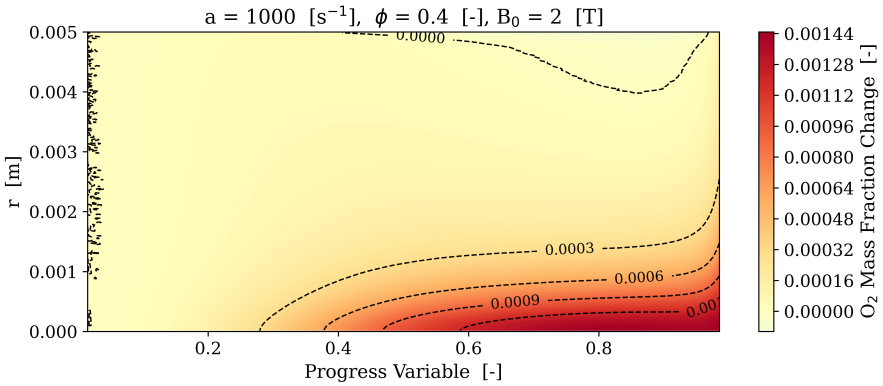

Figure 5.36: Spatial distribution of changes in the O_2 mass fraction in the progress variable space induced by a radially decreasing magnetic field.

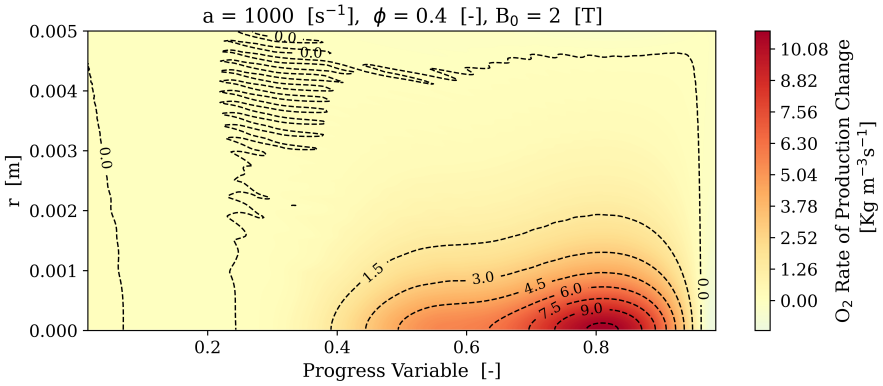

Figure 5.37: Change in the chemical production rate of O_2 mass fraction due to the influence of a radially decreasing magnetic field. A significant reduction in the rate of O_2 consumption near the flame axis in the reaction zone is evident.

the behaviour of the OH radical. As a key intermediate species and marker of the flame front, OH offers further insights into the combustion structure and how it responds to magnetic field-induced perturbations.

5.6.2. OH Field

Hydroxyl (OH) radicals play a key role in hydrogen combustion chemistry as active chain carriers and reliable markers of the reaction zone. In this configuration, the peak OH mass fraction typically coincides with the peak heat release rate, occurring around $C \approx 0.96$–0.97. Figure 5.43 illustrates the change in OH mass fraction under the influence of a radially decreasing magnetic field. A significant reduction is observed near the flame axis in the post-flame zone, particularly for $C \gtrsim 0.8$. This suggests that the local peak concentration of OH has decreased, thereby altering the flame structure and reaction intensity.

To understand this reduction, the governing transport equation for OH is examined, which includes three primary terms: chemical production, convection, and diffusion. The magnetic field directly contributes through the magnetically induced diffusion flux, but as with other species, this contribution is expected to be negligible in magnitude. These comparisons are demonstrated in Figure 5.44 and Figure 5.45.

Among the three contributing mechanisms, chemical reaction, convection, and diffusion, the rate of production ($\dot{\omega}$) emerges as the dominant factor influencing the change in OH mass fraction, particularly beyond $C > 0.8$, where a net depletion of OH is observed. This depletion occurs despite convection and diffusion attempting to replenish OH in that region, indicating that the suppressed chemical formation of OH overrides transport-based contributions. In the intermediate region ($C \approx 0.6$–0.8), diffusion plays a comparatively stronger role than convection, removing OH from the reaction zone even as both $\dot{\omega}$ and convection support its formation. Closer to the base of the reaction zone ($C < 0.6$), all three mechanisms exhibit comparable strengths with opposing trends, leading to a near-zero net change in OH mass fraction. This establishes $\dot{\omega}$ as the principal driver of observed reduction near the OH peak, while transport mechanisms contribute differently across spatial regions.

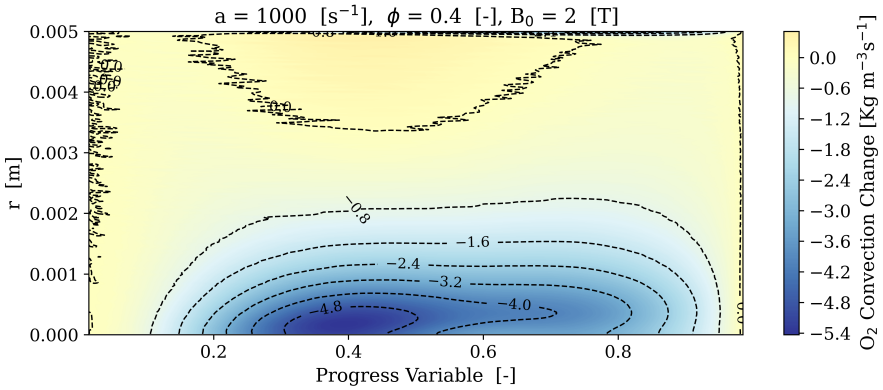

(a) Change due to convection.

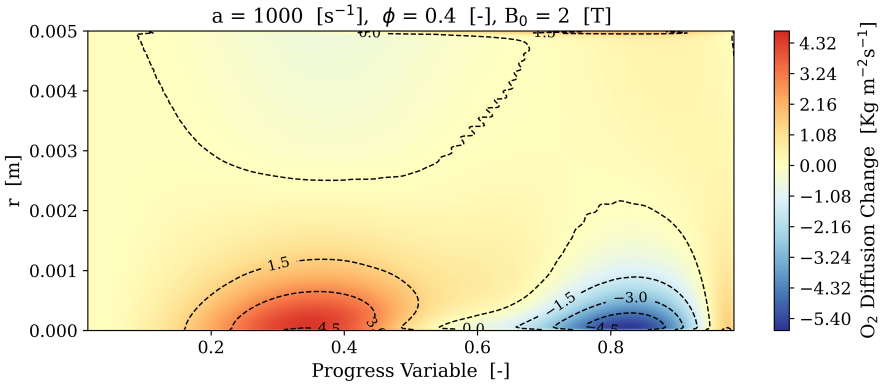

(b) Change due to diffusion.

Figure 5.38: Comparative analysis between transport-based redistribution mechanisms for O_2. Both convective and diffusive mechanisms exhibit significant and comparable magnitudes.

Rate of Production

The rate of production ($\dot{\omega}$) of OH reflects the net chemical source term arising from the competition between reactions that generate and consume OH. Figure 5.44 presents the change in OH production rate due to the application of a radially decreasing magnetic field.

The results exhibit alternating positive and negative regions within the reaction zone, primarily concentrated near the flame axis. These variations can be interpreted as follows: regions where OH was originally being produced (such as $C \approx 0.96$) now exhibit reduced production under magnetic influence, resulting in negative differences. Conversely, regions where OH was previously being consumed now show reduced consumption, reflected as positive values in the difference plot. This behaviour is consistent with the observed reduction in the rate of reaction near the axis, previously attributed to a local decrease in mixture fraction.

These $\dot{\omega}$ variations span across multiple segments of the flame front. Around $C \approx 0.4$–0.6, reduced OH consumption dominates, while $C \approx 0.6$–0.8 marks regions where OH is transported and consumed to sustain extended reaction zones. In the range $C \gtrsim 0.8$, the reduction in OH production is most pronounced and contributes directly to the observed decline in the peak mass fraction of OH.

Convection

The change in convective transport of OH mass fraction under the influence of a radially decreasing magnetic field is shown in Figure 5.46. The streamline plot of convective flux change overlaid with contour levels (blue-dashed lines) of convection difference reveals a clear redistribution pattern, predominantly near the axis and in the reaction zone.

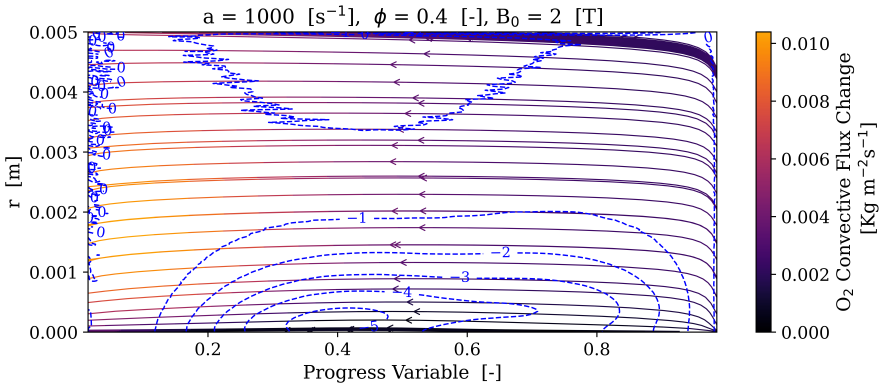

Figure 5.39: Change in the convective transport pattern of O_2 mass fraction within the progress variable space under a radially decreasing magnetic field. The pattern indicates a net reduction in forward axial convective transport near the flame axis.

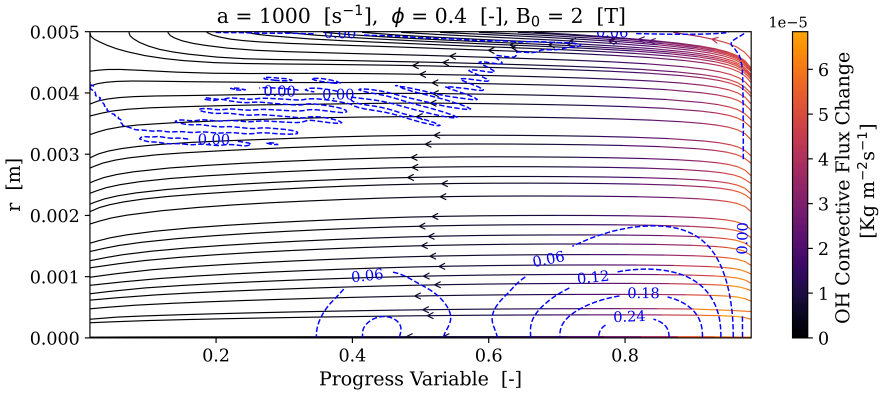

Figure 5.46: Change in the OH convective flux overlaid with the contours of change in convection (blue-dashed lines) in the progress variable space. Results show that the redistribution predominantly occurs near the axis between $C = 0.6$–0.9, where OH is convected from downstream (high C) regions back into the reaction zone.

The net pattern appears to suggest backwards convection, i.e., away from the stagnation point. However, this is an artefact of plotting the change in convective flux. In reality, the flame stabilises closer to regions of lower axial velocity due to magnetic influence, reducing the forward convective strength. As a result, the difference field mimics a reversed flux.

The observed flux pattern shows OH being convected from its peak concentration region ($C \approx 0.97$) back into lower-C regions, namely the reaction zone ($C \approx 0.6$–0.9), where it contributes to sustaining combustion. This net redistribution causes an apparent increase in OH mass fraction in the reaction zone, which counters the reduction caused by the chemical source term.

Importantly, the effect is strongest near the axis and weakens radially outward, reflecting the localisation of magnetic influence. Compared to O_2, the OH flux behaviour is inverted, which aligns with their chemical roles; OH being a product with high concentrations downstream, and O_2 a reactant available upstream. The same convection field thus transports them in opposing directions with respect to the flame structure.

This mechanism contributes positively to OH accumulation in the reaction zone but is ultimately dominated by diffusive transport, which plays a more significant role in shaping the OH distribution under magnetic influence. The following section explores this in detail.

Diffusion

The diffusive transport of OH is governed by two principal mechanisms: species-gradient-driven diffusion flux ($\vec{J}_Y$) and the magnetically induced diffusion flux ($\vec{J}_M$). A comparative analysis of their relative magnitudes is presented in Figure 5.47.

It is evident from Figure 5.47 that $\vec{J}_Y$ dominates the total diffusive behaviour, while $\vec{J}_M$ is negligible in magnitude, even within regions of high OH concentration. This confirms the earlier inference that magnetically induced diffusion is too weak to play a significant role in governing OH transport under the current configuration.

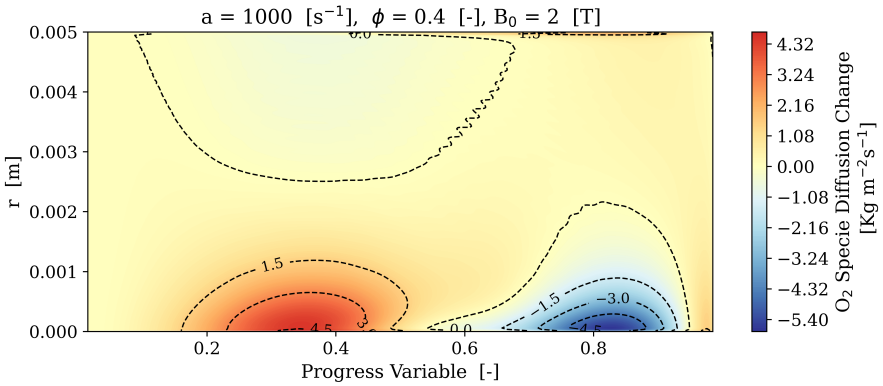

(a) Change in the species-gradient-driven diffusion flux $\vec{J}_Y$.

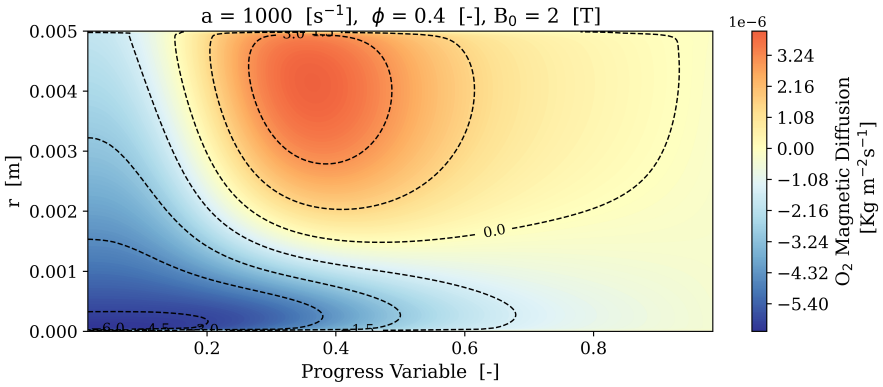

(b) Change in the magnetically induced diffusion flux $\vec{J}_M$.

Figure 5.40: Comparison of diffusion mechanisms affecting O_2 mass fraction. Magnetic diffusion is several orders of magnitude weaker than species-gradient-driven diffusion, indicating the absence of a viable direct magnetic control strategy.

The directionality and magnitude of the dominant diffusion flux $\vec{J}_Y$ are further illustrated in Figure 5.48. The streamlines and contours reveal a net forward and radially inward diffusive flux, transporting OH deeper into the reaction zone. However, the flux field is also marked by alternating regions of positive and negative diffusive contributions, which mirror the structure of the rate of production field (see Figure 5.44) in an opposing sense. This contrast supports the interpretation that diffusion acts to smooth out local imbalances caused by the rate of production and convective processes.

While magnetically induced diffusion is insignificant in magnitude, it is instructive to assess its directional alignment with the magnetic acceleration $\vec{f}_i$ and the magnetophoretic gradient factor $\vec{M}_i$. As shown in Figure 5.49, the radial component of $\vec{f}_i$ and $\vec{M}_i$ are directionally aligned—both pointing radially inward. However, spatial alignment is not observed. The magnetic acceleration $\vec{f}_i$ is concentrated predominantly in regions before $C = 0.5$, where the OH mass fraction is nearly zero. Consequently, $\vec{M}_i$, which depends on both the gradient of mass fraction and the magnetic acceleration, is negligible in those regions. Conversely, in regions with significant OH mass fraction ($C > 0.7$), the magnetic acceleration drops sharply, leading to negligible values of $\vec{M}_i$ even though concentration gradients are strong. This decoupling in spatial localisation further reinforces the minimal role of magnetic diffusion in OH transport.

The OH field shows that its mass fraction is most significantly influenced by chemical production, with strong secondary contributions from diffusion and, to a lesser extent, convection. The reduction in OH concentration near the axis is primarily driven by reduced rates of production, with diffusive transport further depleting OH from the reaction zone and convective effects working to redistribute it. Although the observed diffusive redistribution mimics a forward and radially inward pattern, it ultimately acts to diminish the sharp gradients introduced by reaction rate changes. Magnetic diffusion effects, in contrast, are negligible due to the spatial misalignment between the regions of significant magnetic acceleration and those of high OH concentration. Hence, no direct magnetic control strategy is feasible through diffusive manipulation of OH.

A side-by-side assessment of OH and O_2 mass fraction dynamics highlights two critical distinctions. First, the

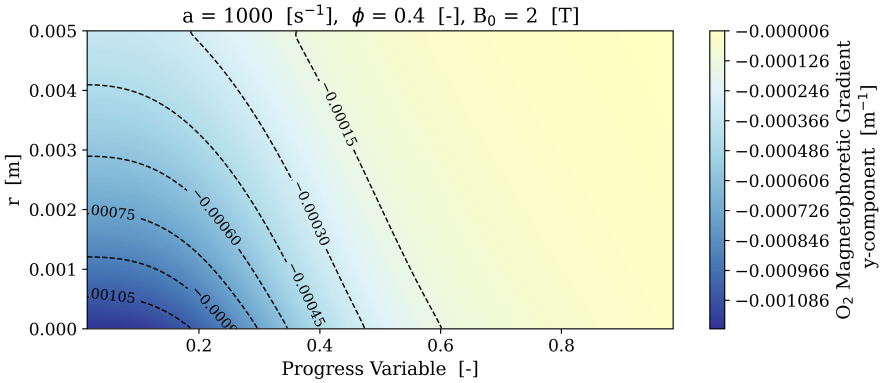

(a) Radial component of the magnetophoretic gradient factor $\vec{M}_i$ for O_2.

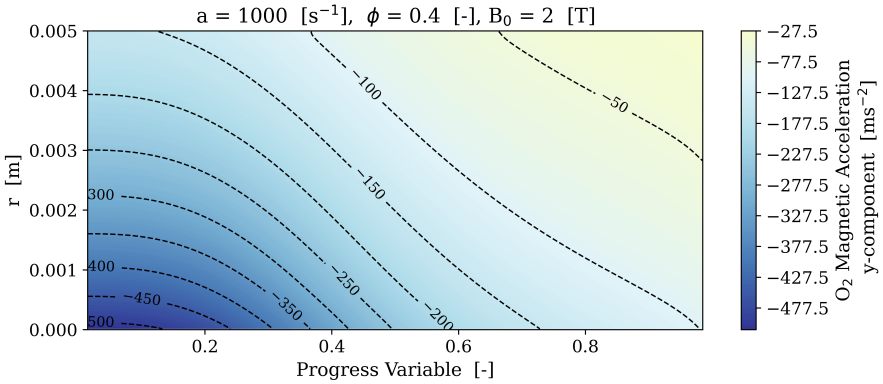

(b) Radial component of magnetic acceleration $\vec{f}_i$ for O_2.

Figure 5.42: Comparison of the directionality of the magnetophoretic gradient factor and magnetic acceleration for O_2. Both vectors point in the same direction, confirming that the magnetic diffusion flux $\vec{J}_M$ follows the direction of magnetic forcing.

dominant mechanism: while the rate of production primarily influences OH, O_2 is primarily altered by a reduction in convective supply into the reaction zone. This reflects their differing roles in the reaction mechanism, OH as a product radical peaking near the flame front, and O_2 as a reactant whose availability regulates flame intensity. Second, the response to magnetic field influence diverges: OH is transported inward by convection and diffusion after being produced, whereas O_2 is depleted due to reduced forward convection. Despite sharing similar directional convective flux patterns (due to global flow field changes), the consequences are species-specific, governed by where each species is most active within the flame structure.

Given that both OH and O_2 are significantly affected by convective redistribution, and considering that convection was altered indirectly due to magnetic forces acting on the flow field, it becomes imperative to investigate the momentum equation next. Understanding how magnetic fields modify the velocity field, streamline topology, and pressure gradients is crucial to evaluating whether convection can be harnessed as an effective indirect magnetic control strategy. The next section, Momentum Transport Mechanisms, will therefore dissect these interactions in detail.

5.7. Momentum Transport Mechanisms

The Navier–Stokes equations for incompressible flows govern the momentum transport in low-Mach-number reacting flows. When the influence of magnetic fields is included, the transient momentum equation can be expressed as

$$\rho\frac{\partial\vec{u}}{\partial t} = -(\vec{\phi}\cdot\nabla)\vec{u} - \nabla p + \nabla\cdot\tau + \underbrace{\rho\sum_i Y_i\vec{f}_i}_{\text{Weighted Body Force}}$$

where $\vec{\phi} = \rho\vec{u}$ is the mass flux vector, τ denotes the viscous stress tensor, and $\vec{f}_i$ represents the body force per unit mass acting on species i. The final term on the right-hand side captures the cumulative magnetic body force

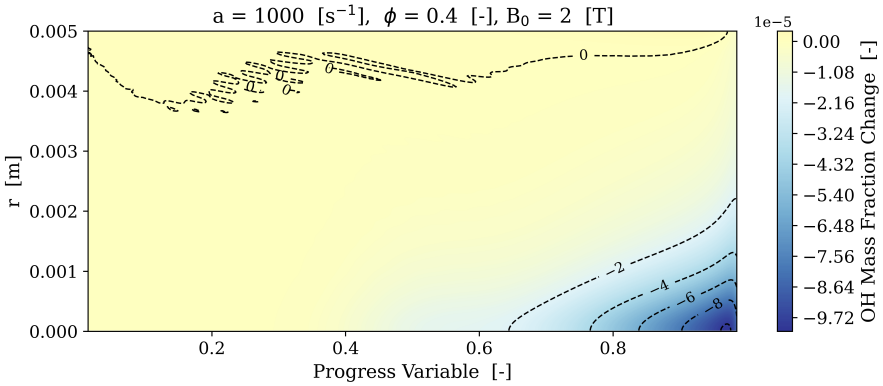

Figure 5.43: Reduction in OH mass fraction near the flame axis in the reaction zone ($C \approx 0.96$–0.97) under a radially decreasing magnetic field, indicating local weakening of reaction intensity.

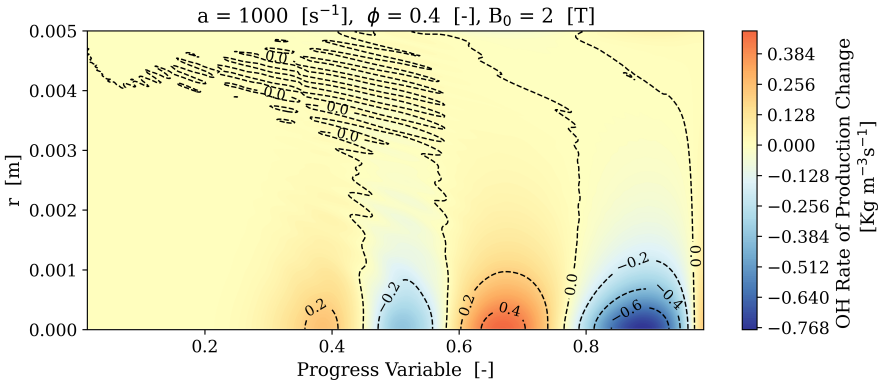

Figure 5.44: Change in the chemical production rate of OH mass fraction due to the influence of a radially decreasing magnetic field. Results indicate a reduction in both OH production and consumption near the axis, corresponding to a diminished overall reaction intensity.

contribution weighted by species mass fractions Y_i.

In the present configuration, the momentum transport is modulated by a radially decreasing magnetic field with a peak intensity of 2 T. The resulting change in the mass flux pattern is illustrated in Figure 5.51, where the contours of progress variable C ($C = 0.05, 0.5, 0.95$) mark the flame position. The induced modification is driven by the distribution of the weighted magnetic body force shown in Figure 5.54a, which indicates that the effective region of magnetic influence is confined primarily upstream of the $C = 0.5$ isoline.

The changes in the mass flux field (Figure 5.51) reveal a radially inward convective motion upstream of the reaction zone, counterbalanced by a radially outward motion downstream of the preheat zone where the magnetic influence is negligible. This redistribution of the convective flux pattern is a direct consequence of the magnetic body force and plays a key role in locally enriching the concentration of abundant species near the flame axis, potentially influencing reaction rates and local flame curvature.

When the mass flux change is represented in the progress variable space (Figure 5.52), an apparent upstream-directed induction is observed. However, this is not a true reversal of the convective flow but rather a relative change caused by the flame anchoring itself closer to the stagnation plane. This upstream stabilisation occurs in a region of lower axial velocity, which reduces the net downstream transport compared to the baseline case and manifests as an apparent backflow in the difference plots.

It is important to note that the momentum transport dynamics in reacting flows are inherently non-linear due to the coupled nature of the Navier–Stokes equations with combustion source terms. As such, a steady-state analysis is insufficient to establish a definitive causality structure for the observed changes in the convective field. Consequently, a detailed mechanism-based breakdown of these effects is not presented in this section; instead, the discussion is limited to a qualitative interpretation of the results. The subsequent section will focus on a parametric study, evaluating how the mechanisms outlined in previous sections respond to variations in the applied strain rate and the equivalence ratio.

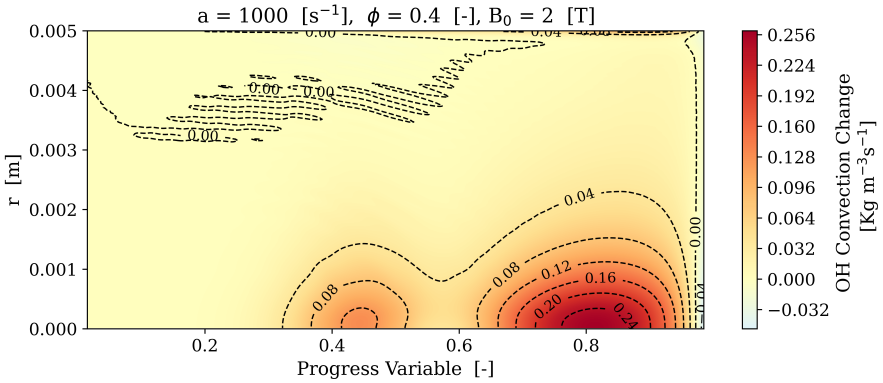

(a) Change due to convection.

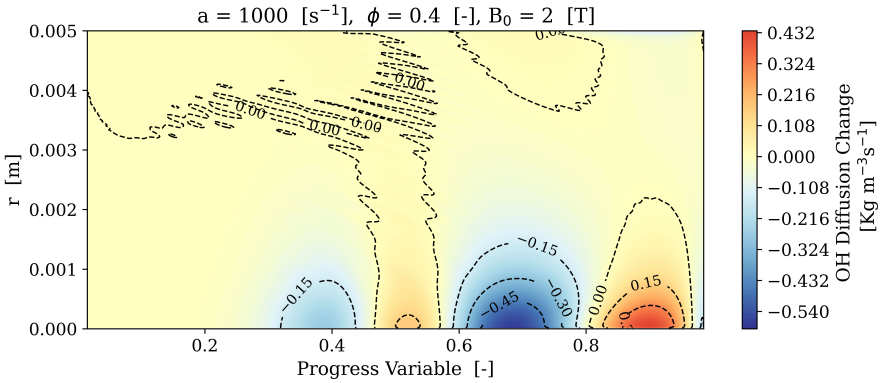

(b) Change due to diffusion.

Figure 5.45: Comparative analysis between transport-based redistribution mechanisms for OH. Both convective and diffusive mechanisms exhibit significant and comparable magnitudes.

5.8. Parametric Study

The effectiveness of magnetic field-based flame control is highly sensitive to the underlying flame conditions and governing flow parameters. To comprehensively assess the robustness and feasibility of magnetic control strategies, a parametric study is conducted by systematically varying three key parameters: strain rate, equivalence ratio, and magnetic field configuration. Each parameter influences the interplay between transport processes, chemical kinetics, and electromagnetic interactions in unique ways. This section aims to quantify and compare the nature and extent of magnetic field influence under different parametric regimes, identifying trends that either favour or inhibit control effectiveness. Ultimately, the goal is to isolate conditions under which magnetic effects, either direct or indirect, are enhanced and to determine which combinations offer the most promise for practical flame control applications.

5.8.1. Effect of Strain

Strain rate is a fundamental parameter that governs flame behaviour, sensitivity to transport processes, and responsiveness to external forcing mechanisms such as magnetic fields. In lean hydrogen-air flames, which exhibit Lewis numbers less than unity ($Le < 1$), increasing strain enhances preferential diffusion and steepens temperature gradients, often elevating the peak flame temperature. Since the magnetic body force $\vec{f_i}$ is inversely dependent on temperature, this trend should theoretically reduce the strength of the Kelvin force and, consequently, diminish the influence of magnetic fields on the flame.

This anticipated behaviour is qualitatively validated in Figure 5.53, which presents the velocity field and flame front (via iso-contours of the progress variable C) for a strain rate of $a = 2000\ \mathrm{s}^{-1}$. Compared to the lower strain case of $a = 1000\ \mathrm{s}^{-1}$, the flame shows minimal deformation and shift under magnetic influence, indicating a suppressed magnetic response at higher strain.

To quantify the influence of strain on magnetic forcing, the y-component of the weighted body force momentum $\rho \sum_i Y_i f_{i,y}$ is compared at $a = 1000$ and $2000\ \mathrm{s}^{-1}$. Figure 5.54 shows the absolute fields at both strain rates.

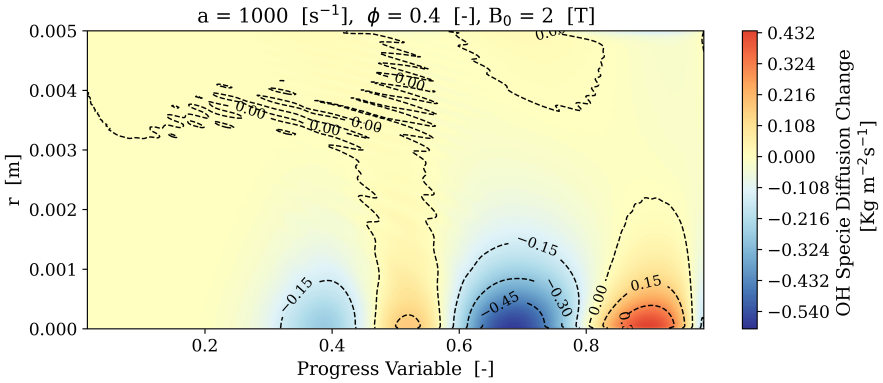

(a) Change in the species-gradient-driven diffusion flux $\vec{J}_Y$.

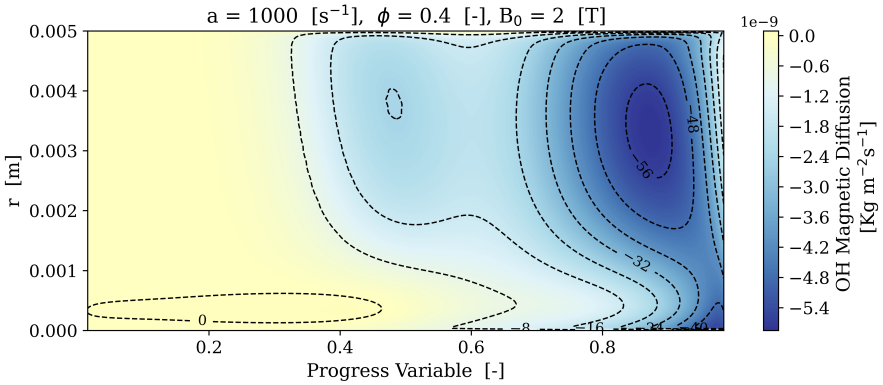

(b) Change in the magnetically induced diffusion flux $\vec{J}_M$.

Figure 5.47: Comparison of diffusion mechanisms affecting OH mass fraction. Magnetic diffusion is several orders of magnitude weaker (approximately 9 orders) than species-gradient-driven diffusion, eliminating the possibility of a viable direct magnetic control strategy.

Although subtle, there is a visible reduction in the intensity of the force near the axis at higher strain. This trend is made explicit in Figure 5.55, which plots the difference in magnitude of the y-component of the weighted body force. As expected, the result clearly demonstrates a net reduction in force magnitude at higher strain, especially near the core flame region (progress variable C between 0.2 and 0.4).

This reduction aligns with the inverse relationship between $\vec{f}_i$ and temperature, yet Figure 5.54 shows that the absolute body-force distribution remains essentially unchanged across most of the domain outside the flame. Two immediate questions, therefore, arise:

1. Why does the magnetic body force remain essentially unaffected in the regions outside the flame, even when the global strain is doubled?
2. Why does the overall magnetic influence on the velocity field and flame structure still diminish if the external body-force field itself is largely unchanged?

Across most of the domain, the weighted body-force field is governed by the fresh-gas conditions that prevail upstream of the reaction zone ($C < 0.5$). In this preheat region, the temperature and density fields remain virtually identical across both strain rates. As a result, the Kelvin-type force, given by

$$\vec{f} \propto \frac{\nabla(\vec{B}^2)}{T}$$

and consequently, the weighted body-force term exhibits negligible variation. Downstream of $C \approx 0.5$, where temperature rises sharply, the $1/T$ dependence significantly attenuates the magnitude of the magnetic force. In this regime, the force is already too weak to exert any meaningful influence on the flow, and further reduction due to higher strain becomes inconsequential. As a result, the difference field between the two cases shows minimal variation outside the flame, consistent with the behaviour observed in Figure 5.54.

Despite minimal variation in the body force, the overall influence of magnetic fields diminishes under high-strain conditions. This reduction arises from two primary factors: a relative decrease in the ratio of magnetic to

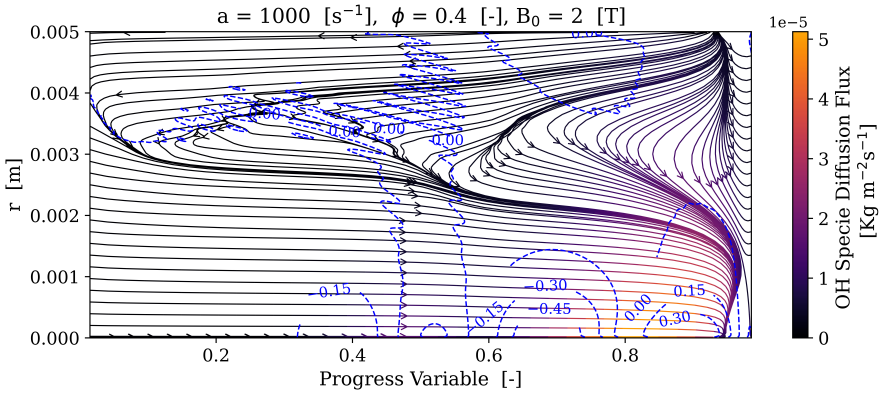

Figure 5.48: Change in the species-gradient-driven diffusion flux $\vec{J}_Y$ of OH in the progress variable space. A net forward and inward redistribution of OH mass fraction is observed, with alternating positive and negative contributions that counteract rate-of-production fluctuations.

inertial forces, and a shortened duration of magnetic field interaction. As applied strain is increased by elevating the flow velocity, the associated inertial forces grow in magnitude, while the magnetic forces remain effectively constant. Consequently, the influence of the magnetic field becomes less pronounced. This observation highlights a disparity in the Stuart number, a key similarity parameter governing magnetohydrodynamic behaviour, which must be carefully considered when designing parametric studies involving strain variation under the influence of a magnetic field.

5.8.2. Effect of Equivalence Ratio

The equivalence ratio (ϕ) plays a critical role in determining both the chemical and physical response of hydrogen flames to magnetic fields. Variations in ϕ influence radical concentrations, flame stabilisation location, and the relative magnitude of magnetic to inertial forces. Understanding these dependencies is essential for assessing the feasibility and effectiveness of magnetic control strategies across operating regimes.

As shown in Figure 5.56, the application of a radially decreasing magnetic field at $\phi = 0.8$ produces only minimal changes in the flow field and flame structure. Two primary factors contribute to this reduced influence. First, at higher nominal equivalence ratios, the oxygen concentration is inherently lower. Since oxygen is the dominant contributor to the magnetic body force, its reduction results in a decrease of at least 20 $\mathrm{N/m^3}$ in the net body force (Figure 5.57). Second, the higher fuel concentration at $\phi = 0.8$ increases the consumption speed, causing the flame to stabilise further upstream relative to the stagnation plane. This upstream shift reduces the spatial extent over which the magnetic field interacts with the flame, thereby shortening the effective magnetic time of influence.

The combined reduction in both body force magnitude and interaction time leads to a diminished capacity for magnetic modulation of flame dynamics under these richer operating conditions.

5.9. Discussion of Key Results

A synthesis of the principal outcomes of the results chapter is presented for lean H_2/air counterflow flames subjected to a radially decreasing magnetic field. Interpretation is provided in the progress variable space using the progress-variable bands *preheat* ($C < 0.7$) and *reaction* ($0.7 \leq C \leq 0.95$). Rather than re-listing figures, the section integrates evidence across progress variable space kinematics (axial and radial redistribution), the stretch decomposition (tangential strain versus curvature-induced stretch), and structural metrics (local-normal thermal thickness reported via distribution-based representatives such as the KDE mode). The earlier analyses of direct and indirect control strategies and the parametric study (strain rate a, equivalence ratio ϕ, and field topology) are consolidated to explain the observed balances and their physical causes. The seven research questions are addressed explicitly, with effect sizes reported where available, to identify the dominant mechanisms by which magnetic forcing influences premixed flames. Finally, robustness and limitations (choice of representatives, local versus global metrics, scope of validity, and modelling assumptions) are delineated, and implications are articulated for control and the reporting of statistics in curved-flame configurations. The next subsection presents the *Key takeaways*, providing a concise statement of the main findings that anchor the detailed discussion that follows.

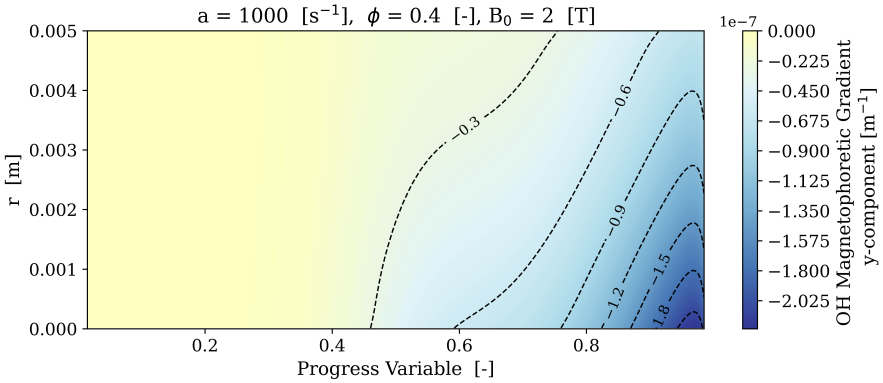

(a) Radial component of the magnetophoretic gradient factor $\vec{M}_y$.

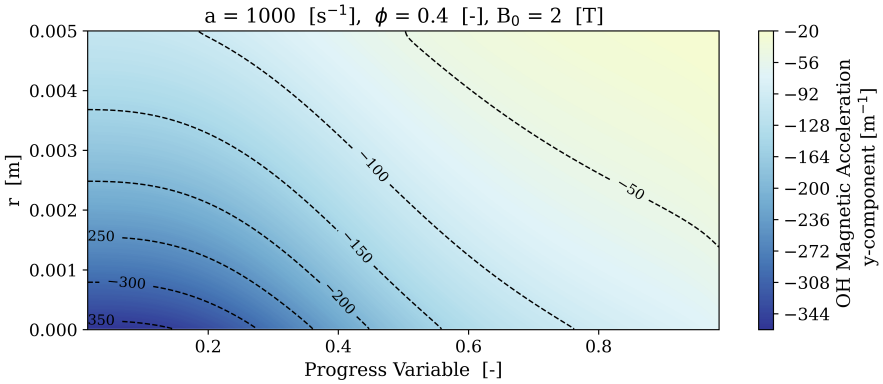

(b) Radial component of the magnetic acceleration $\vec{f}_y$.

Figure 5.49: Assessment of the magnetic field's direct effect on OH diffusion. While $\vec{M}_y$ and $\vec{f}_y$ are directionally aligned, they are spatially decoupled, resulting in negligible effective magnetic diffusion.

5.9.1. Key Takeaways

This subsection summarises the principal empirical findings for lean H_2/air counterflow flames subjected to a radially decreasing magnetic field. Each item is stated concisely with its observed magnitude; explanatory mechanisms are developed in the subsequent *Integrated Interpretation* subsection.

1. **Representative thermal thickness is effectively unchanged** (KDE–mode shift ≤ 0.03 %).
   Rationale: The peak of the local–normal thickness distribution remains essentially stationary between 0 T and 2 T. Although the distribution is mildly skewed, its highest–density region does not move appreciably, indicating no material change in the modal thermal gradient.
2. **Total kinematic stretch decreases near the axis and in the preheat layers by ∼5-13 %, while remaining positive overall.**
   Rationale: The mapped quantity is the *relative change* in κ; the absolute total stretch remains positive across the domain. The strongest reductions occur near the axis and within $C < 0.7$.
3. **Tangential strain exhibits a two–regime response:** a decrease of approximately 5-8 % in the preheat zone and an increase of approximately 6-8 % in the reaction zone.
   Rationale: Opposite–sign changes are separated by the progress variable band, with the minimum centred at low C near the axis and the maximum sustained for $C \gtrsim 0.5$ through the reaction layers.
4. **The curvature–induced contribution changes sign near the axis and dominates the *change* in total stretch.**
   Rationale: With the front concave to the reactants, $S_D(\nabla \cdot \hat{n})$ becomes negative; its *relative* change exceeds 100 % (sign reversal), outweighing the modest rise in a_t where present and thereby driving the net reduction in κ.
5. **Velocity–field redistribution in the flame–attached frame is two–regime.**
   Rationale: The axial component weakens broadly, whereas the radial velocity weakens for low C near

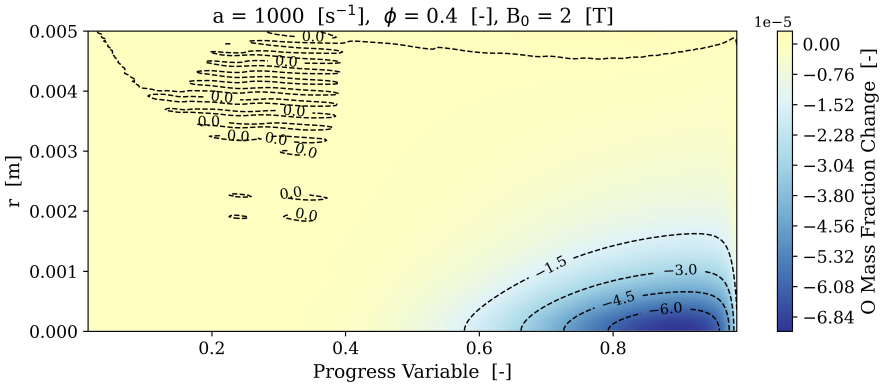

(a) Mass Fraction change of O in progress variable space.

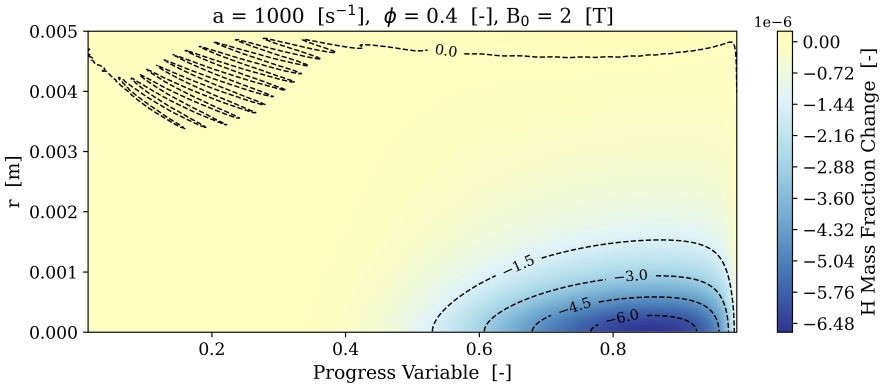

(b) Mass Fraction change of H in progress variable space.

Figure 5.50: Changes in the mass fractions of species exhibiting the greatest sensitivity to the mixture fraction Z.

the axis and strengthens for $C \gtrsim 0.5$ and across the reaction layers. This spatial pattern aligns with the locations of the observed decreases and increases in a_t.

6. **Field topology matters empirically:** the radially decreasing configuration exhibits the clearest, geometry–coupled control signature in this set–up.
   Rationale: Among the tested topologies, it yields the most coherent and repeatable patterns in the κ, a_t, and curvature maps, particularly near the axis and across the reaction layers.
7. **Parametric trends:** magnetic influence weakens as strain rate increases and as the mixture becomes richer.
   Rationale: Higher a shortens the effective influence time and raises inertia; larger ϕ reduces oxidiser leverage and shifts the flame upstream, shortening the spatial region over which forcing acts.
8. **Instability–relevant indicators show local tendencies consistent with stabilisation in curvature controlled modes.**
   Rationale: The strongest reduction of κ occurs in preheat near the axis, where curvature effects are most influential, while global scalar metrics remain largely unchanged or ambiguous at high stretch.

5.9.2. Integrated Interpretation

This subsection provides a coherent interpretation of the empirical findings summarised in *Key Takeaways*. The discussion links the observed fields and statistics to their governing mechanisms by examining: (i) velocity redistribution in the progress variable space; (ii) the kinematic-stretch balance written as $\kappa = a_t + S_D(\nabla \cdot \hat{n})$; and (iii) the behaviour of the local-normal thermal-thickness distribution. For completeness, elements that might otherwise appear in a separate synthesis, namely the roles of control strategy, the parametric dependence on strain rate a and equivalence ratio ϕ, and the influence of field topology, are incorporated here so that mechanisms and cross-section connections are treated within a single, consistent narrative.

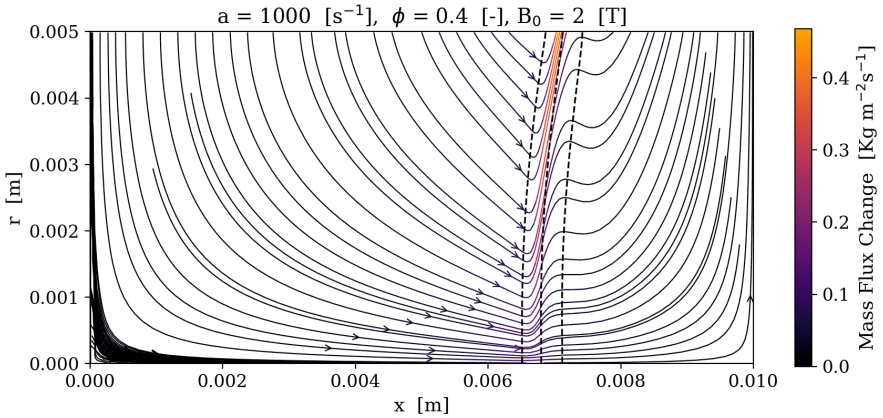

Figure 5.51: Change in the mass flux streamlines influenced by a radially decreasing magnetic field, overlaid with progress variable contours at $C = 0.05, 0.5, 0.95$ (black dashed lines). A radially inward flux is induced upstream of the flame, with a corresponding outward flux downstream of the preheat zone to conserve mass.

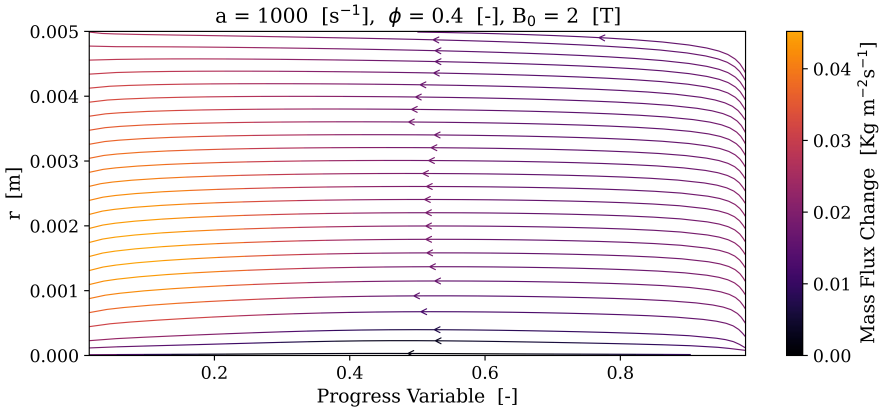

Figure 5.52: Change in the mass flux streamlines in the progress variable space. The apparent upstream induction is a result of the flame stabilising closer to the stagnation plane in a region of lower axial velocity, thereby reducing downstream transport relative to the baseline case.

Velocity–field redistribution in the progress variable space

In the radially decreasing configuration, the Kelvin body force is strongest upstream near the axis, where the gas remains relatively cold, and it draws mass inwards. Mass conservation subsequently redirects this inflow into the radial direction downstream, where thermal expansion is stronger and magnetic forcing is weaker. In the flame–attached frame, the flame stabilises within a region of reduced axial velocity. The resulting velocity field displays a two–regime behaviour: the axial component decreases across the entire domain, while the radial component decreases near the axis in the preheat region ($C < 0.7$) but increases for $C \gtrsim 0.5$ throughout the reaction layers. The stagnation plane itself undergoes only a minor displacement; the dominant adjustment is therefore a redistribution of momentum from the axial to the radial direction, rather than a complete rearrangement of the stagnation structure. This redistribution establishes the spatial pattern of tangential strain: it decreases in the preheat layers, where the radial component weakens, and increases in the reaction layers, where the radial component strengthens.

Kinematic Stretch Rate decomposition

The total kinematic stretch is written as $\kappa = a_t + S_D(\nabla \cdot \hat{n})$. Near the axis, the flame front becomes concave to the reactants, so $\nabla \cdot \hat{n} < 0$ and the curvature–induced term contributes negatively. Its relative change exceeds 100 % (a sign reversal) and, as a result, it dominates the *change* in κ even though a_t remains larger in absolute magnitude overall. Consequently, κ is reduced by approximately 5-13 % in the preheat layers and the near-axis region, while remaining positive in absolute terms. In the reaction layers, the strengthened radial component of velocity increases a_t by about 6-8 %, partially offsetting the negative curvature contribution locally; however,

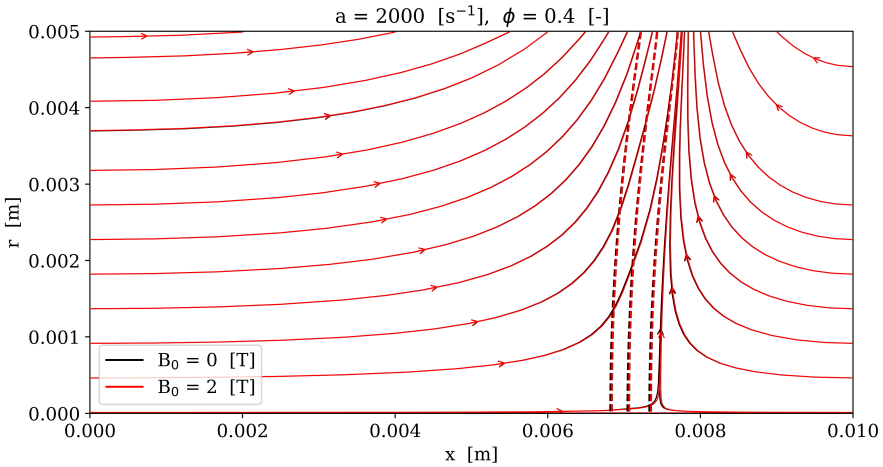

Figure 5.53: Velocity streamlines and flame contours at $a = 2000\ \mathrm{s}^{-1}$ for $\phi = 0.4$ in a radially decreasing magnetic field. Iso-contours of progress variable $C = 0.05, 0.5, 0.95$ mark the flame position. Minimal deviation in both flow and flame structure suggests reduced magnetic control at elevated strain.

this compensation is insufficient to overturn the curvature-driven reduction established in the preheat region.

Thermal Flame Thickness

The local–normal thermal thickness exhibits a mildly skewed distribution over the curved flame front. To obtain a robust single–value descriptor, a distribution–aware representative is employed, thereby avoiding sensitivity to tails and to histogram binning. The kernel–density (KDE) mode, reported alongside the median and a 10 % trimmed mean, changes by no more than 0.03 % between 0 T and 2 T. This negligible shift indicates that the modal thermal gradient is essentially unchanged, consistent with the interpretation that magnetic forcing primarily redistributes the kinematic–stretch balance and the velocity field rather than altering the most probable thermal structure.

Lewis–number and Fickian diffusion effects

In premixed flames, the reactants form a single stream. Only oxygen is directly subject to the magnetic body force, yet the entire mixture must be accelerated. Consequently, purely convective forcing cannot generate differential responses within the stream, and the increased effective inertia reduces the relative strength of the forcing.

Observable composition changes arise only when non–unity Lewis numbers and Fickian diffusion are active. The convective fluxes drive species accumulation towards the axis, and this transport is opposed by diffusion fluxes induced by the locally increased concentrations. Because hydrogen is significantly more diffusive than oxygen, a comparatively small accumulation of hydrogen is sufficient to counter the convective effects. Oxygen, by contrast, requires a substantially higher mass fraction accumulation to balance convection. This asymmetry results in oxygen enrichment near the axis. Under such conditions, the upstream oxygen accumulation alters the local mixture fraction, suppresses heat release and temperature near the axis, and decreases both OH production in the post–peak region and OH consumption around $C \sim 0.7$. When $Le = 1$, no such accumulation occurs, confirming that preferential diffusion is the operative pathway in these premixed conditions and that it is weaker than the convection–dominated mechanisms typical of diffusion flames.

Direct versus indirect control strategies

In this configuration, *direct* magnetic mechanisms comprise the species magnetic–diffusion fluxes, the magnetic body–force work in the energy equation, and the heat interdiffusion induced by the magnetic–diffusion fluxes. At the field strengths considered, all three contributions are intrinsically weak and their net effect is negligible; they do not provide a practical control handle in premixed counterflow.

Effective manipulation, therefore, relies on an *indirect* route in which magnetically induced changes to the carrier–flow field act in concert with Fickian diffusion. Because the mixture is premixed, convection alone moves all species similarly and cannot create differential composition changes. A measurable response arises only when the weak, geometry–dependent convective redistribution (set by the field topology and the near–stagnation kinematics) couples with non–unity Lewis numbers, so that Fickian diffusion responds to the convectively induced

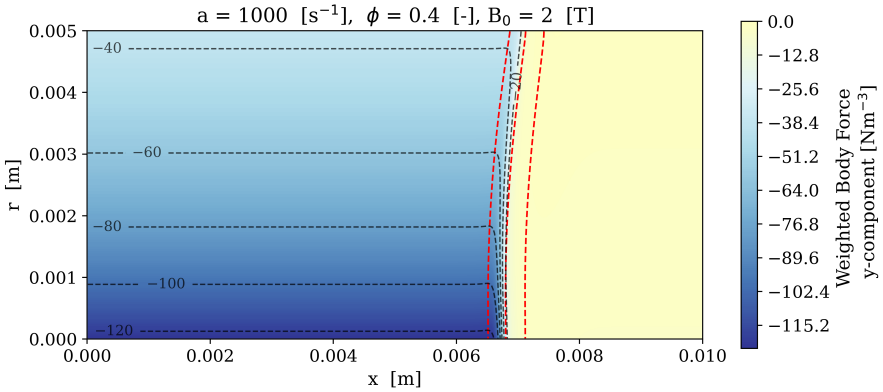

(a) Spatial distribution of the y-component of the weighted body force for $a = 1000\ \mathrm{s}^{-1}$.

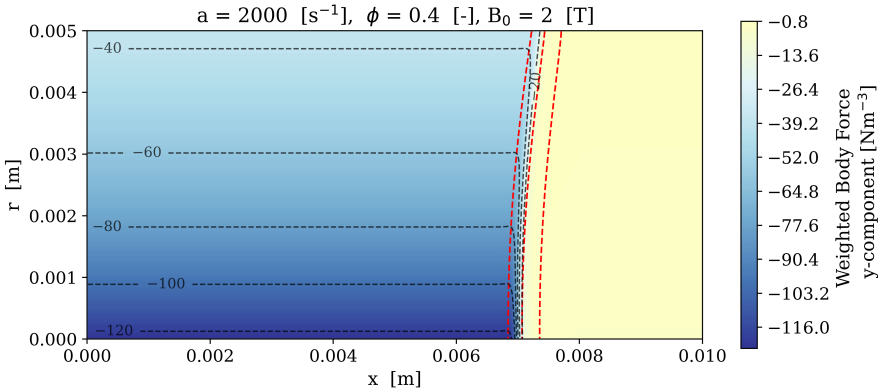

(b) Spatial distribution of the y-component of the weighted body force for $a = 2000\ \mathrm{s}^{-1}$.

Figure 5.54: Spatial distribution of the weighted body force $\rho \sum_i Y_i \vec{f}_i$ in the domain under radially decreasing magnetic fields at two different strain rates. Results show that the overall magnitude remains nearly unchanged despite the increase in strain.

concentration gradients. In practice, this coupling produces oxygen enrichment upstream near the axis, modifies the local mixture fraction and temperature field, and thereby provides limited but reproducible leverage over flame position and propagation characteristics. The degree of control is constrained by regime and topology: it depends on the available influence time, the alignment of the forcing with the dominant transport directions, and the presence of preferential diffusion.

Parametric Trends

Increasing the applied strain rate a raises the characteristic inertia of the incoming streams and shortens the magnetic influence time, thereby weakening the signatures of magnetic forcing in the upstream region where the body force is strongest. Downstream of $C \approx 0.5$, the forcing is intrinsically weaker owing to higher temperatures and thermal expansion; consequently, larger a further diminishes the relative impact of the preferential diffusion pathway in this part of the field. The net effect is a systematic attenuation of magnetically induced redistribution as a increases, with reduced scope for composition or kinematic changes to develop within the flame–attached frame.

Increasing the equivalence ratio ϕ reduces the oxidiser fraction in the reactants and shifts the flame upstream, which shortens the spatial window over which magnetic forcing can act. The reduction in available oxygen also lowers the leverage of oxygen–specific forcing relative to the inertia of the premixed stream, further limiting differential responses. Taken together, these trends provide a consistent explanation for the observed weakening of magnetic influence at higher strain rates and richer mixtures: the effective alignment of forcing with transport pathways is degraded, and the time and length scales available for preferential diffusion–mediated responses are curtailed.

Field Topology Dependence

Field topology determines how the magnetic body force aligns with the dominant transport pathways and with the counterflow geometry, thereby setting the degree of leverage available for control. In the radially decreasing

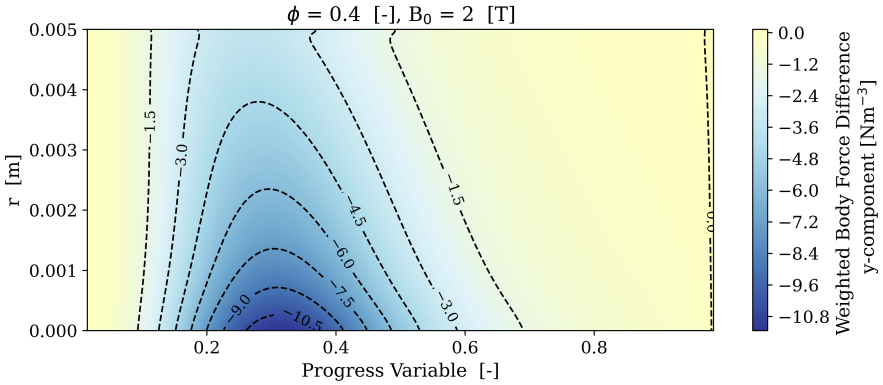

Figure 5.55: Difference in the magnitude of the y-component of weighted body force between $a = 2000\ \mathrm{s}^{-1}$ and $a = 1000\ \mathrm{s}^{-1}$, plotted in the progress variable space. Results show a net reduction in body force strength at higher strain, particularly along the flame axis between $C = 0.2$ and $C = 0.4$.

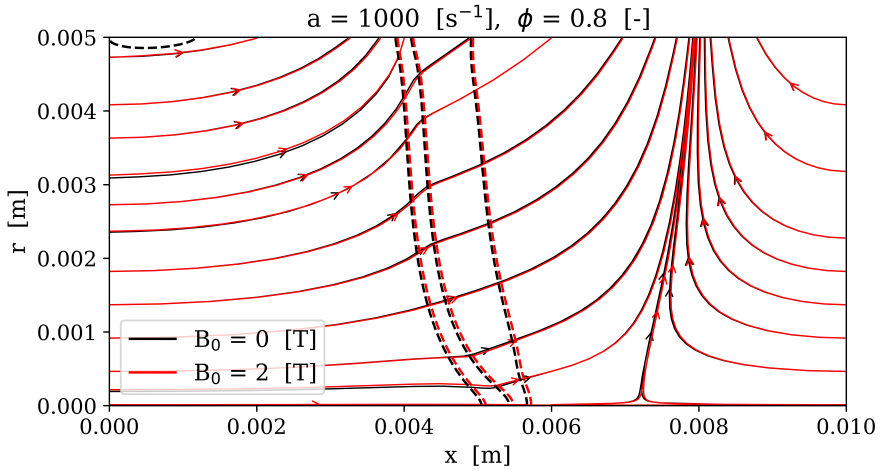

Figure 5.56: Velocity streamlines and flame contours at $a = 1000\ \mathrm{s}^{-1}$ for $\phi = 0.8$ in a radially decreasing magnetic field. Iso-contours of progress variable $C = 0.05, 0.5, 0.95$ mark the flame position. Minimal deviation in both flow and flame structure suggests reduced magnetic control at high equivalence ratios.

configuration, the body force strengthens towards the axis upstream of the flame and acts where the gas is colder; this alignment focuses the response near the axis and within the preheat layers. In the flame–attached frame, the axial component of velocity decreases broadly, while the radial component decreases near the axis for low C and increases for $C \gtrsim 0.5$ across the reaction layers. The resulting kinematic and structural responses are spatially coherent and repeatable in this geometry: curvature near the axis tends to become concave to the reactants, and the total kinematic stretch shows its strongest reduction in preheat close to the centreline.

Alternative topologies (for example, axial fields or the opposite radial gradient) produce weaker or less coherent responses under the same operating conditions. In these cases, the forcing either fails to align with the principal transport directions, acts predominantly in regions where its temperature dependence renders it weak, or does not induce the requisite near–axis actuation to modify curvature and the associated kinematics. Consequently, the observable signatures are diminished and more sensitive to the operating regime. The superiority of the radially decreasing configuration in this counterflow arrangement is thus attributable to its favourable alignment with the geometry and to the localisation of forcing in the regions where preferential diffusion–mediated responses can develop.

Magnetic forcing in the radially decreasing configuration acts mainly by redistributing momentum through geometry and preferential diffusion; direct magnetic effects are negligible under the present conditions. The representative thermal thickness remains unchanged, but the balance between tangential strain and curvature is reorganised in a clear spatial pattern, most notably near the axis and across the preheat and reaction zones. The strength and

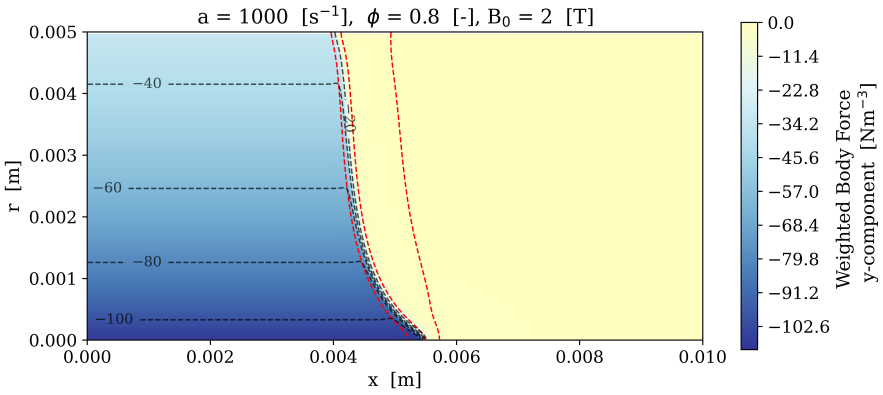

Figure 5.57: Illustration of the y-component of weighted body force at an equivalence ratio of 0.8. Results show a reduction in the weighted body force compared to $\phi = 0.4$.

location of this response depend on the field topology as well as the operating regime (strain rate a and equivalence ratio ϕ). From a methodological perspective, the results highlight the value of reporting a distribution-based thickness measure (such as a KDE mode, with median and trimmed mean as checks) together with local decompositions in progress variable space. This combined view provides a clearer picture than global scalars alone. The present scope is lean H_2/air counterflow flames with a radially decreasing field, but the mechanisms identified are expected to be relevant to other premixed configurations. This completes the Discussion of Key Results; the next chapter (*Conclusion*) summarises the main findings, directly answers the research questions, discusses limitations, and outlines priorities for future work.

6

Conclusion

This thesis aimed to assess control strategies in highly strained flames, specifically focusing on mitigating thermodiffusive instabilities in lean premixed laminar hydrogen flames. The primary goal was to retain the NOx reduction advantage offered by highly strained flames while controlling them to mitigate these instabilities. Methodologically, the study employed local-normal metrics, stretch decomposition, and considered non-unity Lewis/-Fickian diffusion. The research investigated the behaviour of these flames under radially decreasing magnetic fields, exploring their potential as an auxiliary control mechanism to enhance flame stability and mitigate harmful emissions.

This study yielded several key findings regarding the influence of radially decreasing magnetic fields on lean H_2/air premixed counterflow flames:

- **Representative thermal thickness remained effectively unchanged:** The kernel-density (KDE) mode of the local-normal thermal thickness distribution showed a negligible shift ($\leq$0.03%) between 0 T and 2 T magnetic fields. This indicates that the most probable thermal structure of the flame was not materially altered by the magnetic forcing.
- **Total kinematic stretch was reduced:** A decrease of approximately 5-13% in total kinematic stretch (κ) was observed near the axis and within the preheat layers (C < 0.7), while remaining positive overall. This reduction was primarily driven by the curvature-induced contribution.
- **Tangential strain exhibited a two-regime response:** Tangential strain (a_t) decreased by approximately 5-8% in the preheat zone but increased by about 6-8% in the reaction zone (C $\gtrsim$0.5). This opposite-sign change was separated by the progress variable band.
- **Velocity-field redistribution was two-regime:** The axial velocity component broadly weakened, while the radial velocity decreased for low C near the axis and strengthened for C $\gtrsim$0.5 and across the reaction layers. This redistribution of momentum from axial to radial direction influenced the tangential strain pattern.
- **Field topology significantly mattered:** The radially decreasing magnetic field configuration demonstrated the clearest and most geometry-coupled control signature among the tested topologies, yielding coherent and repeatable patterns in κ, a_t, and curvature maps.
- **Magnetic influence weakened with increased strain rate and richer mixtures:** Higher strain rates (a) shortened the effective magnetic influence time and increased inertia, while richer equivalence ratios (ϕ) reduced oxidiser leverage and shifted the flame upstream, diminishing the magnetic field's impact.
- **Instability-relevant indicators showed local stabilisation tendencies:** The strongest reduction of κ occurred in the preheat region near the axis, where curvature effects are most influential, suggesting a local tendency towards stabilisation in curvature-controlled modes.

6.1. Research Questions Addressed

This thesis addressed several key research questions concerning the magnetic control of strained hydrogen flames:

Can magnetic field gradients significantly modify the structure and stability of lean hydrogen premixed counterflow flames through either direct or indirect mechanisms?
Within the examined regime (lean H_2/air premixed counterflow, radially decreasing fields up to 2 T), the *direct* magnetic couplings—species magnetic–diffusion fluxes, magnetic work in the energy equation, and magnetically

induced cross–heat transport—are too weak to produce substantial structural changes on their own. Modifications arise predominantly via an *indirect* pathway: gradients of the field reshape the momentum field through the Kelvin force acting chiefly on paramagnetic O_2, which, in Le < 1 mixtures, interacts with preferential diffusion to adjust local composition and temperature. The resulting shifts in displacement speed, curvature contribution, and tangential strain are spatially localised (notably in preheat and near the axis), whereas global measures are comparatively insensitive. This behaviour accords with the broader expectation that premixed flames offer less magnetic leverage than diffusion flames, where separate streams permit convection–dominated control of oxidiser transport.

How do magnetic field strength, gradient type, and orientation affect the transport and spatial distribution of key radicals, particularly OH, in non-unity Lewis number conditions?
Field strength and topology set both the magnitude and spatial alignment of the Kelvin force, thereby determining where magnetic action couples most effectively to transport. In the counterflow arrangement considered here, a radially decreasing field concentrates forcing near the axis upstream of the flame, enhancing inward O_2 convection; under $Le < 1$, H_2 diffuses faster than heat and O_2, so diffusion only partially offsets this convective build–up, leading to local O_2 enrichment. The resulting shift in composition reduces temperature and heat–release rate in lean premixed conditions and, indirectly, redistributes OH—lowering post–peak OH production and reducing OH consumption around $C \sim 0.7$. Orientation that aligns the gradient with stagnation–point transport (radial-to-axial coupling) yields the clearest and most coherent OH signatures, whereas axial fields couple less efficiently in this geometry.

What roles do direct magnetic effects, such as species-specific diffusion and heat transport, play in modifying flame dynamics, and how do these compare in magnitude and influence to indirect effects like convection and reaction rate alterations?
At 1–2 T, the direct magnetic contributions to transport and energy—species magnetic–diffusion fluxes, magnetic body–force work in the energy equation, and magnetically induced heat interdiffusion—are measurable yet subdominant in lean premixed counterflow and do not, by themselves, provide substantive control. By contrast, the dominant response arises indirectly: the Kelvin force acting on O_2 (with susceptibility $\chi \propto 1/T$) redistributes momentum primarily upstream, and, under non–unity Lewis numbers ($Le < 1$), Fickian diffusion converts the resulting concentration gradients into composition and temperature changes. These thermochemical shifts modify reaction rates and reweight the stretch decomposition (tangential strain versus curvature) and the displacement speed. In summary, the observed dynamics are governed by convection–diffusion–kinetics coupling, with direct magnetic terms acting as a secondary, initiating influence rather than a principal driver.

In what ways does magnetic field application influence instability parameters such as Markstein Length, flame speed, and curvature under strained conditions, and how are these effects mediated by flame structure and transport phenomena?
Under a radially decreasing field in strained counterflow, the near–axis flame front tends to become concave to the reactants, so $\nabla \cdot \hat{n} < 0$ and the curvature term $S_D(\nabla \cdot \hat{n})$ contributes negatively, yielding a local reduction of the total kinematic stretch κ in the preheat band. Velocity redistribution in the flame–attached frame produces a two–regime response of tangential strain a_t (decreasing in preheat, increasing in reaction), while upstream oxygen enrichment depresses temperature and heat release, reducing the kinetic component of the displacement speed S_D^k. The representative thermal thickness (KDE–mode) remains essentially unchanged, indicating preservation of the most probable thermal gradient.

Given this spatial non-uniformity, a single global Markstein length inferred from $S_D = S_L - L_b\kappa$ is not robust. More defensible characterisation is obtained from range–restricted, local regressions estimating $-dS_D/d\kappa$ within verified linear subranges, or from separate strain– and curvature–Markstein sensitivities evaluated in flame–attached coordinates.

6.2. Limitations and Validity

This study, while providing significant insights, is subject to certain limitations regarding its modelling, physics, and numerical fidelity. These limitations define the scope of its validity and highlight areas for future refinement.

From a modelling and physics perspective, the study operated within specific constraints. The magnetic field strengths investigated were within a range where direct magnetic effects on reaction kinetics were considered negligible (i.e., below 5T), aligning with previous findings that very high magnetic fields are required to influence reaction kinetics directly. The analysis primarily focused on lean premixed counterflow hydrogen flames, and

the conclusions drawn may not be directly transferable to other flame configurations (e.g., diffusion flames, partially premixed flames) or different fuel types (e.g., hydrocarbons), where magnetic influence mechanisms might differ significantly. Assumptions related to non-unity Lewis numbers and linear-range constraints for Markstein interpretation also bound the applicability of certain findings. The study focused on steady-state conditions; thus, transient effects and their causality with magnetic influence were not investigated.

Regarding numerical fidelity, the accuracy of the simulations is dependent on factors such as mesh resolution, time-stepping schemes, and the specific numerical solver employed. While the unity Lewis number cases were used as a learning platform to verify the solver against existing results from Yamada et. al. [17], a comprehensive sensitivity analysis concerning mesh independence and time-step convergence was not explicitly detailed in the provided materials. Discrepancies between kinematic and transport-based evaluations of flame displacement speed (S_D) were noted, attributed to numerical factors like incomplete resolution of the reaction zone, numerical diffusion, or interpolation errors in gradient evaluation. These factors can influence the precision of local metrics, although efforts were made to use consistent computational approaches.

Therefore, the validity of the conclusions is bounded by these assumptions and numerical considerations. While the study provides robust insights into the fundamental mechanisms of magnetic control in the specified flame configuration, extrapolation to broader conditions should be done with caution.

6.3. Implications

This research carries significant implications for both scientific understanding and engineering applications, particularly in the context of advanced combustion systems and the development of novel control strategies.

From a scientific and engineering perspective, the findings highlight the potential of magnetic fields as an auxiliary control mechanism for highly strained flames. The observed reduction in total kinematic stretch and the two-regime response of tangential strain suggest that magnetic fields can be leveraged to locally control the strain over the flame surface by changing the flow pattern. This is particularly relevant for applications where NOx reduction is desired, as highly strained flames offer this advantage but are prone to instabilities. The ability to influence flame kinematics through magnetic fields opens avenues for optimising flame location and behaviour, potentially leading to more stable and efficient combustion processes. The study also underscores that the effectiveness of this control is geometry-coupled and diffusion-mediated, emphasising the need for careful consideration of field topology and flame configuration in practical designs. The observed flame shift and reduction in flame speed could be beneficial for flashback prevention and overall flame management in various combustion devices.

Methodologically, this work highlights the value of combining statistical measures of flame properties, such as the kernel density estimate (KDE) mode of thermal thickness, with local analyses performed in progress variable space. This dual approach provides a clearer and more reliable picture of flame structure than relying on global averages alone, which can obscure important features. By examining how the velocity field is redistributed and how kinematic stretch is decomposed into curvature and strain contributions, the study establishes a systematic framework for analysing curved flames. The findings also show that direct magnetic influences are negligible under the present conditions, and that effective control arises indirectly through their interaction with transport processes. These insights suggest that future efforts should focus on exploiting such indirect pathways, particularly in non-unity Lewis number systems, where differential diffusion strongly shapes flame response.

6.4. Future Work

Building upon the findings of this thesis, several promising avenues for future research emerge to further advance the understanding and application of magnetic flame control:

- **Investigate transient effects and causality:** Future work should focus on simulating transient effects to establish causality and determine the precise time scale of magnetic influence on flame dynamics. This would provide a more complete picture of how flames respond to dynamic magnetic fields.
- **Simulate NOx production mechanisms:** To fully assess the environmental implications, it is crucial to simulate NOx production mechanisms under magnetic field influence. This would clarify whether the observed flame kinematic changes translate into tangible reductions in harmful emissions.
- **Develop similarity parameter regimes:** Establishing similarity parameter regimes based on dimensionless numbers like the magnetic Grasshoff Number and Stuart Number would enable better scaling and generalisation of the findings to different operating conditions and flame configurations.
- **Extend analysis to turbulent flame conditions:** Given that most practical combustion systems operate

under turbulent conditions, extending the current analysis to turbulent flame conditions is essential. This would bridge the gap between fundamental laminar studies and real-world applications.

- **Explore alternative magnetic field topologies and strengths:** While the radially decreasing field showed promising results, further investigation into other magnetic field configurations could reveal additional control strategies or optimised conditions.
- **Integrate experimental validation:** Future research should aim to integrate experimental validation with numerical simulations to confirm the predicted magnetic effects and refine the computational models.

In conclusion, this thesis demonstrates that radially decreasing magnetic gradients effectively reorganise local stretch and transport in lean premixed counterflow hydrogen flames, offering a promising avenue for mitigating thermodiffusive instabilities, while notably leaving the representative thermal thickness largely unchanged, underscoring that controllability is geometry-coupled and diffusion-mediated.

References

[1] V. Smil, *Energy and Civilization: A History*, 2nd Edition. The MIT Press, 2017.

[2] R.F.Tylecote, *HISTORY OF METALLURGY*, 2nd Edition. Cambridge University Press, 1992.

[3] R. L. Hills, *Power from steam : a history of the stationary steam engine*. Cambridge University Press, 1989.

[4] J. B. Heywood, *Internal Combustion Engine Fundamentals*, 2nd Edition. McGraw-Hill Education, 2018.

[5] H. J. Penrose, "Jet: The Story of a Pioneer. Sir Frank Whittle, K.B.E., C.B., F.R.S. Frederick Muller Ltd.," *The Aeronautical Journal*, vol. 58, no. 519, pp. 212–212, 1954. DOI: 10.1017/S0001924000098006.

[6] W. E. Council, *World Energy Resources*. World Energy Council, 2023.

[7] I. E. Agency, *The Role of Industry in Decarbonising the Energy Sector*. IEA, 2020.

[8] K. T. Møller, T. R. Jensen, E. Akiba, and H.-w. Li, "Hydrogen - A sustainable energy carrier," *Progress in Natural Science: Materials International*, SI-HYDROGEN STORAGE MATERIALS, vol. 27, no. 1, pp. 34–40, 2017. DOI: 10.1016/j.pnsc.2016.12.014.

[9] A. Züttel, A. Remhof, A. Borgschulte, and O. Friedrichs, "Hydrogen: The future energy carrier," *Philosophical Transactions of the Royal Society A: Mathematical, Physical and Engineering Sciences*, vol. 368, no. 1923, pp. 3329–3342, 2010. DOI: 10.1098/rsta.2010.0113.

[10] J. Larminie and A. Dicks, "Introduction," in *Fuel Cell Systems Explained*, John Wiley & Sons, Ltd, 2003, pp. 1–24. DOI: https://doi.org/10.1002/9781118878330.ch1.

[11] S. Verhelst, T. Wallner, H. Eichlseder, *et al.*, "Electricity Powering Combustion: Hydrogen Engines," *Proceedings of the IEEE*, vol. 100, no. 2, pp. 427–439, 2012. DOI: 10.1109/JPROC.2011.2150190.

[12] F. Oppong, Z. Luo, X. Li, Y. Song, and C. Xu, "Intrinsic instability of different fuels spherically expanding flames: A review," *Fuel Processing Technology*, vol. 234, 2022. DOI: 10.1016/j.fuproc.2022.107325.

[13] T. C. Lieuwen and V. Yang, *Combustion Instabilities In Gas Turbine Engines: Operational Experience, Fundamental Mechanisms, and Modeling*. American Institute of Aeronautics and Astronautics, 2006. DOI: 10.2514/4.866807.

[14] C. K. Law, "Dynamics of stretched flames," *Symposium (International) on Combustion*, vol. 22, no. 1, pp. 1381–1402, 1989. DOI: 10.1016/S0082-0784(89)80149-3.

[15] N. Peters, *Turbulent combustion* (Cambridge monographs on mechanics). Cambridge university press, 2000.

[16] J. Beita, M. Talibi, S. Sadasivuni, and R. Balachandran, "Thermoacoustic Instability Considerations for High Hydrogen Combustion in Lean Premixed Gas Turbine Combustors: A Review," *Hydrogen*, vol. 2, no. 1, pp. 33–57, 2021. DOI: 10.3390/hydrogen2010003.

[17] E. Yamada, M. Shinoda, H. Yamashita, and K. Kitagawa, "Experimental and numerical analyses of magnetic effect on OH radical distribution in a hydrogen-oxygen diffusion flame," *Combustion and Flame*, vol. 135, no. 4, pp. 365–379, 2003. DOI: 10.1016/j.combustflame.2003.08.005.

[18] G. Jiancun, Y. Xigang, H. Shoutao, *et al.*, "Effects of Magnetic Fields on Combustion and Explosion," *Chemistry and Technology of Fuels and Oils*, vol. 58, no. 2, pp. 379–390, 2022. DOI: 10.1007/s10553-022-01395-3. (visited on 12/23/2024).

[19] W.-f. Wu, J. Qu, K. Zhang, W.-p. Chen, and B.-w. Li, "Experimental Studies of Magnetic Effect on Methane Laminar Combustion Characteristics," *Combustion Science and Technology*, vol. 188, no. 3, pp. 472–480, 2016. DOI: 10.1080/00102202.2015.1119825.

[20] A. M. Khlaf, M. A. Ehyaei, and H. A. Abdul Wahhab, "CFD Simulation of Premixed Flame in Counter Burner under the Influence of a Magnetic Field," *International Journal of Computational Methods and Experimental Measurements*, vol. 11, no. 4, pp. 233–238, 2023. DOI: 10.18280/ijcmem.110404.

[21] S. Turns and D. C. Haworth, *An Introduction to Combustion: Concepts and Applications*. McGraw-Hill Education, 2012.

[22] A. H. Lefebvre and D. R. Ballal, *Gas Turbine Combustion: Alternative Fuels and Emissions, Third Edition*, 3rd ed. CRC Press, 2010. DOI: 10.1201/9781420086058.

[23] I. Staffell, D. Scamman, A. V. Abad, *et al.*, "The role of hydrogen and fuel cells in the global energy system," *Energy & Environmental Science*, vol. 12, no. 2, pp. 463–491, 2019. DOI: 10.1039/C8EE01157E.

[24] M. G. Zabetakis, "Flammability characteristics of combustible gases and vapors," Bureau of Mines, Pittsburgh, PA (United States), Tech. Rep., 1964. DOI: 10.2172/7328370.

[25] N. M. Marinov, C. K. Westbrook, and W. J. Pitz, "Detailed and global chemical kinetics model for hydrogen," Lawrence Livermore National Lab. (LLNL), Livermore, CA (United States), Tech. Rep. UCRL-JC-120677; CONF-9510158-1, 1995.

[26] B. Lessani and M. V. Papalexandris, "Time-accurate calculation of variable density flows with strong temperature gradients and combustion," *Journal of Computational Physics*, vol. 212, pp. 218–246, 2006. DOI: 10.1016/j.jcp.2005.07.001.

[27] K. K. Kuo, *Principles of combustion*. Hoboken, NJ : John Wiley, 2005.

[28] M. R. Acquaviva, A. Porcarelli, and I. Langella, "Influence of Soret effect on flame structure and NOx emissions in highly strained lean premixed counterflow hydrogen flames," *Fuel*, vol. 395, p. 134 939, 2025. DOI: 10.1016/j.fuel.2025.134939.

[29] A. Majda and J. Sethian, "The derivation and numerical solution of the equations for zero mach number combustion," *Combustion Science and Technology*, vol. 42, no. 3-4, pp. 185–205, 1985. DOI: 10.1080/00102208508960376.

[30] A. S. Almgren, J. B. Bell, C. A. Rendleman, and M. Zingale, "Low Mach Number Modeling of Type Ia Supernovae. I. Hydrodynamics," *The Astrophysical Journal*, vol. 637, pp. 922–936, 2006. DOI: 10.1086/498426.

[31] T. Poinsot and D. Veynante, *Theoretical and numerical combustion*, 2nd ed. Edwards, 2005.

[32] A. Trouvé and T. Poinsot, "The evolution equation for the flame surface density in turbulent premixed combustion," *Journal of Fluid Mechanics*, vol. 278, pp. 1–31, 1994. DOI: 10.1017/S0022112094003599.

[33] G. K. Giannakopoulos, A. Gatzoulis, C. E. Frouzakis, M. Matalon, and A. G. Tomboulides, "Consistent definitions of "Flame Displacement Speed" and "Markstein Length" for premixed flame propagation," *Combustion and Flame*, vol. 162, no. 4, pp. 1249–1264, 2015. DOI: 10.1016/j.combustflame.2014.10.015.

[34] G. Oztarlik, L. Selle, T. Poinsot, and T. Schuller, "Suppression of instabilities of swirled premixed flames with minimal secondary hydrogen injection," *Combustion and Flame*, vol. 214, pp. 266–276, 2020. DOI: 10.1016/j.combustflame.2019.12.032.

[35] F. H. Vance, A. Scholtissek, P. De Goey, J. Van Oijen, and C. Hasse, "Dynamic stabilization of a hydrogen premixed flame in a narrow channel," *Combustion and Flame*, vol. 248, 2023. DOI: 10.1016/j.combustflame.2022.112560.

[36] H. Böttler, H. Lulic, M. Steinhausen, X. Wen, C. Hasse, and A. Scholtissek, "Flamelet modelling of thermo-diffusively unstable hydrogen-air flames," *Proceedings of the Combustion Institute*, vol. 39, no. 2, pp. 1567–1576, 2023. DOI: 10.1016/j.proci.2022.07.159.

[37] S. Balusamy, A. Cessou, and B. Lecordier, "Measurement of laminar burning velocity–A new PIV approach," 2009.

[38] K. H. Becker, D. Dley, and R. J. Norstrom, "OH* chemiluminescence in hydrocarbon atom flames," *Symposium (International) on Combustion*, vol. 12, no. 1, pp. 405–413, 1969. DOI: 10.1016/S0082-0784(69)80423-6.

[39] A. Porcarelli, B. Kruljević, and I. Langella, "Suppression of NOx emissions by intensive strain in lean premixed hydrogen flamelets," *International Journal of Hydrogen Energy*, vol. 49, pp. 413–431, 2024. DOI: 10.1016/j.ijhydene.2023.08.110.

[40] A. Porcarelli and I. Langella, "Mitigation of preferential diffusion effects by intensive strain in lean premixed hydrogen flamelets," *Proceedings of the Combustion Institute*, vol. 40, no. 1, p. 105 728, Jan. 2024. DOI: 10.1016/j.proci.2024.105728.

[41] E. Yamada, M. Shinoda, H. Yamashita, and K. Kitagawa, "Numerical analysis of a hydrogen-oxygen diffusion flame in vertical or horizontal gradient of magnetic field," *Combustion Science and Technology*, vol. 174, no. 9, pp. 149–164, 2002. DOI: 10.1080/713713079.

[42] J. Baker and M. E. Calvert, "A study of the characteristics of slotted laminar jet diffusion flames in the presence of non-uniform magnetic fields," *Combustion and Flame*, vol. 133, no. 3, pp. 345–357, 2003. DOI: 10.1016/S0010-2180(03)00021-X.

[43] K. Yang, D. Qi, Y. Ying, *et al.*, "Assessment of magnetic effects on soot characteristics in inverse diffusion ethylene flames," *Combustion and Flame*, vol. 260, p. 113 255, 2024. DOI: 10.1016/j.combustflame.2023.113255.

[44] S. H. Park, M. S. Kang, M. S. Cha, J. Park, and S. H. Chung, "Flame spread over twin electrical wires with applied DC electric fields," *Combustion and Flame*, vol. 210, pp. 350–359, 2019. DOI: 10.1016/j.combustflame.2019.09.003.

[45] M. Zharfa and N. Karimi, "Intensification of MILD combustion of methane and hydrogen blend by the application of a magnetic field- a numerical study," *Acta Astronautica*, vol. 184, pp. 259–268, 2021. DOI: 10.1016/j.actaastro.2021.04.023.

[46] Y. Mizutani, M. Fuchihata, and Y. Ohkura, "Pre-mixed laminar flames in a uniform magnetic field," *Combustion and Flame*, vol. 125, no. 1, pp. 1071–1073, 2001. DOI: 10.1016/S0010-2180(00)00244-3.

[47] G. Legros, T. Gomez, M. Fessard, *et al.*, "Magnetically induced flame flickering," *Proceedings of the Combustion Institute*, vol. 33, no. 1, pp. 1095–1103, 2011. DOI: 10.1016/j.proci.2010.06.124.

[48] S. Ueno, H. Esaki, and K. Harada, "Combustion processes under strong DC magnetic fields," *IEEE Transactions on Magnetics*, vol. 21, no. 5, pp. 2077–2079, 1985. DOI: 10.1109/TMAG.1985.1064018.

[49] S. Ueno and K. Harada, "Effects of magnetic fields on flames and gas flow," *IEEE Transactions on Magnetics*, vol. 23, no. 5, pp. 2752–2754, 1987. DOI: 10.1109/TMAG.1987.1065242.

[50] H. Gao, Y. Wang, Y. Wang, M. Zhou, and L. Duan, "Understanding flame behaviours under gradient magnetic fields: The dynamics of non-reacting gas jets," *International Communications in Heat and Mass Transfer*, vol. 159, 2024. DOI: 10.1016/j.icheatmasstransfer.2024.108066.

[51] V. Gilard, P. Gillon, J.-N. Blanchard, and B. Sarh, "Influence of a horizontal magnetic field on a co-flow methane/air diffusion flame," *Combustion Science and Technology*, vol. 180, no. 10, pp. 1920–1935, 2008. DOI: 10.1080/00102200802261506.

[52] A. Jocher, J. Bonnety, T. Gomez, H. Pitsch, and G. Legros, "Magnetic control of flame stability: Application to oxygen-enriched and carbon dioxide-diluted sooting flames," *Proceedings of the Combustion Institute*, vol. 37, no. 4, pp. 5637–5644, 2019. DOI: 10.1016/j.proci.2018.05.156.

[53] A. Muter Khlaif, H. A. Abdul Wahhab, and M. Aliehyaei Ehyaei, "Impact of magnetic field on the stability of laminar flame in a counter burner," *International Journal of Energy Production and Management*, vol. 8, no. 4, pp. 229–234, 2023. DOI: 10.18280/ijepm.080404.

[54] M. Kumar, S. Agarwal, V. Kumar, G. S. Khan, and C. Shakher, "Experimental investigation on butane diffusion flames under the influence of magnetic field by using digital speckle pattern interferometry," *Applied Optics*, vol. 54, no. 9, pp. 2450–2460, 2015. DOI: 10.1364/AO.54.002450.

[55] S. Agarwal, M. Kumar, and C. Shakher, "Experimental investigation of the effect of magnetic field on temperature and temperature profile of diffusion flame using circular grating talbot interferometer," *Optics and Lasers in Engineering*, vol. 68, pp. 214–221, 2015. DOI: 10.1016/j.optlaseng.2015.01.004.

[56] Y. Xie, Z. Wei, T. Zhou, H. Zhen, Z. Liu, and Z. Huang, "Combustion Characteristics of Small Laminar Flames in an Upward Decreasing Magnetic Field," *Energies*, vol. 14, no. 7, p. 1969, 2021. DOI: 10.3390/en14071969.

[57] J. Hult, S. Gashi, N. Chakraborty, *et al.*, "Measurement of flame surface density for turbulent premixed flames using PLIF and DNS," *Proceedings of the Combustion Institute*, vol. 31, no. 1, pp. 1319–1326, 2007. DOI: 10.1016/j.proci.2006.07.188.

[58] S. Chaudhuri and B. Savard, *Turbulent flame speed based on the mass flow rate: Theory and DNS*, 2022. DOI: 10.48550/arXiv.2202.06719.

[59] A. Amato, M. Day, R. K. Cheng, J. Bell, D. Dasgupta, and T. Lieuwen, "Topology and burning rates of turbulent, lean, H2/air flames," *Combustion and Flame*, vol. 162, no. 12, pp. 4553–4565, 2015. DOI: 10.1016/j.combustflame.2015.09.010.

[60] F. A. Williams, *Combustion theory: the fundamental theory of chemically reacting flow systems* (Combustion science and engineering series), 2nd ed. Addison-Wesley, 1985.

A

Solver Specifications

A.1. fvSchemes

Listing A.1: fvSchemes file

```
/*--------------------------------*- C++ -*----------------------------------*\
| =========                 |                                                 |
| \\      /  F ield         | OpenFOAM: The Open Source CFD Toolbox           |
|  \\    /   O peration     | Version:  2.3.0                                 |
|   \\  /    A nd           | Web:      www.OpenFOAM.org                      |
|    \\/     M anipulation  |                                                 |
\*---------------------------------------------------------------------------*/
FoamFile
{
    version     2.0;
    format      ascii;
    class       dictionary;
    location    "system";
    object      fvSchemes;
}
// * * * * * * * * * * * * * * * * * * * * * * * * * * * * * * * * * * * * //

ddtSchemes
{
    default         CrankNicolson 0.2;//Euler;//backward;
}

gradSchemes
{
    default         fourth;//Gauss cubic;
}

divSchemes
{
    default         Gauss cubic;

    div(phi,U)      Gauss cubic;//limitedLinearV 1;
    div(phi,Yi_h)   Gauss limitedCubic 1;//limitedLinear 1;
    div(phi,K)      Gauss cubic;//limitedLinear 1;
    div(phid,p)     Gauss cubic;//limitedLinear 1;
    div(phi,epsilon) Gauss cubic;//limitedLinear 1;
    div(phi,k) Gauss cubic//limitedLinear 1;
    div(((rho*nuEff)*dev2(T(grad(U))))) Gauss cubic;//linear;
    div(phiU,p)     Gauss cubic;//limitedLinear 1;
    div(vk) Gauss cubic;//linear;
}

laplacianSchemes
{
    default         Gauss cubic orthogonal;
}
```

```
47
48 interpolationSchemes
49 {
50     default         cubic;
51 }
52
53 snGradSchemes
54 {
55     default         corrected;//orthogonal;
56 }
57
58 fluxRequired
59 {
60     default         no;
61     p;
62     pd;
63 }
64
65
66 // ************************************************************************* //
```

A.2. fvSolution

Listing A.2: fvSchemes file

```
1  /*--------------------------------*- C++ -*----------------------------------*\
2  | =========                 |                                                 |
3  | \\      /  F ield         | OpenFOAM: The Open Source CFD Toolbox           |
4  |  \\    /   O peration     | Version:  3.0.1                                 |
5  |   \\  /    A nd           | Web:      www.OpenFOAM.org                      |
6  |    \\/     M anipulation  |                                                 |
7  \*---------------------------------------------------------------------------*/
8  FoamFile
9  {
10     version     2.0;
11     format      ascii;
12     class       dictionary;
13     location    "system";
14     object      fvSolution;
15 }
16 // * * * * * * * * * * * * * * * * * * * * * * * * * * * * * * * * * * * * * //
17
18 solvers
19 {
20     rho
21     {
22         solver          PCG;
23         preconditioner  DIC;
24         tolerance       1e-07;
25         relTol          0.1;
26     }
27
28
29     rhoFinal
30     {
31         $rho;
32         tolerance       1e-09;
33         relTol          0;
34     }
35
36     p
37     {
38         solver          PCG;
39         preconditioner
40         {
41             preconditioner  GAMG;
42             tolerance       1e-08;
43             relTol          0.01;
44             nVcycles        2;
45             smoother        DICGaussSeidel;
```

```
46              nPreSweeps      2;
47          }
48          tolerance       1e-08;
49          relTol          0.01;
50           maxIter         100;
51      }
52
53      pFinal
54      {
55          solver          PCG;
56          preconditioner
57          {
58              preconditioner  GAMG;
59              tolerance       2e-09;
60              relTol          0;
61              nVcycles        2;
62              smoother        DICGaussSeidel;
63              nPreSweeps      2;
64          }
65
66          tolerance       1e-09;
67          relTol          0;
68          maxIter         100;
69      }
70
71      p_rgh
72      {
73          solver          PCG;
74          preconditioner
75          {
76              preconditioner  GAMG;
77              tolerance       1e-08;
78              relTol          0.01;
79              nVcycles        2;
80              smoother        DICGaussSeidel;
81              nPreSweeps      2;
82          }
83          tolerance       1e-08;
84          relTol          0.01;
85           maxIter         100;
86      }
87
88      p_rghFinal
89      {
90          solver          PCG;
91          preconditioner
92          {
93              preconditioner  GAMG;
94              tolerance       2e-09;
95              relTol          0;
96              nVcycles        2;
97              smoother        DICGaussSeidel;
98              nPreSweeps      2;
99          }
100
101         tolerance       1e-09;
102         relTol          0;
103         maxIter         100;
104     }
105
106
107     "(U|k|epsilon)"
108     {
109         solver          smoothSolver;
110         smoother        symGaussSeidel;
111         tolerance       1e-08;
112         relTol          0;
113     }
114
115     "(U|k|epsilon)Final"
116     {
```

```
        $U;
        tolerance       1e-09;
        relTol          0;
    }


    "(he|h|e|Yi)"
    {
        solver          PBiCGStab;
        preconditioner  DILU;
        tolerance       1e-08;
        relTol          0;
    }

    "(he|h|e|Yi)Final"
    {
        $he;
        tolerance       1e-09;
        relTol          0;
    }

}

PIMPLE
{
    transonic           no;
    nCorrectors         3;
    nOuterCorrectors    1;
    nNonOrthogonalCorrectors    0;//2;
    momentumPredictor   on;//yes;
}

relaxationFactors
{
    fields
    {
        p       0.4;
    }

    equations
    {
        "(U|h|k|epsilon)"       0.6;
        "Yi.*"                  0.6;
    }
}

// ************************************************************************* //
```

B

Test Matrix

Table B.1: Test matrix for $Le = 1$ cases ($\phi = 0.4$).

Topology	**B$_0$ (T)**	**Strain rate a (s^{-1})**	**Notes**
Radially decreasing	0.5, 1.0, 1.5, 2.0	1000	Full set
Radially increasing	0.5, 1.0, 1.5, 2.0	1000	Full set
Axially decreasing	0.5, 1.0, 1.5, 2.0	1000	Full set
Axial Gaussian	0.5, 1.0, 1.5, 2.0	1000	Full set
Radially decreasing	1.0, 2.0	1500	Reduced set
Radially increasing	1.0, 2.0	1500	Reduced set
Axially decreasing	1.0, 2.0	1500	Reduced set
Axial Gaussian	1.0, 2.0	1500	Reduced set
Radially decreasing	1.0, 2.0	2000	Reduced set
Radially increasing	1.0, 2.0	2000	Reduced set
Axially decreasing	1.0, 2.0	2000	Reduced set
Axial Gaussian	1.0, 2.0	2000	Reduced set

Table B.2: Test matrix for $Le < 1$ cases.

Topology	**B_0 (T)**	**Strain rate a (s^{-1})**	ϕ
No field	0	1000	0.4, 0.8
Radially decreasing	2.0	1000	0.4, 0.8
No field	0	2000	0.4, 0.8
Radially decreasing	2.0	2000	0.4, 0.8